Imperial College London

British Heart Foundation

Experimental and Numerical Investigation of Arterial Wall Mass Transport

---

PhD Thesis

Kok Yean Chooi

Supervisors:
Prof. Peter D. Weinberg
Prof. Spencer Sherwin

Department of Bioengineering
Faculty of Engineering
Imperial College London

This thesis is submitted for examination for the degree of Doctor of Philosophy of Imperial College London

Wednesday 13th April, 2016

Copyright Declaration

The copyright of this thesis rests with the author and is made available under a Creative Commons Attribution Non-Commercial No Derivatives licence. Researchers are free to copy, distribute or transmit the thesis on the condition that they attribute it, that they do not use it for commercial purposes and that they do not alter, transform or build upon it. For any reuse or redistribution, researchers must make clear to others the licence terms of this work

---

Declaration of Originality

I hereby declare that the contents of this thesis are my original work and includes no material previously published or written by another person, nor material which has been credited towards the award of any other degree or diploma of any institute of higher education, except where due acknowledgment has been made.

K. Yean Chooi

Abstract

The accumulation of plasma macromolecules in the arterial intima is a critical step in atherogenesis. It depends on the balance between influx across the endothelium and efflux across the media. The work presented in this thesis investigated these phenomena.

The distribution of 'hotspots' of high endothelial permeability around aortic branches was mapped in immature and mature rabbits; the pattern of disease at such sites changes with age. The pattern of hotspots of Evan's Blue dye-labelled albumin uptake was found to change with age. Using statistical techniques that account for spatial autocorrelation and non-linear relations between variables, a significant correlation with the pattern of cholesterol deposition was obtained at both ages. The hotspot patterns did not correlate with patterns of mitosis. The data also showed that the division of transendothelial transport pathways into 'small' and 'large' pores may represent an arbitrary division of a continuum of pore sizes. Albumin is smaller than the lipoproteins thought to trigger atherosclerosis. The study was therefore repeated using rhodamine-labelled 2 MDa dextran. In immature animals, the pattern of hotspots for this larger tracer was similar to the pattern for albumin. The mature pattern of dextran uptake differed from the immature one, but it was not the same as that observed for albumin.

Further studies investigated transport through the media. As the transport of large molecules occurs predominantly by advection, characterising transmural water flux is important. Ex vivo experimental studies investigated effects of pressure and muscle contraction on hydraulic resistance. Numerical studies based on structural data from the ex vivo experiments were used to characterise the resistance of the media, and the intimal resistance was obtained by subtraction. Intimal and medial resistances in the order $10^{11}\,\mathrm{kg\,s^{-1}\,m^{-2}}$ were found to change in opposite directions with increasing pressure or muscle contraction.

The results may assist in understanding and preventing the development of atherosclerosis.

Acknowledgements

Much of the research presented in my thesis would not have been possible without the help of a number of people at several facilities and institutions and I would like to take this opportunity to thank them for all their contributions.

Firstly, I would like to thank my supervisors, Prof. Peter Weinberg and Prof. Spencer Sherwin for their support over the last four years. Peter's patience and gentle guidance has especially shaped my approach to technical writing and critical appraisal of scientific literature.

I owe a great deal of gratitude to the students, postdocs, research fellows and technicians from the departments of Bioengineering and Aeronautics; and the faculty of Medicine. Special mention goes to Dr. Andrew Comerford, with whom I worked on many projects including all of the computations and much of the image processing presented here. On the experimental side, I am eternally indebted to several people: Mr. Piotr Sowinski, Prof. Peter Weinberg and, especially for the first few months, Dr. Anthony Hunt and Dr. Eleni Bazigou, were always ready to suggest and discuss solutions to the latest technical difficulties arising in my *ex vivo* experiments, including some pretty far-fetched ideas at times. Their combined veterinary and surgical experience was instrumental in establishing a working method. Finally, the endless (and often thankless) efforts of Mr. Ken Keating and Mr. Edgar Ibarguen made my hours in the laboratories more productive and enjoyable.

I would also like to thank other members of the department for their thought-inducing discussions at lunch, or in the laboratories, corridors and lifts on all topics from permeability measurement to methods in light microscopy: Mr. Ethan Rowland (who had to endure several late-night discussions with me on optics and statistics), Prof. Kim Parker, Dr. Emma Bailey, Dr. Katherine Fraser, Mr. Stephen Gray, Dr. Sietse Braakman, Mr. Jason Chang, Mr. Mean Ghim, Miss Yumnah Mohamied and Miss Paola Alpresa.

I thank Mr. Mark Hopkinson at the Royal Veterinary College for training me and allowing me the use of their X-ray micro-CT scanner and Mr. Simon Burbridge for allowing me to use the computational resources of the Imperial College High Performance Computing Service.

The funding for this work all came from an MRes/PhD studentship at the British Heart Foundation (BHF) Centre of Research excellence at Imperial College. I thank them not only for the funding but also for the support and the opportunities they have given me to expand my general scientific knowledge with

their structured MRes/PhD training program and informal journal clubs. It has been a privilege to be part of this programme and I would like to thank the staff and students of the Centre for their horizon-broadening discussions and the management team for their friendliness and efficiency. In particular, Ms. Clodagh Li for having a real interest in my well being and progress, even after the end of her tenure. I would also like to thank the people who trained me during my MRes studies at the Centre: Prof. Molly Stevens, Prof. Michael Schneider, Dr. Daniel Stuckey, Dr. Luis Rojo, Dr. Sara McSweeney, Dr. Zahra Mohri, Dr. Lindsey Clarke and Mr. Daniel Wells.

I am not sure if thanks or apologies would be more appropriate to all those who agreed to sign up for the many British Heart Foundation London-Brighton and London-Southampton bike rides we have done over the last four years, some of whom needed more persuasion than others: Phin, Peter, Isobel, Jonathan, Jan, Spencer, Andrew, Ethan, Stella, Emma, Caroline, Tim, Eugene, Zahra, Taghreed, Ewa, Agata, Paola, Mariea, Rob, Anthony, Ameeta, Mike, Aditi, Hilary, Mercedes, Ose, Stuart and Pradeep. I hope this Weinberg/Sherwin group tradition continues to help support the BHF, who funds so much of our research.

Finally, I must thank my family. My parents have always placed my education above everything else and supported me in whatever interested me and I appreciate their unconditional love and genuine interest in whatever I do. My brother, Phin, who has always been my harshest critic, has been a great sounding board for my ideas and all my endeavours to date have been improved by that.

I dedicate this thesis to all my previous teachers, mentors and supervisors. The self-belief they instilled in me gave me the confidence to pursue post-graduate studies.

Yean Chooi

April, 2015

Contents

Copyright Declaration 1

Declaration of Originality 2

Abstract 3

Acknowledgements 4

Table of Contents 10

List of Figures 12

List of Tables 13

Abbreviations and Symbols 14

1 Atherosclerosis and Mass Transport in the Walls of Large Arteries 16

1.1 Cardiovascular diseases . . . 16

1.2 Atherosclerosis: global and local risk factors . . . 17

1.3 Arterial wall structure and mass transport . . . 17

1.3.1 Transendothelial transport of macromolecules . . . 18

1.4 Heterogeneity of medial mass transport properties as a local risk factor . . . 19

1.5 Research Aims . . . 20

1.6 Outline . . . 21

2 Patterns of Endothelial Permeability to Small Macromolecules 23

2.1 Overview . . . 23

2.1.1 Endothelial transport pathways and the cell turnover-leaky junction hypothesis . . . 23

2.1.2 Observations supporting the CTLJ hypothesis *in vivo* . . . 24

2.1.3 Hotspots and disease patterns . . . 25

2.1.4 Technical innovations . . . 25

2.2 Methods . . . 25
2.2.1 Animals and diet . . . 25
2.2.2 EBA uptake experiments . . . 26
2.2.3 Analysis of EBA images . . . 26
2.2.4 Cell division experiments . . . 29
2.2.5 Spatial correlation statistics . . . 30
2.3 Results . . . 35
2.3.1 Animals . . . 35
2.3.2 Validation of segmentation method on test images . . . 36
2.3.3 Hotspots . . . 38
2.3.4 Mitosis . . . 39
2.3.5 Lesion prevalence . . . 39
2.3.6 Spatial correlations . . . 40
2.4 Discussion . . . 40
2.5 Conclusions . . . 45

3 Patterns of Endothelial Permeability to Large Macromolecules 46
3.1 Introduction . . . 46
3.2 Methods . . . 47
3.2.1 Animals . . . 47
3.2.2 *In vivo* Protocol . . . 47
3.2.3 Immunofluorescence Staining for CD31 and Preparation of Tissue for Confocal Microscopy . . . 48
3.2.4 Confocal Microscopy . . . 48
3.2.5 Image Analysis . . . 48
3.3 Results . . . 55
3.3.1 Outliers . . . 55
3.3.2 Qualitative comparisons . . . 56
3.3.3 Statistical comparisons of hotspot occurrence between locations . . . 57
3.3.4 Validation of hotspot segmentation . . . 57
3.4 Discussion . . . 58
3.4.1 Further work . . . 61

4 Development of Methods to Determine Medial Mass Transport Properties **62**

4.1 Introduction . . . 62

4.2 Established Experimental Methods . . . 62

4.2.1 Preparation of Fluorescent Protein Tracer . . . 62

4.2.2 Preparation of Glycerol-based Anti-fade Mounting Medium . . . 63

4.2.3 Preparation of Poly(dimethylsiloxane)-lined petri dishes . . . 63

4.3 Development of *ex vivo* L_p and P Measurement Methods . . . 63

4.3.1 Uncertainty Analysis . . . 64

4.3.2 Feasibility Studies in Various Arteries . . . 66

4.3.3 The External Pressurisation/Measurement Circuit . . . 68

4.3.4 Development of Procedures using Cadavers . . . 71

4.3.5 Transfer of Procedures to Anaesthetised Animals . . . 75

4.3.6 Refinement of Surgical Techniques . . . 75

4.3.7 Final Surgical Protocol . . . 77

4.4 Development of Sample Preparation and Imaging Methods . . . 79

4.4.1 Preservation of Pressurised Structure . . . 79

4.4.2 Epoxy embedding . . . 81

4.4.3 Physical Sectioning and Image Volume Reconstruction vs 3D Imaging Techniques . 82

4.4.4 Final Choice of Embedding, Sample Preparation and Imaging Method . . . 84

4.5 Development of Methods to Determine Rh-BSA Distribution and Available Space . . . 85

4.5.1 Determination of Time Required to reach Equilibrium . . . 86

4.5.2 Determination of Rh-BSA Distribution at Equilibrium . . . 87

4.5.3 Determination of Rh-BSA Distribution at Steady State . . . 87

4.6 Development of Image Processing Methods . . . 88

4.6.1 Accounting for Signal Attenuation with Depth . . . 88

4.6.2 Image Volume Rotation for Axis Alignment . . . 88

4.6.3 Semi-automation of image processing . . . 88

4.7 Computational simulations . . . 88

4.7.1 Unsteady Brinkman's equation . . . 88

4.7.2 Effective permeability . . . 89

4.8 Geometry and fictitious solid objects . . . 91

5 Medial Hydraulic Resistance as a Function of Transmural Pressure **94**

5.1 Introduction . . . 94

5.2 Methods . . . 96
5.2.1 Overview: Interconnection of experimental and computational methods . . . 96
5.2.2 *Ex vivo* experiments . . . 97
5.2.3 Microscopy and image processing . . . 99
5.2.4 Effective permeability . . . 100
5.2.5 Porous media mixture theory . . . 101
5.2.6 Solid volume fraction . . . 102
5.2.7 Intimal hydraulic resistance . . . 103
5.3 Results . . . 103
5.3.1 Hydraulic conductance of the whole wall . . . 103
5.3.2 Permeability of the media . . . 103
5.3.3 Solid volume fraction of the media . . . 105
5.3.4 Empirical constitutive relationship . . . 105
5.3.5 Intimal hydraulic resistance . . . 106
5.4 Discussion . . . 106

6 Medial Hydraulic Resistance as a Function of Medial Tone 112
6.1 Introduction . . . 112
6.2 Methods . . . 113
6.2.1 Overview . . . 113
6.2.2 Animals . . . 114
6.2.3 Vessel Isolation . . . 115
6.2.4 Hydraulic Conductance Experiments with Noradrenaline . . . 115
6.2.5 Microscopy and image processing . . . 115
6.2.6 Effective Permeability . . . 117
6.2.7 ECM Volume Fraction . . . 118
6.2.8 VSMC aspect ratio . . . 119
6.2.9 Intimal hydraulic resistance . . . 119
6.3 Results . . . 119
6.3.1 Comparison of Hydraulic Conductance with and without NA . . . 119
6.3.2 VSMC contraction and Volume Fraction . . . 120
6.3.3 Medial hydraulic permeability . . . 121
6.3.4 Decomposition of wall hydraulic resistance . . . 121
6.4 Discussion . . . 123

7 Conclusions **125**

7.1 Summary of Key Findings 125

7.2 Wider Applicability of Tools and Techniques Developed 126

7.3 Recommendations for Future Work 127

7.3.1 Further development of experimental methods 127

References **136**

A Publications **137**

A.1 Journal Articles 137

A.2 Conference Contributions 137

B Attenuation Correction and Image Volume Rotation **139**

B.1 Downsampling 139

B.2 User prompting 141

B.3 Rotation and attenuation correction 147

List of Figures

1.1 Schematic of arterial wall structure 18

2.1 Schematic showing major steps in hotspot segmentation algorithm 27
2.2 Convergence plots for determining optimum number of levels in thresholding algorithm . . 36
2.3 Example image histograms of key steps of EBA image processing algorithm 37
2.4 Validation of hotspot segmentation using test images 37
2.5 Average hotspot maps for branches in immature rabbits 38
2.6 Average hotspot maps for branches in mature rabbits 39
2.7 Average BrdU-positive nuclei maps 39
2.8 Average lesion prevalence maps 40
2.9 Average large (> 450pixel) hotspot maps for branches in immature rabbits 42
2.10 Average large (> 450pixel) hotspot maps for branches in mature rabbits 42
2.11 Average rhodamine albumin uptake maps for immature and mature rabbits 44
2.12 Autofluorescence around rabbit intercostal branches 45

3.1 Approximate locations of ROIs around intercostal ostia in dextran endothelial permeability study 49
3.2 Overview of automated ostium masking algorithm 51
3.3 Examples of automatically generated ostium masks from AF MIPs of dextran dataset . . . 52
3.4 Histogram of average background fluorescence around naive rabbit ostia 52
3.5 Overview of automated intensity-based hotspot thresholding algorithm 54
3.6 Overview of automated skeletonising algorithm 55
3.7 Boxplots showing number of spots identified in dextran uptake images 56
3.8 Hotspot occurence around intercostal ostia in immature rabbits 57
3.9 Hotspot occurence around intercostal ostia in immature rabbits 58
3.10 Average number of dextran hotspots occurring around rabbit intercostal ostia 59
3.11 Average background fluorescence intensity of dextran uptake images 60

4.1 Arterial corrosion casting apparatus . . . 67
4.2 Photograph of rat arterial cast . . . 67
4.3 *Ex vivo* vessel preparation pressurisation apparatus . . . 68
4.4 Validation of pressurisation/measurement circuit . . . 70
4.5 Definition of bifurcation dimensions . . . 70
4.6 Results of fixative selection trials . . . 80
4.7 Determination of time required to reach equilibrium with Rh-BSA . . . 87
4.8 Calculating effective permeability by oversampling (After Comerford et al., 2015) . . . 90
4.9 Sequence of steps to transfer confocal image data to the quadrature points. (After Comerford et al., 2015) . . . 92

5.1 Flowchart showing interconnection of methods used in study on effects of transmural pressure on arterial hydraulic resistances . . . 97
5.2 *Ex vivo* vessel preparation pressurisation apparatus . . . 98
5.3 Sample trace showing bubble displacement during measurement of hydraulic flux . . . 104
5.4 Relationship between L_p with pressure in the physiological range . . . 104
5.5 Relationship between permeability and pressure in the principal axes of the arterial wall . . . 105
5.6 Structural deformation of media due to arterial pressurisation . . . 105
5.7 Constitutive relation between radial medial permeability and tissue deformation . . . 106
5.8 Relationship between R_{WALL}, $R_{MED}$and $R_{INT}$with pressure in the physiological range . . . 107

6.1 Flowchart showing interconnection of methods used in study on effects of vascular tone on arterial hydraulic resistances . . . 114
6.2 *Ex vivo* vessel preparation pressurisation apparatus for SMC tone study . . . 116
6.3 Extraction of a representative tissue region from confocal imaging of the fixed arterial media 117
6.4 Sample trace showing bubble displacement during measurement of hydraulic flux . . . 120
6.5 Change in L_p with VSMC tone in the physiological range . . . 120
6.6 Change in medial structure upon SMC contraction . . . 121
6.7 ECM volume fraction change due to VSMC contraction . . . 122
6.8 Relationship between permeability and tone in the principal ages of the arterial wall . . . 122
6.9 Change in components of total wall hydraulic resistance with tone in the physiological range 122

List of Tables

2.1 Summary of rabbit data used in EBA and BrdU studies 35

2.2 Correlation coefficients and associated confidence intervals between all pairs of the parameters measured in immature rabbits 40

2.3 Correlation coefficients and associated confidence intervals between all pairs of the parameters measured in mature rabbits 41

3.1 Summary of ages and weights of rabbits used in dextran endothelial permeability study . . . 47

4.1 Preliminary uncertainty analysis for L_p Measurements 65

4.2 Preliminary L_p measurements in mouse and rat bifurcations 74

4.3 Treatment combinations used in fixative trials 80

4.4 Confocal microscope scan settings 86

Abbreviations and Symbols

List of Abbreviations

AF	Autofluorescence
BSA	Bovine serum albumin
CLSM	Confocal laser scanning microscope
EBA	Evan's blue dye-conjugated bovine serum albumin
EBD	Evan's blue dye
EC	Endothelial cell
ECM	Extracellular matrix
MIP	Maximum intensity projection
NA	Noradrenaline
NZW	New Zealand White
PDMS	Poly(dimethylsiloxane)
PBS	Phosphate-buffered saline
Rh	Rhodamine
Rh-BSA	Rhodamine-conjugated bovine serum albumin
SD	Sprague-Dawley
TMR	Tetramethylrhodamine
TMR-dextran	Lysine-fixable Tetramethylrhodamine-conjugated dextran
TSS	Tyrode's salt solution
VSMC	Vascular smooth muscle cell

List of Symbols

L_p	Hydraulic conductance
P	Solute Permeability

$Pé$	Péclet number
R_{WALL}	Total hydraulic resistance of the arterial wall
R_{MED}	Hydraulic resistance of the arterial tunica media
R_{INT}	Hydraulic resistance of the arterial intima
ϕ^{ECM}	Extracellular matrix volume fraction
ϕ^{SMC}	Vascular smooth muscle cell volume fraction

Chapter 1

Atherosclerosis and Mass Transport in the Walls of Large Arteries

1.1 Cardiovascular diseases

Cardiovascular diseases (CVDs) are the leading cause of death worldwide, accounting for 29 % of all deaths - a total of 17.1 million - in 2004 (WHO, 2009); . This burden of disease is expected to increase over the next few decades: the World Health Organisation predicts almost 23.6 million CVD-related deaths occurring in 2030 (WHO, 2009), highlighting the need for a better understanding of the causes of CVDs.

Atherosclerosis is the underlying pathological process that causes the majority of CVDs. The initial stage of this chronic disease is a clinically-silent lesion termed the fatty streak. It is thought to arise in response to the accumulation of plasma macromolecules, particularly lipid-carrying lipoproteins, in the subendothelial space of the walls of large arteries. As the accumulation of lipids and the consequent inflammatory response and fibrosis build up, the arterial wall remodels, alleviating the lumen-narrowing effects of the plaques. Continued accumulation leads to the formation of complicated lesions with smooth muscle cell proliferation, calcification and necrosis. As these begin to exceed the wall's ability to remodel, the lumen becomes chronically stenosed, causing local ischaemia. A further risk presented by chronic lesions is plaque rupture, which triggers blood clotting, either completely occluding the lumen at the rupture site, or in downstream vessels of smaller diameter due to transport and embolization of small clot fragments. The different types of lesion have been formally categorised by the American Heart Association (Stary et al., 1995).

The effects of atherosclerosis on a person's wellbeing is dependent on the location of the plaque or plaque rupture. The two most common clinical manifestations of atherosclerosis are cerebrovascular disease and coronary heart disease; together these accounted for over three quarters of all CVD-related deaths in 2009 (WHO, 2009)

1.2 Atherosclerosis: global and local risk factors

Current clinical guidelines for assessing an individual's risk of developing CVDs are based on systemic or global risk factors (Goff et al., 2013). One such clinical tool is the Systematic Coronary Risk Evaluation published by the European Society of Cardiology (Conroy et al., 2003) in which systolic blood pressure, gender, age, smoking habit and total: high density lipoprotein (HDL) cholesterol ratio are used to calculate a percentage ten-year risk of developing fatal CVD.

This *global* approach arises from an epidemiological view of the disease, as opposed to a mechanistic approach studying the disease at the level of the tissue or organ. It is therefore unsurprising that it is unable to explain a key feature of atherosclerosis: that plaques in both humans and animals occur only in large and mid-sized systemic arteries and form distinct patches of diseased tissue with the adjacent arterial tissue completely unaffected (Caro et al., 1971, DeBakey et al., 1985, Anitschkow, 1933, Nakashima et al., 1994). By definition, systemic factors influence the entire arterial system and therefore cannot explain spatial variation on the length scales typical of atherosclerotic plaques. Many studies aimed at understanding the mechanisms that cause the initiation of atherosclerosis have therefore focused on identifying local risk factors for atherogenesis.

The earliest experimental studies on the localisation of plaques were carried out by Anitschkow (See Anitschkow, 1933) who developed an *in vivo* animal model of atherosclerosis in which rabbits were fed cholesterol dissolved in vegetable oil. In the aortas of these animals, lesions formed downstream and at the sides of intercostal branches but upstream regions were spared. The blood cholesterol concentrations were several times higher than in normal rabbits so it was concluded that material within the plaques had originated from the lumen and infiltrated into the wall (Anitschkow, 1933). These observations eventually led to what is known today as the lipid hypothesis of atheroslcerosis: circulating lipid-carrying macromolecules (eg: low density lipoprotein, LDL) accumulate in the arterial wall, triggering a series of cellular responses that eventually lead to plaque formation (Steinberg, 2002).

The patchy distribution of plaques has led researches to look for spatial variations that occur over similar length scales that could explain local variations in lipid accumulation, so-called 'local risk factors'. Much of this work has focused on the influx of macromolecules across the endothelium. Less attention has been given to local variations in the rate of efflux of macromolecules once they have entered the arterial wall. As accumulation is an imbalance of influx and efflux, investigating the factors that affect both fluxes are of equal importance and is the broad topic of this thesis.

1.3 Arterial wall structure and mass transport

The arterial wall is comprised of three main layers: the tunica intima, tunica media and tunica adventitia (Fig 1.1 - the information in this section is derived from standard texts: Levick, 2003, Tortora and Derrickson, 2006). Each layer has a specific structure that enables the tissue to fulfil a specific function. The tunica intima

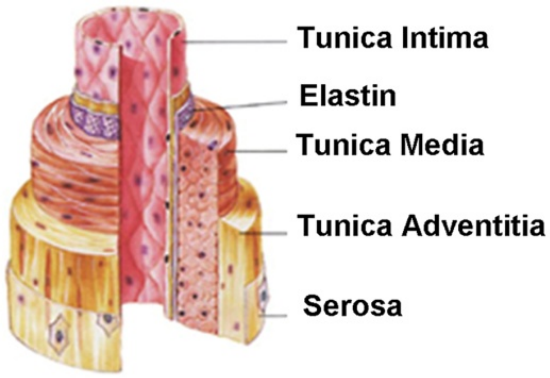


Figure 1.1: Schematic of arterial wall structure (after Callanan et al., 2011)

is made up of a monolayer of tightly joined endothelial cells (ECs) on a basement membrane consisting mainly of collagen; the endothelium forms a barrier that impedes transport of fluid and dissolved molecules out of the lumen. The tunica media is separated from the tunica intima by the internal elastic lamina. The media is composed of vascular smooth muscle cells (VSMCs) arranged in fasicles (Clark and Glagov, 1985) with a circumferential/helical orientation, separated by concentric elastin sheets. Gaps between VSMCs are filled with a ground substance containing elastin and collagen fibres and water-retaining proteoglycans. VSMC tone is known to regulate lumen diameter in muscular arteries. The tunica adventitia of larger arteries contains capillary and lypmphatic vessels (collectively known as the vasa vasorum), which supply the vessel wall with nutrients and remove waste products in tissue fluid. They are embedded in a loose network of extracellular matrix proteins and proteoglycans. The adventitia also contains fat cells, fibroblasts and nerves.

Cholesterol and triglycerides are transported in the blood plasma as the lipid component of lipoproteins, in which the hydrophobic lipids are made soluble in the aqueous plasma by a coating of apolipoproteins and phospholipids. Of the five major groups of lipoproteins, low-density lipoprotein and high-density lipoprotein (LDL, HDL) are the main classes involved with lipid transport to and from vascular tissues respectively and are therefore the classes of interest with respect to lipid accumulation. (The situation may be different in non-human species - for example, very low density lipoproteins can be more important than LDL in cholesterol-fed rabbits.) The two gradients governing their transport are the pressure and concentration gradients of the fluid and solute respectively. At the scale of the vessel, both gradients act radially outwards, setting up advectional and diffusional fluxes from the lumen into the tissue.

Accumulation of macromolecules results from the interaction of these two transport gradients with the permeabilities associated with the structures of the various tissues that make up the wall. Therefore heterogeneity in accumulation leading to the patchy distribution of disease could arise from multiple sources.

1.3.1 Transendothelial transport of macromolecules

A more detailed review of the literature is provided as the introduction to chapter 2. What follows here is a brief survey as motivation for research aims (1) and (2) outlined in section 1.5.

Spatial heterogeneity in endothelial permeability to plasma macromolecules has been investigated as a possible local risk factor. Possible transport routes for these molecules include active vesicular transport and passive paracellular transport through intracellular junctions, recently reviewed by Tarbell (2003). Tight junctions between ECs (1-2 nmTarbell, 2010) prevent transendothelial transport of blood-borne macromolecules. Tight junctions do not create a continuous seal between the lumen and the tunica media. Naturally occurring breaks in the tight junction (approx. 20 nm) are large enough to allow albumin (4×14 nm; DeBlois et al., 1973) through but macromolecules such as LDL (Stokes-Einstein diameter 23 nm; DeBlois et al., 1973) are too large to pass through pores of this size.

One current hypothesis for the paracellular transport of macromolecules of the size of LDL is the leaky-junction cell turnover hypothesis (Weinbaum et al., 1985) which postulates that intercellular junctions are transiently widened during certain stages of cell turnover events (eg: mitosis and apoptosis), causing foci of high endothelial permeability. Dimensions of these leaky junctions were estimated to be 80-1330 nm during mitosis and 15-1000 nm during apoptosis (Chen et al., 1995), supporting the idea that LDL could pass through such pores.

Previous work in our group has shown that the pattern of lesions in cholesterol-fed rabbits changes with age. Lesion prevalence is highest downstream of aortic ostia in young animals but with increasing age, the location of the disease moves to the sides of the branch mouths (Barnes and Weinberg, 2001, Cremers et al., 2011). Additionally, the pattern of macromolecule uptake by the rabbit aortic wall also changes with age, and in the same way (Sebkhi and Weinberg, 1994a, 1996, Ewins et al., 2002, Clarke et al., 2012, Bailey et al., 2015). However, the effect of age on the pattern of hotspots and its dependence on mitosis has not been examined and is the topic of research aims (1) and (2).

1.4 Heterogeneity of medial mass transport properties as a local risk factor

A more thorough review of the literature is provided as the introduction to chapters 5 and 6. What follows here is a brief survey as motivation for research aims (3), (4) and (5) presented in section 1.5.

Another possible local risk factor is inhomogeneity in arterial media structure, leading to spatial variation in the transport properties of the media, which would have an affect on macromolecular accumulation within the subendothelium. As described above, there are two gradients that drive mass transport in the arterial wall. To determine which of the two resulting fluxes dominates LDL transport through the rabbit thoracic aorta, Tedgui and Lever (1985) performed a set of experiments in which a pressure gradient and a concentration gradient of radioisotope-labelled albumin were set up in opposing directions such that the diffusion of the

radiotracer opposed the radial convective water flux. The two processes were allowed to reach a steady state and radioactivity was then measured in slices taken through the wall thickness. The Péclet numbers (4.12-11.25) derived from these measurements suggest that advection is the dominant process in the arterial wall. This observation was confirmed by more recent studies (Baldwin et al., 1997, Hwang et al., 2001). Therefore understanding transmural water transport is a key step in understanding the macromolecular transport in the arterial wall. Determining transport properties of the individual layers of the wall would also give an insight into which layer represents the dominant resistance layer of the whole wall and therefore have a greater role in determining areas prone to greater macromolecular accumulation.

Early experimental work (Tedgui and Lever, 1985, Shou et al., 2006) measured hydraulic conductance (L_p) in arteries before and after denudation of the endothelium in order to determine the hydraulic resistances of the endothelium. However, these studies were limited by experimental artefacts: removal of the endothelium exposes the media to elevated hydraulic flux, compacting the structure, and removes the source of an array of vasodilators and constrictors. Numerical studies calculating fluid flow through porous structures representing the arterial wall aimed to avoid such experimental artefacts (Wang and Tarbell, 1995, Huang and Tarbell, 1997, Dabagh et al., 2009b). However, the simulations in these studies were performed using idealised 2D/3D geometries with cylinders in regular arrays representing the VSMCs in the media. Developing methods to overcome these limitations and applying them are the subjects of research aims (3) and (4).

As the target of many vasoactive mediators, spatially varying VSMC tone is another potential risk factor for macromolecular accumulation: local variation in vasoconstrictor/dilator concentrations would create local variations in tone leading to changes in the medial structure and therefore its permeability (Caro and Lever, 1983, Baldwin et al., 1983, Caro et al., 1980). For example, The effective radius of action of NO can be roughly estimated from its diffusion coefficient ($8.48\times10^{-10}\mathrm{m}^2/\mathrm{s}$, Liu et al., 2008)and *in vivo* half-life (∼2s, Thomas et al., 2001) to be $\sim 100\mu m$, about 1.25× the radius of an EC. Thus gradients of such vasoactive signalling molecules could elicit responses of VSMC tone of approximately the same scale. This is the topic of reseach aim (5).

1.5 Research Aims

The research aims of this thesis are as follows:

1. To investigate if there are age-related changes in the pattern of endothelial permeability hotspots for small macromolecules (67 kDa) that can account for the age-related patterns of total uptake and lesions;

2. To investigate whether mitotic cell distribution can account for age-related changes in small molecule (67 kDa) hotspot distribution and age-related changes in lesion prevalence;

3. To investigate if there are age-related changes in the distribution of endothelial permeability hotspots for large (2 MDa) macromolecules that are similar to those for small macromolecules;

4. To develop experimental, imaging and numerical tools to study the mass transport properties of the arterial media;

5. To determine the influence of transmural pressure-induced structural change in the media on the hydraulic resistance of arterial wall components;

6. To determine the influence of VSMC contraction-induced structural change in the media on the hydraulic resistance of arterial wall components.

1.6 Outline

The six research aims set out in section 1.5 are each addressed in chapters 2 to 6.

Chapter 2 begins with an introduction of the leaky-junction cell turnover hypothesis, which attributes foci of high endothelial permeability to transiently widened EC junctions during cell cycle events, and a review of the supporting evidence. Changing spatial patterns of macromolecule uptake and lesion prevalence with age have been previously reported, leading to our investigation of the hypothesis that patterns of mitosis and small molecule hotspots change with age in rabbits in the same way as lesions. Several tools developed for this study are presented and applied: (1) an automated spot segmentation algorithm to identify foci of elevated transendothelial transport of fluorescent tracers was used to identify hotspots from a background of varying intensity; (2) a statistical method accounting for spatial autocorrelation was developed in collaboration with other group members to evaluate the significance of spatial correlations between pairs of 2D images.

Chapter 3 is an extension of the study presented in chapter 2, investigating the patterns of large molecule hotspots and their relation to patterns of mitosis and small molecule hotspot distribution obtained in chapter 2. A simpler automated spot segmentation algorithm, based on global intensity thresholding, was developed to process the much less complex images of large molecule hotspots. A secondary aim of this chapter was to determine if large molecule transport *in vivo* occurs predominantly via a transcellular or a paracellular route. An initial attempt to segment EC boundaries from images of stained arterial tissue is presented as the basis for future work.

The development and validation of experimental, imaging and numerical methods applied in the studies of medial transport are described in chapter 4. The chapter begins with protocols already established in the group. Experimental methods developed for this thesis include: (1) measurement of L_p and P in fully intact *ex vivo* rat abdominal bifurcations; (2) determination of steady state and equilibrium tracer distributions in the arterial wall and (3) fixation of elastic tissue under stress without recoil. The imaging techniques developed include: (1) High-resolution 3D optical sectioning of epoxy-embedded tissue and (2) algorithms to correct

for intensity attenuation with depth for optical sectioning techniques and image volume rotation of high resolution (memory intensive) 3D images. The numerical method, to determine the effective permeability of realistic 3D structures representing arterial medial tissue, presented at the end of this chapter was developed in collaboration with Dr. A Comerford.

The study in Chapter 5 investigates the effect of pressure-induced structural deformation of the arterial media on the hydraulic resistance of the whole wall, the media and (by subtraction) the intima. (The adventitia has a looser structure and is assumed to provide a negligible resistance.) The chapter begins with a justification for focusing on water transport in the arterial wall as an intermediate step towards understanding transmural macromolecular transport and a review of the literature concerning medial transport properties. An overview of the interconnections between the experimental, imaging and numerical methods developed in chapter 4 is then given, arriving at results showing the hydraulic resistance of the two layers and the whole wall. Further, a relationship between medial hydraulic permeability and deformation is derived from a combination of the experimental and numerical results.

Chapter 6 is an extension of the study presented in chapter 5, focusing instead on medial structure changes brought about by VSMC contraction.

Finally, conclusions are summarised in chapter 7 along with suggestions for further work.

Publications: The statistical methods and the combined experimental-numerical methods have been published as a full paper. The Evan's Blue hotspot study and the study examining effects of pressure have been submitted as full papers. The study concerning effects of tone is in preparation as a full paper and has been presented at conferences. The dextran study is in preparation as a full paper.

Chapter 2

Patterns of Endothelial Permeability to Small Macromolecules

2.1 Overview

Current clinical practice, to estimate an individual's risk of death from atherosclerosis-related conditions from *systemic* risk factors, highlights the lack of consensus on a mechanism to account for the *focal* distribution of lesions that characterises the disease. There is considerable evidence that lipoprotein accumulation in the arterial wall is a precursor for atherosclerosis (Steinberg, 2002). In this chapter, we focus on hotspots of high endothelial permeability, and on spatially heterogeneous rates of endothelial cell (EC) mitosis as a possible factor in the distribution of such hotspots. In particular, we examine whether they can account for the age-related patterns of lesion prevalence previously observed around intercostal ostia in rabbit aortas.

2.1.1 Endothelial transport pathways and the cell turnover-leaky junction hypothesis

The EC monolayer forms a barrier between the blood in the lumen and the underlying tissues of the arterial wall. Although small lipid-soluble molecules (eg: dissolved gases, ethanol) are easily able to pass through the cell membranes of the ECs, transendothelial transport of lipid-insoluble plasma solutes is restricted to water-filled channels. Possible routes include active vesicular transport and passive transport through intercellular junctions. Vesicular transport is a transcellular pathway in which macromolecules are encapsulated in vesicles on the apical endothelial surface and transported to the basolateral surface. Tight junctions represent the normal resting state of the EC junctional complex, however due to their physical size (1-2 nm) they prevent the transport of blood-borne macromolecules. Breaks in the tight junction ($\geq$20 nm) should allow the passage of albumin (4$\times$14 nm; DeBlois et al., 1973) but larger macromolecules such as LDL (Stokes-Einstein diameter 23 nm; DeBlois et al., 1973) are unlikely to cross the endothelium through pores of this size.

A second class of intercellular junction was proposed by Weinbaum et al. (1985) in the so-called 'cell turnover leaky junction' hypothesis (CTLJ): temporarily widened cell junctions ('leaky junctions') formed during cell turnover events, such as mitosis and apoptosis, could open up large enough pores in the endothelium to allow the transport of the largest plasma macromolecules, including LDL. Typical dimensions of these leaky junctions were estimated to be 80-1330 nm during mitosis and 15-1000 nm during apoptosis

(Chen et al., 1995), supporting such a possibility. The relative importance for albumin transport of all these pathways was estimated in recent *in vitro* work (Cancel et al., 2007). This cell culture-based study attributed 20 % to vesicles, 36 % to breaks in the tight junction and 44 % to leaky junctions. More significant to the development of atherosclerosis, >90 % of LDL transport was attributed to leaky junctions. However, a drawback of *in vitro* studies is that the cellular junctions in static culture may not be identical to those *in vivo*, leading to a widely known difference in endothelial permeability of up to 2 orders of magnitude. The sensitivity of the EC morphology, junctional complexes and therefore permeability to the biological and mechanical environment provided *in vitro* has been well studied (Albelda et al., 1988, Estrada et al., 2011, Bazzoni and Dejana, 2004). Therefore the absence of flow-mediated shear stress in all aforementioned transwell-based studies and the absence of the native ECM, a major source of cellular signalling to ECs, in all tissue culture studies necessitates the use of *in vivo* experiments.

2.1.2 Observations supporting the CTLJ hypothesis *in vivo*

Stemerman et al. (1986) conducted experiments in rabbit aortas which suggested that LDL crossed the endothelium via routes also taken by the much smaller horseradish peroxidase (HRP, Stokes-Einstein diameter 6.4 nm; Öjteg et al., 1987): uptake of HRP occurred in distinct spots (here termed 'hotspots') 1 min after administration and the concentration of LDL in these HRP hotspots was up to 47 times greater than in HRP-free arterial tissue. Subsequent studies (Lin et al., 1988, 1990) used Evan's Blue dye-albumin (EBA) in place of HRP, taking advantage of the binding affinity of Evan's blue dye (EBD) to collagen and elastin in the subintimal space: EBD binds preferentially to elastin and collagen on entering the wall (Heinle and Lindner, 1984), leaving a permanent record of its site of entry rather than reacting with or diffusion through in the underlying tissue. These studies showed that hotspots occurred in association with both apoptotic and mitotic ECs: after 3-5 minutes of EBA circulation, 99 % of mitotic cells, identified by nuclear haematoxylin staining (Lin et al., 1988), and 63 % of dead or dying cells, identified by indirect IgG immunohistochemistry (Lin et al., 1990), were associated with EBA hotspots [1]. Furthermore, these mitotic and dead or dying cells accounted for 30 % and 37 %, respectively, of all EBA hotspots. A further study using ^{125}I-LDL reported that 80 % of mitotic cells were associated with LDL hotspots, with mitotic cells present in 45 % of hotspots (Lin et al., 1989). However, a similar study by Truskey et al. (1992) found that only approximately 25 % of leakage sites were associated with mitosis, a much lower percentage.

A second body of evidence supporting this theory arises from comparing the results from studies of mitotic cells, uptake and lesion distributions around athero-prone sites (eg: aortic ostia). Petroff (1922) used the intravital dye Trypan Blue, an isomer of Evan's Blue dye (EBD), which predominantly binds to

[1] This technique is an indicator of membrane permeability to IgG; high permeability allows entry of IgG into the cell and the subsequent cytoplasmic binding of the IgG. Its application to detect dead or dying cells relies on the increase in membrane permeability associated with cell death however this could occur by apoptosis or simply necrosis so this data should not be interpreted as a measure of apoptosis, rather an indicator of it.

serum albumin in the plasma (Lindner and Heinle, 1982) and acts similarly to EBA in the studies mentioned above. The dye was preferentially taken up by the flow divider at arterial branch points, a location known to be particularly prone to developing atherosclerotic lesions in the cholesterol-fed rabbit (Anitschkow, 1933). Although the study was conducted using frogs, the result was subsequently repeated in young pigs (Bell et al., 1972). The observations that mitosis rates are higher in areas of Evan's Blue dye-albumin (EBA) uptake by the pig aortic wall (Caplan and Schwartz, 1973), viewed in tandem with those of Petroff (1922) and Anitschkow (1933), suggests a possible mechanism linking mitosis, hotspots and lesions.

2.1.3 Hotspots and disease patterns

Previous work in this group has shown that the pattern of lesions in cholesterol-fed rabbits changes with age. Lesion prevalence is highest downstream of aortic ostia in young animals but with increasing age, the location of the disease moves to the sides of the branch mouths (Barnes and Weinberg, 2001, Cremers et al., 2011). Looking at the locations of spontaneous lesions that occasionally affect rabbits on a normal diet, a similar switch is seen (Barnes and Weinberg, 1998) and it parallels a comparable change with age in human aortas (Sinzinger et al., 1980, Sloop et al., 1998, Weinberg, 2002). Furthermore, the pattern of macromolecule uptake by the rabbit aortic wall also changes with age, and in the same way (Sebkhi and Weinberg, 1994a, 1996, Ewins et al., 2002, Clarke et al., 2012, Bailey et al., 2015). HRP (Barakat et al., 1992) and LDL (Herrmann et al., 1994) hotspots occur at a particularly high frequency downstream of branch points in young rabbits. However, the effect of age on the pattern of hotspots and its dependence on mitosis has not been examined.

This chapter investigates the hypothesis that patterns of mitosis and EBA hotspots change with age in rabbits in the same way as lesions, and examines the proportion of total uptake that occurs via hotspots.

2.1.4 Technical innovations

A range of technical innovations were employed in this study. With regards to EBA hotspot identification: to increase sensitivity, EBD was detected from its fluorescence rather than its absorbance; to preferentially detect EBD bound to elastin in the inner wall, *en face* confocal microscopy was used in conjunction with a maximum intensity projection; to remove observer bias, hotspots were identified and their area and intensity were quantified by an objective, automated method of image segmentation. Further, a DNA synthesis marker was added to drinking water to record mitotic events over several days rather observing a snapshot of cells in mitosis at the time of death. Finally, comparisons between patterns of hotspots, mitosis and lesions were made by rigorous statistical methods (Rowland et al., 2015) that account for autocorrelation and avoid assumptions of linearity.

2.2 Methods

2.2.1 Animals and diet

All animal procedures were conducted by Dr S G Cremers. They complied with the Animals (Scientific Procedures) Act 1986 and were approved by the Local Ethical Review Panel of the University of Reading. Twelve immature (70±3 days, 2.10±0.09 kg; mean±SEM) and twelve mature (333±17 days, 4.00±0.16 kg) male New Zealand White rabbits (HSDIF strain, Harlan) were individually housed at 18±2 °C under a 12 h light cycle and were fed a normal laboratory diet (9603 TRB; Harlan Teklad, Bicester UK) *ad libitum*.

2.2.2 EBA uptake experiments

2.2.2.1 EBA preparation and animal procedure

EBA was prepared by mixing EBD (Sigma) with bovine serum albumin (BSA, fatty acid adsorbed, First Link UK Ltd) in a 14:1 molar ratio in Ringers solution (composition in g/L: NaCl, 9.0; KCl, 0.25; $CaCl_2$, 0.25; $NaHCO_3$, 0.1). Five conscious, unrestrained rabbits in each age group were each administered 100 mg kg^{-1} (2.4 ml kg^{-1}) EBA via the marginal ear vein. This step was omitted in an additional 2 animals in each age group that were used to assess levels of naturally-occurring tissue autofluorescence. After 8 minutes, all rabbits were given heparin (2000 USP units, Sigma) and, after an additional 2 minutes, an overdose of sodium pentobarbital (Euthatal, approx. 200 mg kg^{-1}, Rhône Mérieux) by the same route.

Immediately after confirmation of death, a ventral midline incision was made, the abdominal organs were deflected and the diaphragm removed to reveal the aorta. The aorta was cannulated retrograde and flushed by perfusion with ∼50 ml of Ringers solution containing heparin (2000 USP units, Sigma) from a reservoir suspended 90 cm above the animal. It was then fixed *in situ* by perfusion with 10 % buffered formalin (Sigma) for 30 minutes through the same cannula from a fixative reservoir also placed 90 cm above the animal. The aorta from the point of cannulation to the descending arch was excised and post-fixed in 10 % formalin for 24 h. Finally, the tissue was rinsed with phosphate buffered saline (PBS, 0.15 M, pH7.4, Sigma) to remove excess fixative and cleansed of loose adventitial tissue.

2.2.2.2 *En face* confocal imaging

Imaging was also conducted by Dr S G Cremers. Each aorta was opened longitudinally along its ventral surface and placed luminal surface down in a coverslip-bottomed petri dish containing PBS. The tissue was held flat by placing a glass disk on top of it, and examined *en face* with an inverted confocal microscope (TCS SP2, Leica Microsystems). To image the region surrounding each intercostal branch ostium, EBD fluorescence was excited at 633 nm, and emission at 660-690 nm was recorded with a ×10 objective, using a 2×2 tile scan to increase the field of view to 3×3 mm (944×944pixels). Z-stack images were acquired with each slice being approximately parallel to the endothelial surface. Photomultiplier tube gain was set for

each image volume so that a few pixels saturated in the brightest slice, making maximum use of the dynamic range of the detector. A maximum intensity projection (i.e. an *en face*, 2-dimensional map comprising only the brightest pixel in each depth-wise column of pixels) was obtained from the confocal image stack for each branch.

2.2.3 Analysis of EBA images

Analysis methods were developed and employed as part of this PhD project.

2.2.3.1 Flatfield correction

To adjust maps for spatial variation in the sensitivity of the microscope, each tile had to be divided by an equivalent tile of a uniformly fluorescing object. Ideally, this flatfield correction would be done by first imaging a Chroma slide, known to have spatially homogeneous fluorescence, to create a correction tile. All image tiles would then be divided by the correction tile to remove any effects of spatial variation in the sensitivity of the microscope. The mathematical possibility that division by a zero-valued pixel in the flatfield correction tile does not occur unless there is broken detector. As optical components in microscopes are known to change in alignment with routine use, this should be done concurrently when obtaining the dataset. For the EBA images, this was not done.

As an alternative to the ideal case, the flatfield correction tile was generated from the autofluorescence images from the four animals not receiving tracer. Variations in autofluorescence around branches are small (Clarke et al., 2012) and were reduced further by averaging tiles from different locations around the ositum. The averaging procedure is illustrated in figure 2.1. The ostium was situated within one quadrant of each of the four tiles in every 2×2 tile scan (Fig 2.1A); these quadrants were masked. Since a different quadrant was affected in each tile, superimposing the 4 masked tiles then effectively resulted in the sum of three branch-free tiles (Fig 2.1B, C). Averaging the results from all 67 branches produced the final flatfield image (Fig 2.1D). Figures 2.1E and F illustrate, respectively, a tile scan of EBA fluorescence before and after correction.

2.2.3.2 Automated hotspot segmentation

Ostia were masked, using manual segmentation guided by edge detection, since hotspots within intercostal arteries were not of interest. Hotspots in the remaining area were identified using the thresholding method of Otsu (1979), which minimises the combined intraclass variance for the above-threshold and below-threshold groups. The method can be generalised to compute multiple thresholds, dividing pixels into several levels on the basis of their intensities. Since the fluorescence of non-hotspot uptake varied from region to region, and was superimposed on the fluorescence from the hotspots themselves, the multi-threshold method was applied locally, in a sampling window, to remove local variation, and then globally to separate adjacent hotspots. The use of four levels in both local and global thresholding and the size of sampling window were chosen on the

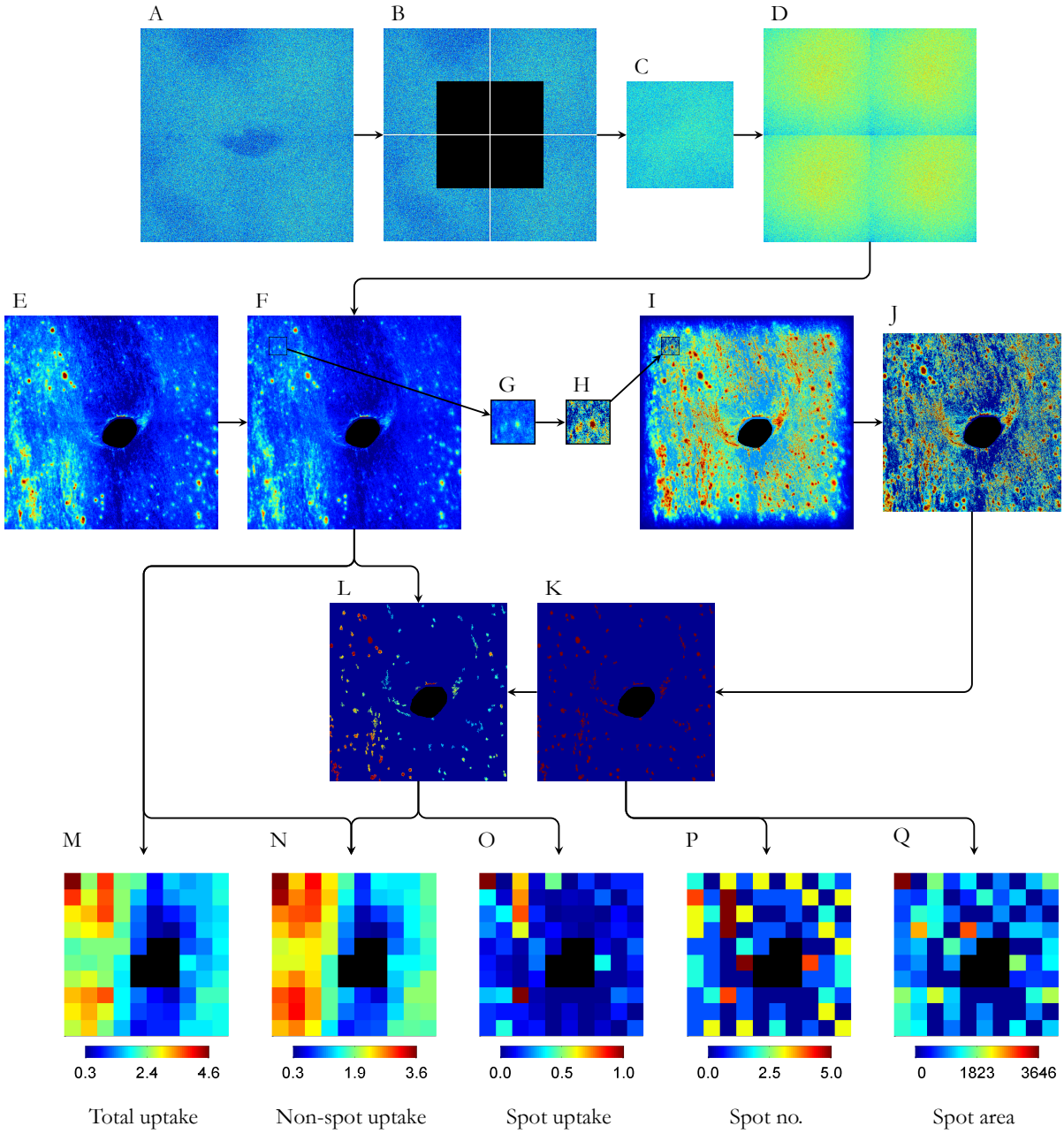


Figure 2.1: Image processing steps involved in hotspot segmentation. They are illustrated using typical en face images from mature animals, with mean aortic flow from top to bottom. A: Maximum intensity projection of a 2 x 2 tile scan covering a 3 x 3 mm area of aortic wall centered an intercostal branch ostium, showing autofluorescence in an animal not administered tracer. B: Superposition of mask to block the ostium, and separation of constituent tiles. C: Average of all four quadrants from (B). D: 2 x 2 tile flatfield image reconstructed from 4 images of the type shown in (C) but using data from all 67 autofluorescence branches. E: Typical image from a mature animal administered tracer. F: The corresponding flatfield- corrected image (inset:100 x 100 pixel sampling window). Total uptake (M) is quantified using this image. G: 100 x 100 pixel image cropped from F. H: 4- level Otsu thresholding applied to (G). I: Reconstruction of all 100 x 100 pixel images after 4-level Otsu thresholding. J: The same image after removal of a 100-pixel-wide border, to eliminate the edge artifact introduced during local thresholding. K: A binary image showing spot locations, used to generate spot counts (P) and to measure spot areas (Q). L: The top level of pixels in (J), which are interpreted as hotspots, coloured by their original intensities in (F) and used to quantify spot uptake (O). N is obtained by subtracting (L) from (F) and then calculating uptake as in image (M).

basis of convergence testing (see Validation, below).

The implementation is illustrated in figure 2.1. A 100×100 pixel (318×318 μm) sampling window was placed in the top left hand corner of the whole image (Fig 2.1F, G). The size of this window was chosen based on the results of preliminary validation tests, detailed in section 2.3.2. The pixels of this sub-image were placed in one of four intensity categories by computing three Otsu thresholds for the sub-image (Fig 2.1H), giving each pixel a value from 0-3; these values were placed in the corresponding pixels of a new image (Fig 2.1I). The sample window was then moved one pixel to the right and Otsu thresholds were recalculated. The new Otsu values were again placed in the new image, being added to the values obtained in the previous sub-image for each pixel that had been examined twice. This process was repeated, moving the sample window in a raster, until the whole of the original image had been covered. Each pixel in the new image could have had a value between 0 and 3 times the number of times it had been included in a sample window. A 100-pixel wide border was cropped from the new image to ensure that all pixels had been included in the same number of local thresholding calculations (Fig 2.1J). To determine which of these locally-thresholded values should indicate the presence of a hotspot, three Otsu thresholds were computed for the entire new image, placing pixels into four categories; pixels in the top category were considered to be part of a hotspot.

Connectivity rules for 8-connected pixels were applied in the resulting binary image to identify apparent hotspots. These were filtered by area to reduce noise: apparent hotspots smaller than 50 pixels (506 μm^2), which is similar to the average surface area of EC in the vicinity of a rabbit intercostal ostium (Nerem et al., 1981), were excluded. A filter of 450 pixels (4552 μm^2) was also applied in some cases to identify a subpopulation of larger spots (not shown in Fig 2.1). The number, intensity and area of hotspots were computed from the filtered binary image (Fig 2.1K). Validation experiments with a series of test images demonstrated the ability of the method to correctly identify the original number of spots and their areas despite the spots having variation in size and shape and the addition of high and low frequency noise (see section 2.3.2).

The filtered binary image was applied to quantify non-hotspot transport: it was used to mask the flatfield-corrected image (Fig 2.1F) to obtain an image of the residual albumin uptake. Finally, a 10×10 grid was superimposed on the resulting maps, giving squares of 238×238 μm, the same size as the grid within which mitotic events were counted.

2.2.4 Cell division experiments

These experiments were conducted by Dr S G Cremers.

2.2.4.1 Animal procedures and tissue preparation

5-bromo-2- deoxiuridine (BrdU, Sigma) was added to the drinking water at a concentration of 1.6 mg ml^{-1} for five rabbits in each age group for 48 h. The solution was freshly made twice every day. Animals were then euthanised and their aortas flushed, fixed *in situ* and excised as described in section 2.2.2.1, except that, after

initial fixation, aortas were transferred to PBS and cleaned of loose adventitial tissue without post-fixation. For antigen retrieval, they were immersed in 0.01 M citrate buffer (pH 6.0) for 1 h, opened ventrally, clamped between 2 microscope slides and maintained at 100 °C for 15 minutes.

Immunohistochemistry to stain BrdU-positive nuclei was performed as follows: the tissue was washed in PBS and blocked with normal goat serum (1:100 dilution, Amersham Biosciences, UK) for 30 minutes before incubating with a mouse anti-BrdU monoclonal antibody (Becton Dickinson; 1:20 dilution with 1 % BSA in PBS) for 1 h. Samples were then washed with 1 % BSA in PBS before incubation with fluorescein-conjugated goat anti-mouse IgG (KPL, Gaithersburg, USA; 1:20 dilution in Tris-buffered saline, pH7.6, Sigma) for 1 h. All incubations were conducted at room temperature. Nuclei were counterstained with 0.5 mg ml^{-1} propidium iodide (PI; Eugene, Netherlands) for 1 minute and the tissue studied immediately.

2.2.4.2 *En face* confocal microscopy

Aortas were mounted in glass-bottomed petri dishes as described in section 2.2.2.2. The 2nd and 4th pairs of intercostal branch ostia were examined in all 10 animals, imaging a 12×12 tile scan, centered on each ostium with a ×63 glycerol immersion objective. This gave a field of view of 2.86×2.86 mm, as close in size as practicable to that obtained in the EBA experiments with a different objective. Fluorescein-labelled antibodies were excited at 488 nm and emission was recorded at 510-530 nm; PI-stained nuclei were excited at 543 nm and their emission was recorded at 600-640 nm. The 144 stacks of optical slices were examined for fluorescein and PI fluorescence, and the number and location of fluorescein-stained nuclei in the endothelial layer of each 238×238 μm tile (462×462 pixels) was recorded.

2.2.5 Spatial correlation statistics

These techniques were developed as part of the present PhD, but in collaboration with E Rowland, Y Mohamied and Dr E Bailey.

2.2.5.1 Fundamental problems in comparing biological image data

A fundamental problem encountered when evaluating the statistical significance of correlations between two sets of images is spatial autocorrelation. This arises due to an inherent property of image data: for a continuously varying variable (eg: EBD fluorescence intensity) discretised over a grid of pixels to form an image, adjacent pixels in any given image are more likely to have similar values than would be expected to occur by chance. Therefore adjacent pixels cannot be regarded as being independent of one another. This makes it impossible to apply standard statistical tests, which rely on having independent samples, to compare a pair of images. To do so would increase the chance of producing spurious significant correlations: the higher the level of spatial autocorrelation, the higher the chance of generating false positive results.

A second problem stems from the need to aggregate data and the effect that has on the average maps:

Since we cannot obtain the two sets of data in each animal without one biological intervention affecting the other, we are forced to collect data sets from different animals and therefore we do not have paired data for statistical comparisons. (For example, if we were to perform EBA uptake experiments on cholesterol-fed rabbits with the intention of getting paired lesion prevalence and EBA data, the biological effects of the cholesterol diet could have influenced the EBA data (Sebkhi and Weinberg, 1994b): diet-induced lesions would introduce spatially varying endothelial permeability that is not present in naive vessels and the interpretation of the results would be difficult.) Instead, we collect individual maps from multiple animals to construct each dataset and then analyse correlation between the two sets by constructing average maps for each set. However, as averaging reduces variance, there is a tendency for such correlations to be biased towards stronger correlations.

Regarding this study, the two problems discussed only apply to unpaired images; spatial autocorrelation does not inflate the significance when a t-test is applied to correlation coefficients calculated from pairwise comparisons (Rowland et al., 2015). That is, we only need to overcome the problems of spatial autocorrelation and data aggregation when comparing EBA-derived metrics against BrdU and lesion data and when comparing BrdU to lesion data; correlations between EBA-derived metrics can simply be done by calculating pairwise correlation coefficients and applying a t-test on these values.

A final consideration to be taken into account when evaluating statistical significance is the mathematical form of the relation we expect between the two data sets. There is no *a priori* reason to expect a linear relation between any of the data sets in this study. (For example, there is no reason to expect a 238×238 μm grid square containing 2 mitotic nuclei to have EBA hotspots twice the area of a grid square containing only 1 mitotic nucleus). However, it would be reasonable to suggest some monotonic relationship. (eg: more EBA hotspots in grid squares containing more mitotic nuclei.)

2.2.5.2 Linear vs monotonic relations

The methods described in this section and section 2.2.5.3 were predominantly work by E Rowland with help from Y Mohamied (DT-CWT, decorrelation length based sampling and bootstrapping), Dr E Bailey (Decorrelation length based sampling and bootstrapping) and the author (IAAFT, decorrelation length based sampling and bootstrapping) and was published in a recent paper (Rowland et al., 2015). What follows here is a brief summary.

In each of the following methods to overcome spatial autocorrelation (Section 2.2.5.3), Pearson's correlation coefficient was calculated between the ranked datasets ($\{\boldsymbol{x}|x_1, x_2, ..., x_{N_{pix}}\}$ and $\{\boldsymbol{y}|y_1, y_2, ..., y_{N_{pix}}\}$). That is, for a correlation between two images, the data in each image was first ranked with the lowest value assigned a rank of 1 and the highest value receiving a rank of N_{pix}, the number of pixels in the image. Tied values were each assigned the mean of the ranks that they would otherwise have occupied. This is also known

as Spearman's rank correlation coefficient, ρ, and is calculated as in equation 2.1:

$$\rho = \frac{\sum_{i=1}^{N_{pix}} (x_i - \bar{x})(y_i - \bar{y})}{\sqrt{\sum_{i=1}^{N_{pix}} (x_i - \bar{x})^2} \sqrt{\sum_{i=1}^{N_{pix}} (y_i - \bar{y})^2}} \tag{2.1}$$

By ranking the pixels, any assumptions of linearity in the relation between the two variables are discarded but monotonic relations are maintained.

The significance, p, of correlation, ρ, was then evaluated using a Student's two-tailed t-test by calculating Student's t-statistic:

$$t = \rho \sqrt{\frac{N_{pix} - 2}{1 - \rho^2}} \tag{2.2}$$

From Student's t-distribution, we can then obtain a p-value associated to the correlation coefficient, ρ.

2.2.5.3 Methods to overcome spatial autocorrelation

Two general approaches are available to account for spatial autocorrelation when correlating images. The first aims to remove spatial autocorrelation by re-sampling the images to obtain a subset of pixels that are independent of one another. These subsets can then be used to calculate ρ and associated p values as described in section 2.2.5.2. A method based on this approach was developed previously by Peiffer et al. (2013a) and modified more recently by Rowland et al. (2015): A single decorrelation length (l_{dec}) is found in the image sets that represents the minimum distance between pixels that are not correlated. The number of pixels drawn at random with replacement is then set at $\frac{N_{pix}}{l_{dec}^2}$. (Note that N_{pix} represents an area, making $\frac{N_{pix}}{l_{dec}^2}$ dimensionless.) This subset of pixels is then used in calculations to obtain a correlation coefficient (See section 2.2.5.2). Repeated re-sampling is used to generate multiple subsets of data to obtain a distribution of ρ and p values and the median values are taken to represent the correlation of the original datasets and its significance respectively.

An equivalent method was proposed by Clifford et al. (1989) and modified by Dutilleul et al. (1993), based on the fact that spatial autocorrelation has the same effect as reducing the number of degrees of freedom in the t-test. Therefore a simple correction to the number of degrees of freedom can be made by substituting N_{pix} with an effective sample size, m. For comparison with our modified method of Peiffer et al. (2013a), $m = \frac{N_pix}{l_{dec}^2}$. The advantage of this method is that a p-value is evaluated directly from one calculation without the need for repeated re-sampling and is therefore more computationally efficient. ρ is largely insensitive to l_{dec} and can also be evaluated directly from the original datasets (Fig 7, Rowland et al., 2015).

Both of the methods described so far rely on there being a single de-correlation length and are therefore

unsuitable for images with autocorrelation occurring over a range of length scales. Further, de-correlation length is not necessarily isotropic, with images commonly having different de-correlation lengths in each direction, that is, they have features which have some orientation within the image frame. From initial visual inspection of EBA and BrdU fluorescence images and lesion prevalence maps, no single de-correlation length could be applied to each image that would apply in all directions so these two methods were not applied in this study.

The second general approach addresses the issue of spatial autocorrelation at the hypothesis testing stage by incorporating spatial autocorrelation into the null hypothesis. In such methods, surrogate datasets are generated in which the spatial autocorrelation of one of the original datasets is replicated. For ease of further explanation, let us suppose we generate a surrogate image, $\boldsymbol{y\prime}$, aiming to preserve the spatial autocorrelation present in the original image, $\boldsymbol{y}$. Multiple surrogate images ($\boldsymbol{y\prime}$)are generated and each correlated with original image $\boldsymbol{x}$ to build a null distribution of ρ values. The correlation of $\boldsymbol{y}$ with $\boldsymbol{x}$ is then calculated to obtain the observed ρ value. Finally, the significance is determined by the proportion of the null distribution as extreme or more than the observed ρ.

Two methods to generate surrogate images were tested: the iterative amplitude adjusted Fourier transform (IAAFT) and the dual-tree complex wavelet transform (DT-CWT). Both methods rely on decomposing the image onto basis functions. In the case of the IAAFT, the decomposition onto sinusoidal functions gives the amplitudes and phase coefficients of the spatial frequencies contained in the original data. The amplitude coefficients encode the image's autocorrelation information such that the square of the amplitudes (ie: the power spectrum of the image) is the Fourier transform of the image's autocorrelation function. The aim is then to preserve this autocorrelation function in the surrogate image by combining the original power spectrum with randomly generated phase coefficients in the range $(0, 2\pi)$ and performing the inverse Fourier transform. The resulting values in the surrogate image are normally distributed due to the randomness of the phase coefficients so the IAAFT method is used to approximately match the surrogate distribution with the original distribution of values. There is a balance between matching the power spectrums or the distributions perfectly so a maximum of 200 iterations was used. Finally, the surrogate images were ranked and correlation coefficients were calculated to construct the null distribution as described above. One issue to note here is that the Fourier transform is not localised in space (ie: the sinusoidal functions are periodic) so can usually only be applied on regular domains. The presence of the ostium in our images is therefore a problem which we overcame by overlaying a zero-valued branch mouth onto the surrogate and re-applying the Fourier transform. The resulting new phase coefficients were then used to generate a new surrogate with the branch mouth preserved.

The second method, DT-CWT, is analogous to the IAAFT method: the image is represented as a series

of wavelets that are localised in both frequency and space. The method is therefore suited to irregular domains without the need for the workaround required by the IAAFT method. A set of wavelets that can be easily modified by simple transformations is used to describe the image: at a given location within the image, a coefficient indicating how well the wavelet matches the local signal is computed. By shifting the wavelets over the entire image, a grid of these detail coefficients (called a sub-band) is computed, approximating the whole image as a summation of these wavelets, modified by the coefficients. To capture details at greater length scales, the process of decomposing the image can be repeated on the image after halving the resolution. Repeating this halving process, a hierarchy of sub-bands is produced. The set of wavelets used, consisting of six basis wavelets, are described in (Kingsbury, 1998) and produce six complex-valued sub-bands at each length scale. Similar to the IAAFT method, the sum of the squared magnitudes of the coefficients gives the power spectrum which, if preserved, maintains spatial autocorrelation. Analogous to introducing random phase coefficients in the IAAFT method, the detail coefficients were permuted within each sub-band corresponding to the four largest length scales. To account for the branch mouth, detail coefficients at locations within the branch mouth were excluded (Breakspear et al., 2004). The surrogate images were then produced using the inverse transform. Finally, as in the IAAFT method, the distribution of values in the surrogates was adjusted to match that of the original.

A final method that is particularly suited to correlations between aggregated unpaired maps uses a bootstrapping approach to estimate the sampling distribution of ρ in the population: A bootstrap sample was drawn from each of the datasets being compared. For each bootstrap sample, images were sampled from the dataset with replacement (ie: any image within the dataset could be selected multiple times in the bootstrap sample) and average maps were constructed from the images selected and correlation coefficients were calculated for the two resulting average maps. By repeating this bootstrap sampling multiple times, the distribution of ρ is estimated. The number of repetitions required (35000) was decided upon by convergence of the median ρ, which is the value that describing the correlation between the two original datasets. Finally, the 2.5 and 97.5 percentiles were used to form the 95 % confidence interval.

The advantage of the bootstrapping method over the surrogate image-based methods is the ability to construct a confidence interval, which is superior to a single p-value since it describes the uncertainty around an estimate of ρ, rather than just performing a hypothesis test. Therefore bootstrapping was applied to all correlations of unpaired datasets in this study.

2.2.5.4 Application of bootstrapping to evaluate significance of correlations

To enable comparison of images of differing resolution and size, datasets were cropped and re-sampled to obtain 10×10 grids covering a 2.4×2.4 mm region of interest (ROI) centered on the ostium. To obtain lesion prevalence maps, the same procedures were conducted for the maps obtained in our previous work

(Cremers et al., 2011), in which 8 immature (64 days, 1.79±0.01 kg) and 9 mature (183 days, 3.63±0.07 kg) male New Zealand White rabbits of the HSDIF strain were fed a normal diet supplemented for 8 weeks with 1 % cholesterol. Arteries were dissected as above and stained for 1 h at 4 °C in a 1 % solution of Oil Red O in 60 % triethyl phosphate, destained for 30 min in 60 % triethyl phosphate and re-equilbrated with PBS. Samples were then imaged *en face* on a flatbed scanner (Perfection 1660 Photo, Epson).

Pair-wise rank correlation was used to determine the spatial correlation between pairs of hotspot metric maps and 95 % confidence intervals (CIs) were calculated using the Fisher transformed z' statistic. Paired correlation was not possible for comparisons between hotspot, mitosis and lesion maps, so an r-statistic distribution was estimated, using the bootstrapping method to calculate 95 % CIs as described above. When this method is applied to unpaired data, it gives more conservative estimates of the CIs than would have been calculated if a paired test had been possible.

2.3 Results

2.3.1 Animals

One immature rabbit (CUKO) had >8 times as many BrdU-positive nuclei as the average for the group, and nearly 5 times as many as the rabbit with the next highest number. It was determined to be an outlier by Chauvenet's criterion [2] and excluded from all further analysis.

2.3.2 Validation of segmentation method on test images

A convergence test was run on a subset of images that examined the effect of the number of Otsu levels on the total number and area of hotspots. Figure 2.2 details the outcomes of using 2 to 5 Otsu levels. In each case, the number of levels used for global thresholding was the same as that applied in the local thresholding. This paring was based on inspection of the image histogram after local thresholding: for example, when four local levels were applied, the resulting image histogram had four distinct populations of pixel intensities, so four global levels achieved the best separation of these populations. An example histogram is shown in figure 2.3.

For low numbers of Otsu levels (eg: two), the method was inherently unstable due to sampling effects. Increasing the number of Otsu levels attenuated this effect and convergence was subsequently achieved. The use of four levels in both local and global thresholding identified a substantially smaller number of hotspots than the use of fewer levels, but using more levels did not change the result. Thus we concluded that using 4 Otsu levels in each stage was optimal. Effects of local image size were also investigated systematically; there was a strong influence of size on segmentation for sizes up to 100 pixels, so this value was chosen for the

[2] Chauvenet's criterion is a statistical test applied to experimental data that assesses whether an extreme data point, $x_{extreme}$, is in fact an outlier. Assuming the data, x_i, are normally distributed with mean, μ, and standard deviation, σ, if $p(x = x_{extreme}) \times n < 0.5$, where n is the total number of data points, the extreme data point should be excluded from the dataset.

Immature

Group	Identifier	Age [days]	weight [kg]
EBA	XIJJ	78	2.62
EBA	XIJM	88	2.48
EBA	XAWB	73	2.23
EBA	XBVJ	60	1.94
EBA	XAEV	59	1.66
BrdU	CUKO	67	1.96
BrdU	CUJW	70	2.17
BrdU	CUJH	70	2.06
BrdU	CUJF	73	2.15
BrdU	CUJV	73	2.27
AF	XGLW	48	1.58
AF	XGMG	76	2.53
mean		70	2.10
s.d		3	0.09

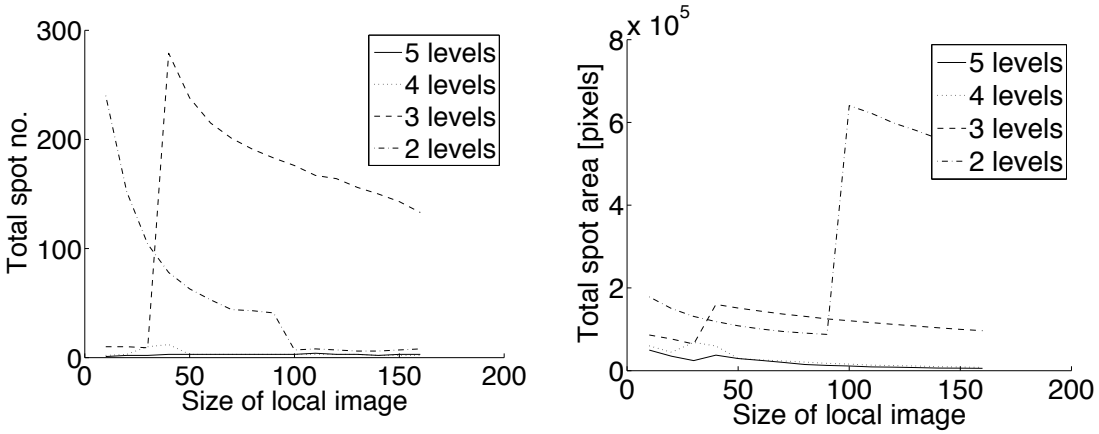
Mature

Group	Identifier	Age [days]	weight [kg]
EBA	XBQK	366	5.42
EBA	XAZS	392	3.86
EBA	XBIS	378	4.00
EBA	XAXD	378	3.87
EBA	XSCM	429	3.85
BrdU	CBHF	307	3.43
BrdU	XJBV	365	4.72
BrdU	4472	285	3.62
BrdU	4473	285	3.78
BrdU	4474	285	3.87
AF	XBAK	288	3.65
AF	YZEE	240	3.91
mean		333	4.00
s.d		17	0.16 8

Table 2.1: Summary of rabbit data. In the immature BrdU group, mean and standard deviation are given excluding CUKO as the data from that animal was determined to be outliers by Chauvenet's criterion

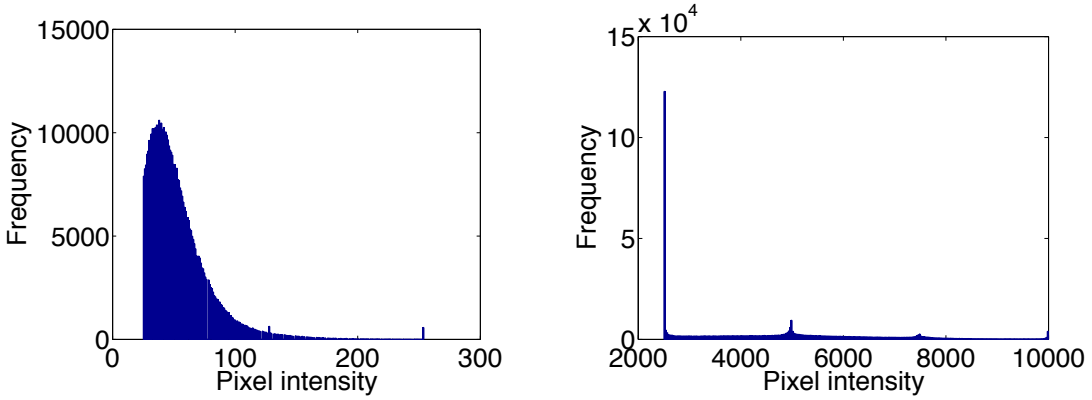
main study.

A series of test images were used to assess the accuracy of the method in determining the number and area of hotspots. Images containing a known number of spots were superimposed on a background with low frequency noise, simulating the more smoothly varying, non-hotspot uptake of EBA. A second test image was generated from the first by adding high frequency noise, to simulate noise introduced during imaging. Different spot sizes and shapes were also used. In all tests, the method correctly identified the original number of spots and their areas - an example is shown in Figure 2.4.



a b

Figure 2.2: Determining the optimum number of Otsu levels at both local and global thresholding stages: the total number and area of spots converged when 4-level Otsu thresholds were applied to sub-images > 100 pixels in size.



a b

Figure 2.3: Example image histograms of key steps of EBA image processing algorithm: (a) histogram of an original image (b) Image histogram of the resulting image after application of local Otsu thresholding to the original: in each sampling window, a 4-level Otsu threshold was applied locally. The histogram of the resulting image has 4 distinct peaks.

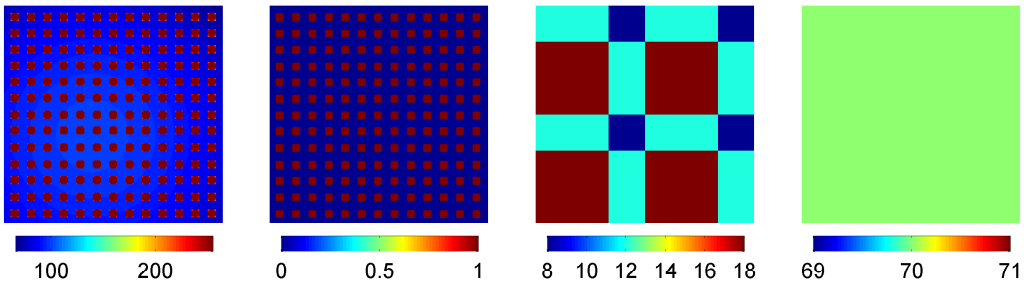


Figure 2.4: Validation of 2-stage thresholding on test images. (a) test image containing a regular grid of square spots of equal size superimposed on a background with low frequency noise. (b) Segmented image shows complete removal of low frequency noise. (c) Number of spots within a 6x6 grid shows that the correct number of spots has been identified. (d) Average areas of spots demonstrates the accurate identification of spot boundaries

2.3.3 Hotspots

Average maps for immature and mature rabbits are shown figures 2.5 and 2.6 respectively: the number of hotspots and their area, and the amount of EBD fluorescence in hotspots, outside hotspots and in both compartments combined are averaged for each grid square. (Note that every map in this and subsequent figures use a colour bar that ranges from the lowest to the highest value for that particular map.) Within each age group, the average maps for all 5 metrics had largely similar patterns. However, there was a strong effect of age: in the immature group, high values for each metric tended to occur downstream of the branch ostium whereas in the mature group they occurred in four patches located at the corners of the maps.

At both ages, the average number of spots reached a maximum of approximately one per grid square (Note that the area of each grid square was $56.644\,\mu m^2$, equivalent to approximately 100 ECs). Overall, however, immature maps had significantly fewer spots than mature maps (mature $= 49.6 \pm 5.3$ spots per branch; immature$= 26.2 \pm 3.8$ spots per branch, mean$\pm$SEM, $p = 0.0005$, Student's t-test; approximately equivalent to 1 spot per 200 and 400 cells, respectively). The maximum average area of hotspots in each grid square differed substantially, being around 250 pixels in immature animals but only 80 in mature ones. However, mean values for spot areas at the two ages were not significantly different (139.6$\pm$8.2 pixels for immature; 125.2$\pm$2.6 for mature). At both ages, when summed over the entire set of images, uptake in hotspots was around an order of magnitude lower than uptake not in hotspots and the non-hotspot uptake therefore accounted for the large majority of total uptake.

2.3.4 Mitosis

Maps of the mean number of BrdU-positive nuclei in each grid square are shown for immature and mature animals in figure 2.7. The data were more sparse than the hotspot metrics and although the maps suggest

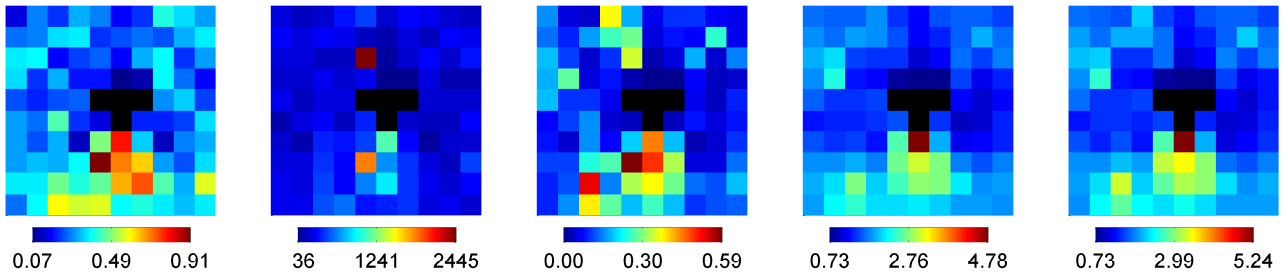


Figure 2.5: Average 10 minute EBA uptake maps for 63 branches from 5 immature rabbits. The maps show a 2.36×2.36 mm area of the aortic wall, displayed *en face* and centred on the intercostal ostium, with mean aortic blood flow from top to bottom. Each map is divided into 10×10 grid squares. The black squares in the ostial region indicate where a branch mouth was present in any image. Spot number is expressed per grid square; spot area is expressed per spot. Spot, non-spot and total uptake are expressed in the same arbitrary units.

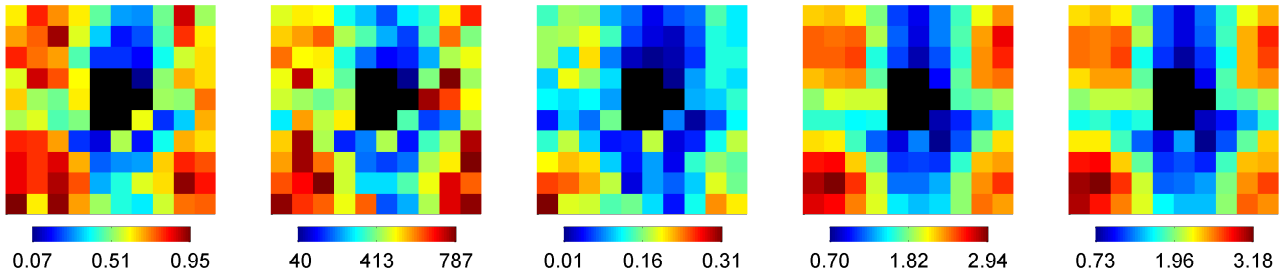


Figure 2.6: Average EBA uptake maps for 58 branches from 5 mature rabbits as in figure 2.5.

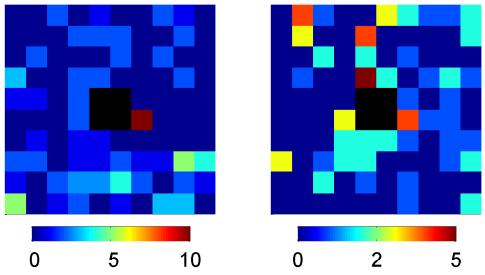


Figure 2.7: Maps showing the average number of BrdU-positive nuclei per grid square for 16 branches from 4 immature rabbits and 20 branches from 5 mature rabbits. The size and orientation of the maps are the same as in figure 2.5.

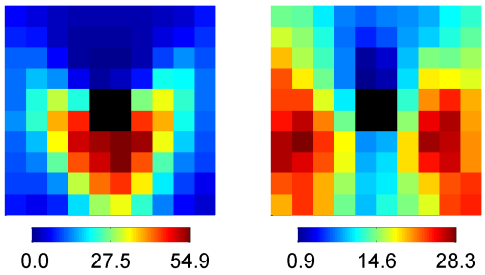


Figure 2.8: Maps (after Cremers et al., 2011) showing lesion prevalence around 112 branches from 8 immature rabbits and 118 branches from 9 mature rabbits. The size and orientation of the maps are the same as in figure 2.5.

that there were slightly more labeled nuclei downstream of the branch in immature animals, and slightly more upstream of the branch in mature ones, these differences were not statistically significant (immature, $p = 0.15$; mature, $p = 0.14$; 1-tailed t-test comparing the top and bottom halves of the maps).

2.3.5 Lesion prevalence

Maps of the frequency of lesion occurrence around intercostal branches in immature and mature cholesterol-fed rabbits are shown in figure 2.8. As discussed in detail in the original paper (Cremers et al., 2011) from which the data were derived, the highest frequencies are seen in an arrowhead-shaped region surrounding the downstream half of the ostium in immature branches, and at the lateral margins of branches in mature animals.

2.3.6 Spatial correlations

Tables 2.2 and 2.3 summarise the median values of Pearson's r and corresponding 95 % confidence intervals for correlations between the different EBD measures, numbers of BrdU-positive nuclei and lesion frequencies for the immature and mature age groups respectively. Correlations within each age group followed the same

trend: all EBD metrics had significant positive correlations with one another and with lesion prevalence; and no significant correlations were observed between the number of BrdU-positive nuclei and any EBD measure . In the mature group there appeared to be a weak negative correlation between the number of BrdU positive nuclei and lesion prevalence, but there was no relation in the immature group. Correlations between corresponding datasets from the two age groups were all insignificant (e.g. mature number of hotspots vs immature number of hotspots) (data not shown).

	Spot area	Total uptake	Non-spot uptake	Spot uptake	BrdU positive nuclei	Lesion prevalence
Spot no.	0.793	0.577	0.515	0.820	0.046	0.388
	[0.678 0.870]	[0.384 0.721]	[0.306 0.676]	[0.718 0.887]	[-0.112 0.208]	[0.282 0.482]
Spot area		0.595	0.515	0.882	0.002	0.253
		[0.407 0.734]	[0.307 0.677]	[0.811 0.927]	[-0.090 0.215]	[0.091 0.478]
Total uptake			0.990	0.687	0.077	0.386
			[0.983 0.994]	[0.529 0.799]	[-0.057 0.217]	[0.261 0.490]
Non-spot uptake				0.598	0.081	0.387
				[0.411 0.737]	[-0.048 0.217]	[0.256 0.493]
Spot uptake					0.034	0.308
					[-0.093 0.180]	[0.170 0.453]
BrdU positive nuclei						0.096
						[-0.079 0.217]

Table 2.2: Correlation coefficients and, in square brackets, associated confidence intervals between all pairs of the parameters measured in immature rabbits. Correlations are not significant if the confidence intervals include zero; however, if both confidence limits are positive, or both negative, then the correlation is significant

	Spot area	Total uptake	Non-spot uptake	Spot uptake	BrdU positive nuclei	Lesion prevalence
Spot no.	0.704	0.549	0.481	0.758	-0.069	0.384
	[0.545 0.814]	[0.338 0.707]	[0.254 0.658]	[0.622 0.850]	[-0.207 0.060]	[0.199 0.516]
Spot area		0.545	0.454	0.830	-0.020	0.396
		[0.334 0.704]	[0.221 0.637]	[0.728 0.896]	[-0.161 0.134]	[0.233 0.522]
Total uptake			0.985	0.646	-0.077	0.376
			[0.975 0.991]	[0.466 0.775]	[-0.234 0.066]	[0.160 0.537]
non-spot uptake				0.533	-0.083	0.376
				[0.319 0.696]	[-0.241 0.060]	[0.161 0.535]
Spot uptake					-0.031	0.320
					[-0.161 0.110]	[0.111 0.487]
BrdU positive nuclei						-0.182
						[-0.298 -0.047]

Table 2.3: Correlation coefficients and, in square brackets, associated confidence intervals between all pairs of the parameters measured in mature rabbits. As in table 2.2, correlations are not significant if the confidence intervals include zero; however, if both confidence limits are positive, or both negative, then the correlation is significant

2.4 Discussion

A significant change with age in the pattern of hotspots of EBA uptake around intercostal branch ostia in the rabbit aorta was the main finding of this study. Hotspots occurred most frequently downstream of the ostium in immature rabbits whilst in mature rabbits, this downstream region was spared - instead the EBA hotspots occurred in two lateral stripes lying either side of the branch mouth, but with the regions immediately lateral to the ostium itself spared. A similar pattern was seen in maps of the number of hotspots, their area and the

amount of tracer within them; within each age group, but not between them, the three measures were highly correlated. Our observations of the immature pattern agree with previous studies, as noted above, but we believe that the mature pattern is novel.

An interesting finding was that, at each age, the map of hotspot uptake correlated with the map of non-hotspot uptake (and hence, of course, with the map of total uptake). Indeed, within each age group the three maps were visually indistinguishable. At minimum, this suggests that there may be common underlying mechanisms, perhaps related to mechanical forces, which determines spatial variation in both hotspot and non-hotspot uptake. The data are also consistent with the speculation that there is not a binary distinction between transport through normal junctions and transport through leaky junctions, but instead a continuum. For example, non-hotspot and hotspot uptake could both reflect transport through inter-endothelial cell junctions, with the width of the junction and hence the local rate of transport varying in a continuous fashion. A continuous distribution of junctional widths and an arbitrary width at which transport was termed hotspot rather than non-hotspot would then also explain the spatial correlation between the number of hotspots, their area and hotspot uptake. (Larger junctions would experience much higher convective velocities, which depend on the 4th power of cylindrical pore radius, leading to faster advection of tracer and, presumably, to greater spreading of the spot.) At both ages, non-hotspot uptake was an order of magnitude higher than hotspot uptake. A possible explanation for this, based on the idea of a continuum of intercellular transport, is that hotspots may be more important for the uptake of larger macromolecules such as LDL since the threshold junctional width would be expected to be larger.

An alternative explanation is that the hotspots identified using our automated method were smaller than those identified in previous studies, and that we therefore counted what previously might have considered non-hotspot uptake in our hotspot uptake, confounding the two mechanisms. For the results described so far, we defined the minimum area of a hotspot to be 50 pixels (506 μm^2), approximately equivalent to the area of one EC. To test whether this area threshold was too small, we also processed images using a nine-fold larger area threshold of 450 pixels (4552 μm^2), equivalent to a circular spot with radius of 38 μm, approximately half of the average radius of HRP hotspots reported by Shou et al. (2007) for 1-minute HRP uptake. (The same time and tracer were used by Stemerman et al. 1986). Although the mean maps grew sparser with the increased filter size, the general patterns of hotspot occurrence remained the same (compare figures 2.5 and 2.6 with figures 2.9 and 2.10), consistent with the concept of a continuum of junctional widths.

Since many previous authors have noted that the location of hotspots often coincides with mitotic endothelial cells, we investigated whether patterns of mitosis change with age in the same way that hotspots do. Instead of taking a mitotic cell-centered view and determining the rate at which hotspots coincided with mitotic events, we used a different strategy, investigating mitosis and hotspots in different animals and then

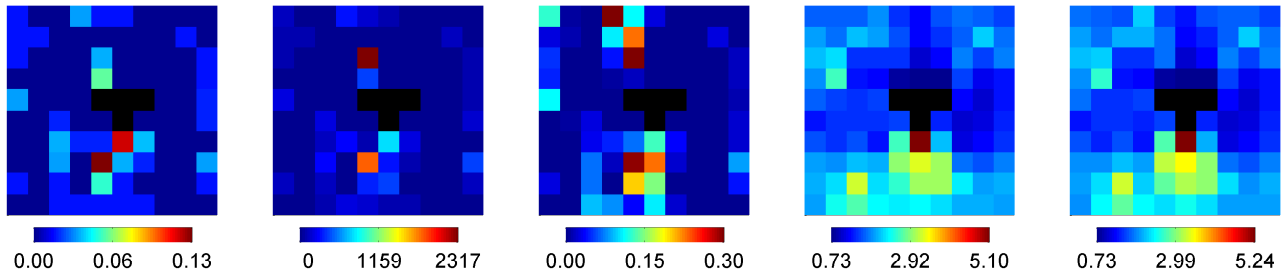


Figure 2.9: Average EBA uptake maps for 63 branches from 5 immature rabbits as in figure 2.5 except that spots were filtered so that only those larger than 450 pixels (4552 μm^2) rather than 50 pixels (506 μm^2) were selected

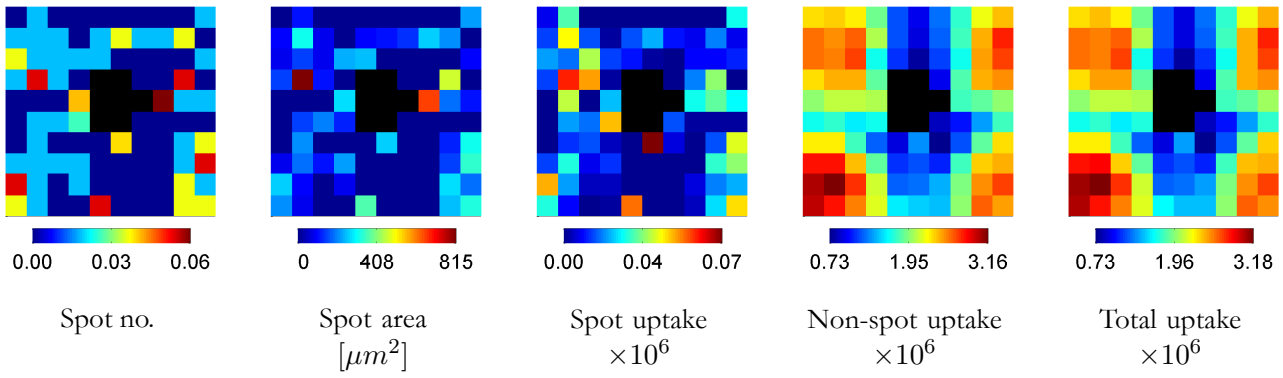
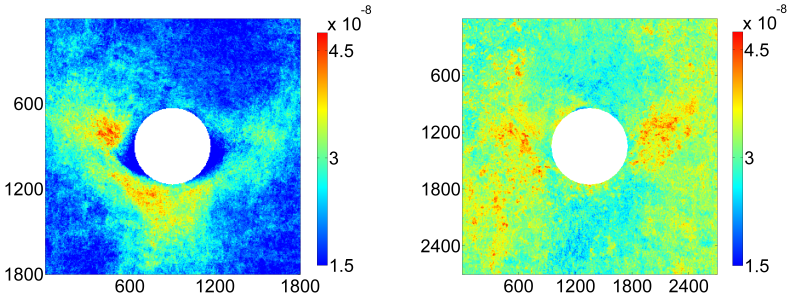


Figure 2.10: Average EBA uptake maps for 58 branches from 5 mature rabbits as in figure 2.6 except that spots were filtered so that only those larger than 450 pixels (4552 μm^2) rather than 50 pixels (506 μm^2) were selected

statistically compared the resulting maps. This has two main advantages: Firstly, a cumulative record of mitosis over several days can be obtained by administering BrdU in dinking water, increasing the number of mitotic events detected. Secondly, using separate animals for the BrdU and EBA studies avoids the possibility that the potentially mutagenic agent would itself modify transport. In our method, BrdU is incorporated into all newly synthesised DNA which we then detect using fluorescence immunohistochemical techniques. Identification of BrdU by immunofluorescence also represents a technical improvement on the methods employed in previous work, in which dividing cells were identified by visual assessment of haematoxylin stained nuclei. A potential weakness to this technique is the risk of generating false positives as BrdU could be incorporated during DNA repair. Estimates for the brightness of nuclei resulting from this were made as follows: DNA repair occurs at 10^5 to 10^6 bases per nucleus per day. The rabbit genome contains approximately 3×10^9 bases so over 2 days the expected intensity of a unreplicated nucleus would be about 3000 times less intense than a replicated nucleus. Even with the sensitivity of confocal microscopy, this noise is well below the detection limits. Therefore our method is likely to give a lower error rate than manual identification which is limited by observer error.

In either age group, no significant correlation was found between EBA patterns and mitotic cell prevalence. Indeed, unlike the result obtained for the distribution of hotspots, there was no significant difference between the mitosis patterns at the two ages. The lack of correlation between EBA measures and mitosis indicates that mitosis is not the most significant cause of leaky junctions. This does not necessarily disagree with the observation by Lin et al. (1988) that 99 % of the mitotic cells occur within EBA hotspots, since only 30 % of the hotspots they identified had mitotic cells present within them. Since our method of hotspot segmentation is more sensitive than the manual identification used in earlier studies, we have identified more hotspots per unit area so it is likely that an even smaller percentage of hotspots in our data had mitotic cells occurring within them. Indeed, the average number of mitotic cells per branch was 20.6 % of the average number of hotspots per branch in the immature group and 7.5 % in the mature group, despite the 48-hour window for detecting mitosis and the 10-minute window for hotspots. (The averages were 6.2 mitotic events per immature branch and 3.9 per mature branch.) The lack of a strong relation between mitosis and hotspots is consistent with the view that, on the whole, non-hotspot and hotspot uptake is an arbitrary division of a continuum rather than two distinct processes, although of course mitotic (and apoptotic and necrotic) ECs may make a minor contribution that is of a qualitatively different type.

If mitotic events are not the main cause of the change with age in EBA uptake, then other factors need to be considered. Previous studies, done in this group, of the uptake of rhodamine-albumin showed that the mature pattern is dependent on endogenous NO synthesis, and was abolished by the eNOS inhibitor NG-monomethyl-L- arginine, but the immature one is not (Forster and Weinberg, 1997a, Staughton and



Immature Mature

Figure 2.11: Maps (after Bailey et al., 2015) showing patterns of mass transfer coefficients [cm s^{-1}] around intercostal branches from male immature (9 weeks) and mature (16-22 months) rabbits. The map dimensions are given in microns and orientation of the maps are the same as in figure 2.5. White circles represent branch mouths. Each map represents the average of at least 18 branches from at least 4 animals.

Weinberg, 2004). That suggests an age-related change in the signaling events controlling patterns of uptake. However, the transport data were obtained only along the centerline through the branch; a more recent study, employing *en face* mapping of transport, suggested that disruption of the NO pathway was only associated with quite subtle changes to transport in the mature animals (Bailey et al., 2015). Another possibility is that mechanical forces change with age. In rabbits there is a change in the helicity of flow in the descending aorta, reflecting an alteration of aortic taper, and a consequent change in the pattern of wall shear stress around branch ostia, particularly in the degree of how multidirectional the shear stress is during the cardiac cycle (Peiffer et al., 2012, 2013b, Mohamied et al., 2015).

Finally, we consider the relation between EBA uptake and lesion frequency. At both ages, our data show significant positive correlations between maps of lesion frequency and all hotspot measures, non-hotspot uptake and total uptake. The pattern of lesion prevalence was largely similar to the patterns observed in all these measures, being greater downstream of the ostium in immature rabbits and in axial streaks either side of the branch mouth in mature rabbits. However, closer inspection of the maps does reveal discrepancies between the transport and lesion patterns within each age group. In particular, lesion prevalence at both ages is high lateral to the ostium, where EBD uptake is low; the discrepancy is particularly obvious in the mature age group but, once identified, can be discerned in the immature group too. Our previous studies of rhodamine-albumin uptake (Ewins et al., 2002, Bailey et al., 2015) give a pattern that more closely resembles the lesion frequency maps; uptake is high lateral to the branch mouth (See figure 2.11). Hence there appears to be an issue with the uptake of EBA.

EBD is known to potentially have an indirect pharmacological effect on the VSMCs of the arterial media, inhibiting endothelium-dependent relaxation (Forster and Weinberg, 1997b). Therefore, it has the potential to alter the mature pattern of transport, since that is NO-dependent to some extent as discussed above. In previous studies, assessing long-term (3 h) aortic uptake of EBA along the centerline of the renal artery

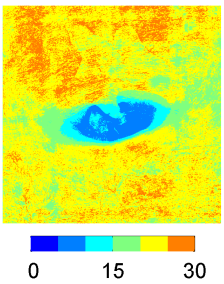


Figure 2.12: Levels of autofluorescence surrounding branch ostia. The image, which shows an average of maximum intensity projections for 6 branches, has the same size and orientation as the maps in figure 2.5. Intensity in arbitrary units.

branch, transport was greater downstream than upstream of the ostium in immature rabbits, as expected, but this pattern was not abolished with increasing age; however, when EBA circulated for shorter times (15-20 minutes), the downstream pattern was abolished or reversed in rabbits approaching maturity, mirroring the observations with rhodamine albumin (Murphy, 1998, Murphy and Lever, 2002). This suggests that long-term exposure to EBA may influence transport but short-term exposure does not. Exposure to EBA was restricted to 10 minutes in the present study to minimise modification of transport patterns by the EBA itself.

A second possibility is that since EBD binds preferentially to elastin and collagen once the tracer enters the wall, its observed distribution may depend not only on transport rates but also on the amount and location of these proteins. For instance, an area of low EBD fluorescence could arise either due to low endothelial permeability or due to low elastin and collagen content in the intima directly below. Elastin and collagen are the primary source of tissue autofluorescence, so we investigated this possibility by scanning 6 intercostal branch ostia from a mature rabbit not administered EBA, using similar methods to those described above except that excitation and emission wavelengths were reduced to 458 nm and 490-530 nm, respectively; there is negligible autofluorescence at the longer wavelengths used to image EBA. The average map (Fig 2.12) revealed regions lateral to the branch mouth with lower autofluorescence intensity than upstream and downstream regions, consistent with the view that the discrepancy between EBA and rhodamine-albumin uptake is caused by lower concentrations of elastin and/or collagen in these areas.

2.5 Conclusions

In conclusion, our data do show that the pattern of endothelial permeability hotspots around intercostal branch ostia changes with age and in a way that is consistent with the patterns of lesions. Hotspots were not the major route for EBA uptake and were not dominantly explained by patterns of mitosis. They may play a more significant role in the transport of larger molecules such as LDL. It is plausible that hotspots represent an arbitrary subdivision of a continuum of local permeabilities reflecting intercellular junctions of different width.

Chapter 3

Patterns of Endothelial Permeability to Large Macromolecules

3.1 Introduction

Patterns of permeability to macromolecules around arterial branch points and their relation to the development of atherosclerosis have been extensively discussed in previous sections. The literature concerning hotspots has been reviewed in the Introduction to the previous chapter. The present chapter considers the effect of macromolecule size on patterns of permeability hotspots. The EBA tracer used in chapter 2 has a Stokes-Einstein radius of around 3.5 nm, and should therefore pass through the endothelial small pores, identified as a combination of gaps in the tight junctions between neighbouring ECs and the overlying glycocalyx; these small pores - at least in capillaries - give permeability-surface area products for solutes of different size that would be predicted by restricted diffusion through a cylindrical pore having a radius of approximately 5 nm (see Komarova and Malik, 2010, Levick, 2003 p.157 for a review of this topic).

Clearly, solutes of radius much greater than 5 nm should not pass through such pores, but entry into the arterial wall of considerably larger species (e.g. LDL, diameter approximately 23nm) does take place. These solutes are thought to penetrate through a different system - the large pores; the physical nature of the large pores is a matter of debate. One possibility is that such large solutes enter the wall predominantly through endothelial permeability hotspots representing temporarily widened inter-endothelial cell clefts (Weinbaum et al., 1985). Another possibility is that they enter across the cells through a mechanism depending on vesicles (Tarbell, 2003). There is further debate as to whether transendothelial vesicular transport of solutes occurs via shuttling of vesicles backwards and forwards across cells, by the temporary fusion of pairs of vesicles permitting transfer of their contents, or by the fusion of vesicles to form patent tubes from the lumen to the subendothelial space (Tuma and Hubbard, 2003, Frank et al., 2003, Rippe et al., 2002, Schnitzer, 1992, Predescu and Palade, 1993). Since LDL is strongly associated with the development of a therosclerosis, this is an important issue.

In the study reported in this chapter, the EBA experiments were repeated but using a tracer with a molecular mass similar to that of LDL (Hydrodynamic radius=27.2 nm, Nordmeier, 1993). The distribution

of hotspots of its uptake around intercostal branch ostia was examined in immature and mature rabbits to determine whether the patterns were similar to those found for EBA, which would suggest a dominant role for leaky junctions in the uptake of larger macromolecules, or whether they were dissimilar, which would suggest a different route.

3.2 Methods

All animal procedures, tissue preparation and microscopy were performed by a postdoc within the Weinberg Group, Dr. Lindsey Clarke. The subsequent image processing algorithm applied to quantify the images was developed and implemented by the author and some of the manual image processing steps relied upon in this algorithm were performed by an undergraduate intern, Miss Soléne Cadiou under the author's supervision.

3.2.1 Animals

Eight male New Zealand White (NZW) rabbits of the HSDIF strain were obtained from Harlan (Bicester, Oxford, UK) for this study. They were housed under a 12 h light/dark cycle and were fed a standard laboratory diet *ad libitum*. Ages and weights of each individual are listed in table 3.1. All animal procedures complied with the Animals (Scientific Procedures) Act 1986 and were approved by the local ethical review panel of Imperial College London.

Immature

Identifier	Age [days]	weight [kg]
DPSL	62	1.65
EGXY	61	1.55
ERLA	62	2.08
ERKI	62	1.97
mean	62	1.81
s.e.m	0.3	0.13

Mature

Identifier	Age [days]	weight [kg]
ACPF	446	4.44
AIFE	533	4.80
AXPS	425	3.97
ALUE	533	5.54
mean	484	4.68
s.e.m	29	0.33

Table 3.1: Summary of ages and weights of rabbits used in dextran endothelial permeability study

3.2.2 *In vivo* Protocol

2 MDa dextran, labelled with tetramethylrhodamine (TMR) and made aldehyde-fixable by the addition of covalently bound lysine (TMR-dextran, Molecular Probes®), was used to obtain fluorescence images showing the uptake patterns of large macromolecules through the endothelium. TMR-dextran was administered via

the marginal ear vein at a dose of 4 mg kg^{-1} in saline and allowed to circulate for 30 minutes. 28 minutes after the tracer injection, heparin was administered (2000 U, *i.v.*) and, after a further 2 minutes, the rabbit was killed with an overdose of pentobarbitone (Euthatal, Rhône Mérieux, 160 mg kg^{-1}, *i.v.*).

The aorta was exposed by performing a midline thoracotomy and laparotomy followed by reflecting the thoracic and abdominal organs. A cannula was inserted into the aorta in the retrograde direction at the level of the diaphragm and secured. The vessel was then flushed with 50 ml physiological saline from a pressure reservoir suspended 1 m above the animal. The maximum time delay between death and the beginning of this flushing step was 5 minutes. Finally, the aorta was perfused with 15 % formaldehyde from a second reservoir suspended 1 metre above the animal for 30 minutes to fix the vessel *in situ* , as had been done for all previous studies in this group. After approximately 1-2 minutes of fixation, the aortic arch was clamped to reduce the volume of fixative required. The thoracic aortas from the arch to the diaphragm were excised and stored in 15 % formaldehyde until required.

3.2.3 Immunofluorescence Staining for CD31 and Preparation of Tissue for Confocal Microscopy

In order to visualise the EC boundaries, antibody staining was done to fluorescently label the cell-surface protein, CD31. Thoracic aortas were opened along the ventral midline and placed in a blocking solution containing 2 % BSA for 45 minutes. The tissue was then placed in a primary monoclonal mouse anti-human CD31 antibody solution (1:15, Dako, Clone JC70A) for 1 h, washed and then placed in a secondary polyclonal Alexa Fluor®633-conjugated goat anti-mouse IgG solution (1:50, Thermo Scientific) for 1 h. All blocking and staining solutions were made up in PBS and all steps were performed at room temperature. The vessels were then mounted *en face* in VECTASHIELD®HardSet™mounting medium (Vector Laboratories).

3.2.4 Confocal Microscopy

Tissue autofluorescence (AF) and TMR and Alexa Fluor®633 fluorescence from the *en face* mounted vessels was recorded at specific locations around intercostal ostia as z-stack image volumes using an inverted laser scanning confocal microscope (Leica SP5) with a computer-controlled galvanometer stage and a 20× magnification, 0.7 NA glycerol-immersion lens; excitation and emission wavelengths (ex/em [nm]) for AF, TMR and Alexa Fluor®633 were (458/565-610), (561/565-610) and (633/645-699) respectively. Each stack was taken at 200 % electronic zoom, minimising the effects of any spatial biases in the optical train, at a pixel resolution of 512×512, representing a 775×775 µm square. Image stack locations were manually selected to lie upstream, downstream, left and right of the ostia as depicted in figure 3.1.

3.2.5 Image Analysis

Image processing was done using a combination of FIJI (Schindelin et al., 2012) and MATLAB®, using the java-based interface, MIJ (Sage et al., 2012). A secondary goal throughout the developement of the image

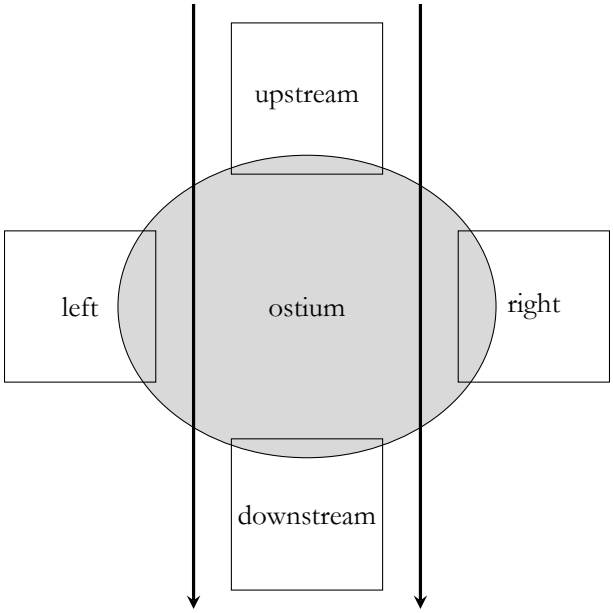


Figure 3.1: Schematic showing approximate locations of regions of interest around intercostal ostia. Arrows illustrate direction of predominant axial flow.

processing algorithm was to develop methods with as high a degree of automation as possible to minimise observer bias and to produce methods with applicability to more than one dataset.

3.2.5.1 Automated Ostial Masking

The purpose of this process was to produce a mask from the AF channel of each image stack which could be applied to the other two channels to remove branch mouth pixels from further analysis. A histogram-based strategy to automatically threshold AF images was developed and the algorithm is demonstrated on a typical AF image from the mature dataset (See figure 3.2). A maximum intensity projection (MIP) of each stack was first performed to create a single image with (x,y) locations occurring within the ostium showing up as background signal (Fig 3.2a). To remove high frequency noise arising from the high photon multiplier gain (940.0 V), a mean filter with a radius of 3 pixels was applied (Fig 3.2b). A histogram was generated and numerically differentiated twice to find the intensity value at the first local minimum (Fig 3.2c). The lower and upper peaks in Fig 3.2c correspond to the dark pixels in the ostium and the brighter pixels of the tissue respectively. The MIP was then thresholded at this intensity value, resulting in a preliminary binary mask (Fig 3.2d). Initial testing on a subset of MIPs showed that some had patches within the ostium with fluorescence signal above the threshold, usually due to some foreign material in the branch. These would appear in the mask as small, false positive regions in the ostium and were removed by several iterations of erosion operations until there was only one positive region remaining in the mask, representing the tissue. An equal number of dilation operations was performed to undo the erosion of the true positive region. As repetition of erosion and dilation causes triangulation of curves, a maximum number of 25 iterations was

allowed.

10 MIPs were randomly selected from each age group and manually checked at high magnification to confirm that the boundary of the automatically generated mask was accurate to within 5 pixels of where an unbiased observer would have manually traced the boundary (Fig 3.3a). Those that failed this test were mostly images where the tissue was either damaged or folded (Fig 3.3b).To remove these from the dataset, all masks were manually checked at low magnification and for any instances where automatically generated masks failed to accurately depict the ostium, a manual check of all three image channels was done to determine if a mask could be traced manually. If a manual mask was not possible due to there being folds or tears in the tissue, the image was omitted from further analysis.

3.2.5.2 Quantification of Dextran Uptake

After initial manual thresholding of a subset of MIPs generated from the dextran channel images, it was noted that the hotspot pixels occurred at intensities much greater than the mean intensity in each image. Thus it appeared that hotspot pixels could be separated from background fluorescence pixels (i.e.: noise) by approximating the distribution of the noise pixels as a normal distribution and setting an intensity threshold a given number of standard deviations above the mean noise intensity. The number of standard deviations was chosen so that only one pixel of noise per image would be expected to exceed the threshold on average. For a 512×512 pixel image containing 262144 pixels, the number of standard deviations needed above the mean to only expect one pixel of noise is 4.4757.

To confirm this, images of the autofluorescence at TMR excitation and emission wavelengths of a naive rabbit aorta were obtained, following the same protocol described in section 3.2.2 but omitting the administration of the dextran tracer. The same locations described in figure 3.1 were imaged around 8 intercostal branches using the scan settings for TMR fluorescence as described in section 3.2.4. Figure 3.4 shows a histogram of the average image generated from these 32 images. Although formal statistical tests for normality (eg: Jarque-Bera test) show that the distribution of intensities is not normal, it is visually evident from the histogram that *approximating* the background fluorescence as a normal distribution is appropriate if we only use it to determine a threshold above which background fluorescence can be ignored.

The semi-automated algorithm to calculate this threshold is demonstrated on the dextran MIP (Fig 3.5a), corresponding to the AF image used previously in figure 3.2. A histogram of the background noise was created after removing ostial pixels using the masks generated as described in section 3.2.5.1 (Fig 3.5b). Then, hotspots were removed by setting a manual threshold (Fig 3.5c) such that the histogram of the remaining pixels better approximated a normal distribution. The mean (μ) and standard deviation (σ) of the resulting histogram were calculated; removing the hotspots with this manual thresholding step removed the influence of the bright hotspot pixels on the mean and standard deviation of the background. Finally, a new threshold,

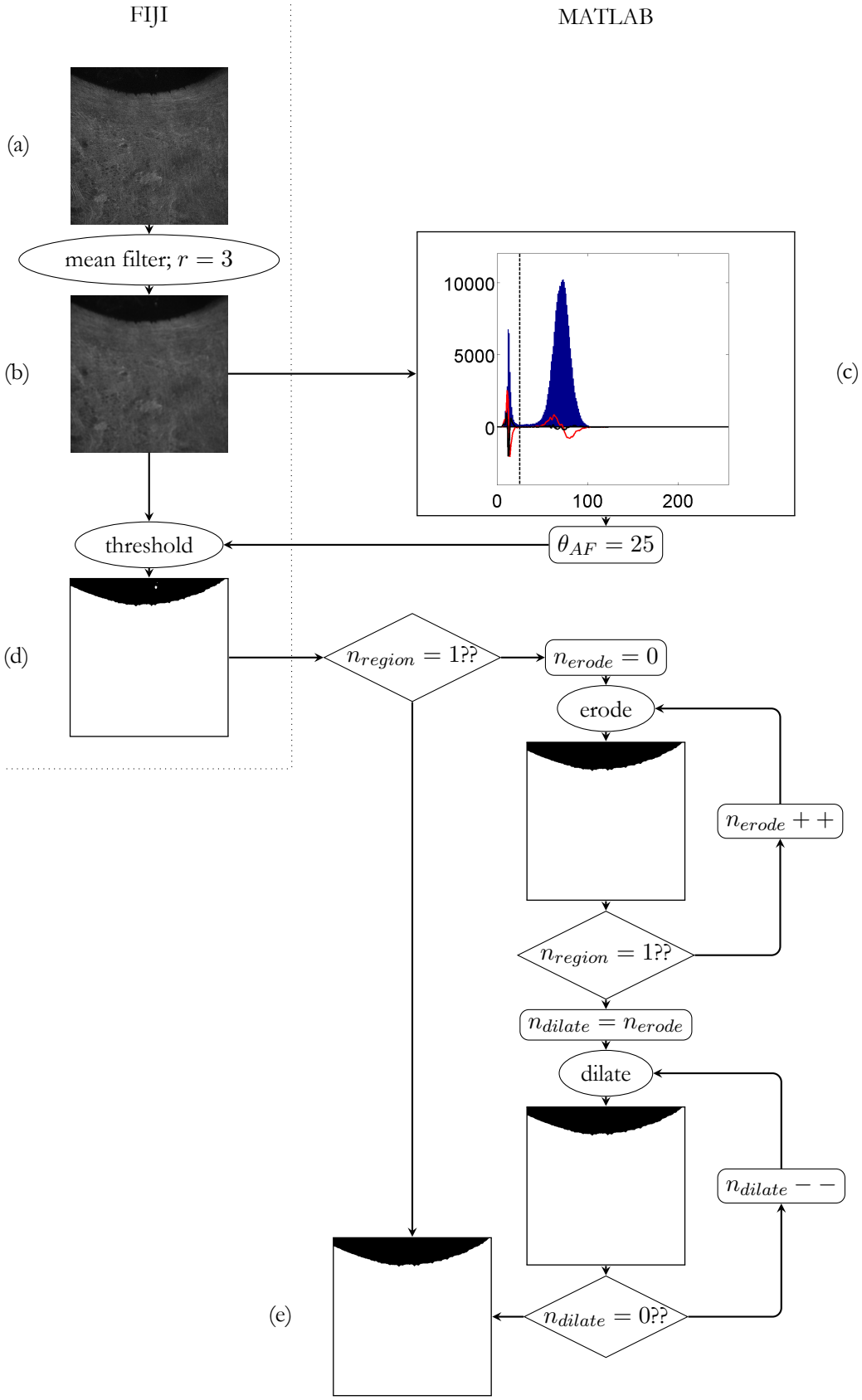
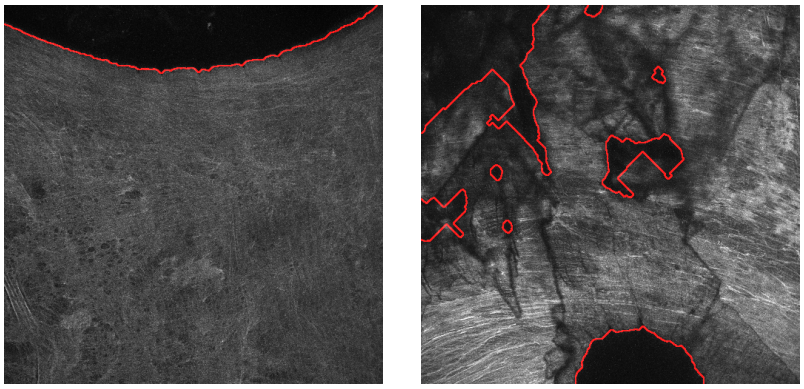


Figure 3.2: Overview of automated ostium masking algorithm, demonstrated on a typical image: (a) MIP of the AF channel of a typical z-stack (b) MIP after smoothing with an averaging filter with radius=3 pixels (c) Histogram of the MIP with 1st (red) and 2nd (black) derivatives of the histogram envelope superimposed. The threshold is depicted by the dotted line (d) Preliminary binary mask (e) Binary mask after erosion/dilation iterations



(a) (b)

Figure 3.3: Examples of automatically generated ostium masks from AF MIPs. In each example, the mask boundary (red) is overlaid over the original MIP (grey). (a) Ostium boundary correctly identified (b) Damaged tissue

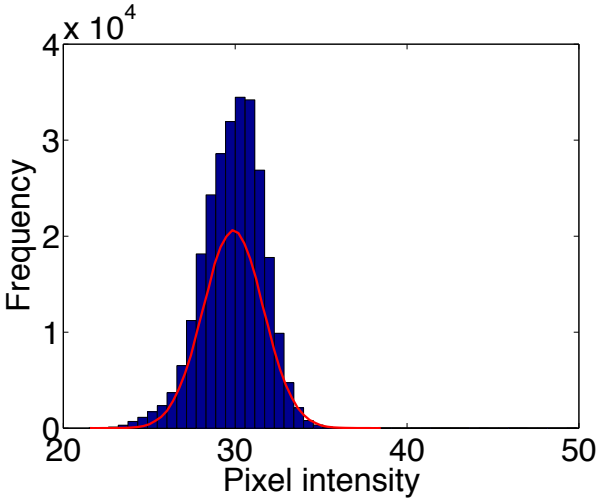


Figure 3.4: Histogram of average background fluorescence around naive rabbit ostia taken from 8 branches. A Normal distribution curve with $\mu = 29.9$ and $\sigma = 1.75$ is superimposed in red.

θ_{dex} ,was calculated from these two values (equation 3.1). The function of the manual threshold was only to reduce the influence of the hotspot pixels on the calculated threshold. Applying this calculated threshold to the masked MIP(3.5b), hotspots were effectively separated from the background tissue fluorescence (Fig 3.5d).

$$\theta_{dex} = \mu + 4.4754\sigma \tag{3.1}$$

Dextran hotspots were counted in each image and summarised as total numbers of hotspots occurring upstream, downstream, left and right of the ostium in each age group. Statistical outliers were removed by Chauvenet's criterion.

To check that θ_{dex} reliably separated hotspots from the background fluorescence, mean background fluorescence was calculated for each image by calculating the mean pixel intensity after removal of all hotspot pixels. Similar to the hotspot counts, these data were summarised as mean background fluorescence intensity upstream, downstream, left and right of the ostium in each age group

Comparisons between the locations within each age group were done with unpaired t-tests in the following paris: upstream (U) vs downstream (D); left (L) vs right (R); and medial (Me) vs lateral (La).

3.2.5.3 Segmentation of Endothelial Cell Boundaries

The overall aim for this section of the study was to determine if the dextran hotspots occurred at boundaries of ECs. Attempts to segment EC boundaries from MIPs of the z-stacks of tissue stained with the fluorescently-labelled anti-PECAM antibody were made using a combination of FIJI plugins. As with the dextran MIP processing, CD31 MIPs were first masked to remove branch mouth pixels using the same masks as before. Intensity of the staining was spatially heterogeneous so images were artificially flattened: An effective flatfield correction image was generated by passing an averaging filter over each MIP and normalising by the maximum pixel intensity. The original MIP was then flattened by dividing by the effective flatfield correction image. Individual images also had differing levels of background fluorescence. To overcome this, an unbiased edge detection kernel was used to separate brightly stained EC boundaries from the background:

$$\begin{bmatrix} 1 & 1 & 1 & 1 & 1 \\ 1 & 1 & 1 & 1 & 1 \\ 1 & 1 & -24 & 1 & 1 \\ 1 & 1 & 1 & 1 & 1 \\ 1 & 1 & 1 & 1 & 1 \end{bmatrix}$$

The resulting image was thresholded, creating a binary image. The FIJI *skeletonize* plugin was run on the binary image to obtain the cell boundaries. Due to the variation in background and foreground intensity

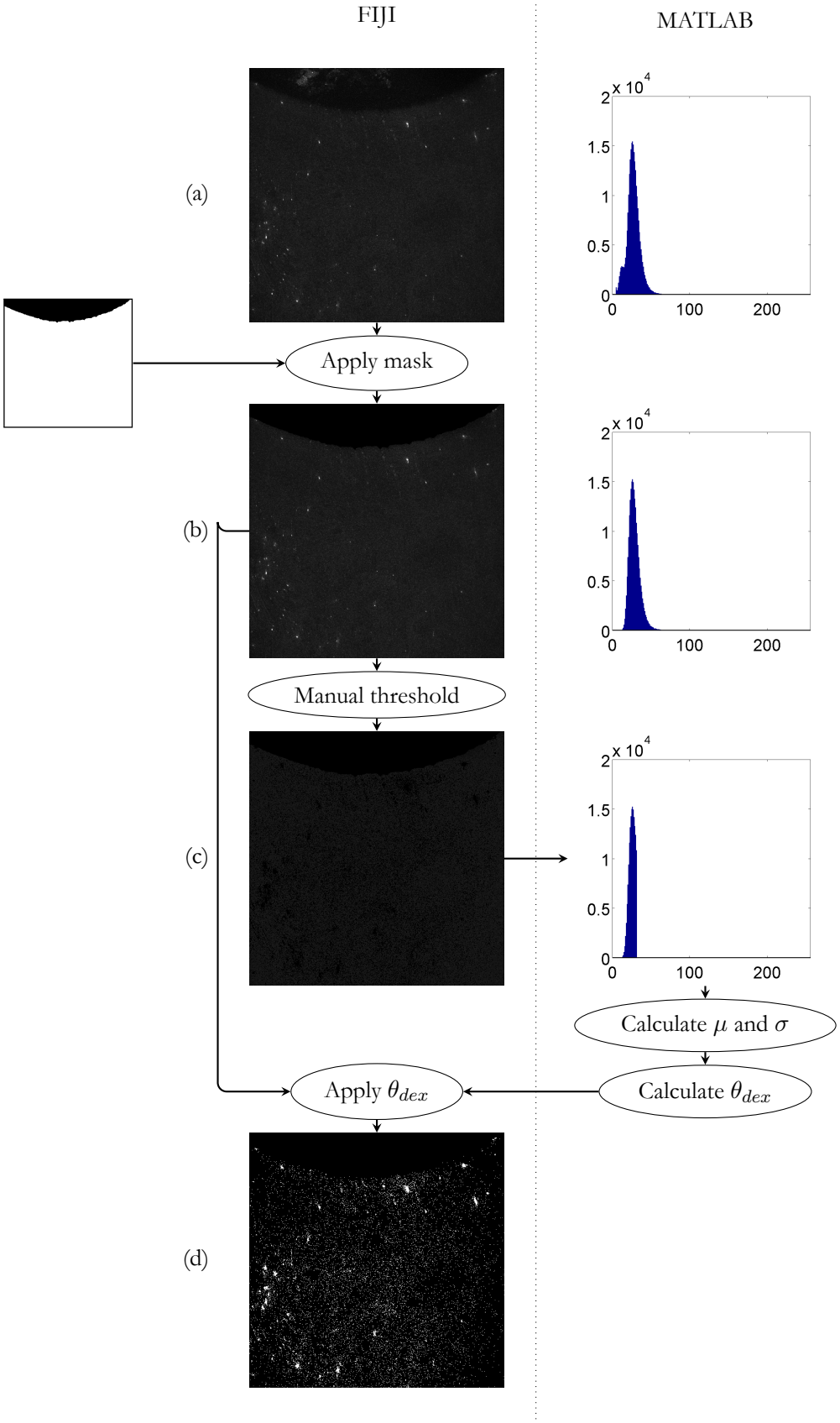


Figure 3.5: Overview of automated intensity-based hotspot thresholding algorithm: (a)MIP of the dextran channel of a typical z-stack (b) MIP after masking using mask generated in figure 3.2 (c) Result of manual thresholding to approximately segment hotspots (d) Apply θ_{dex} to segment dextran hotspots

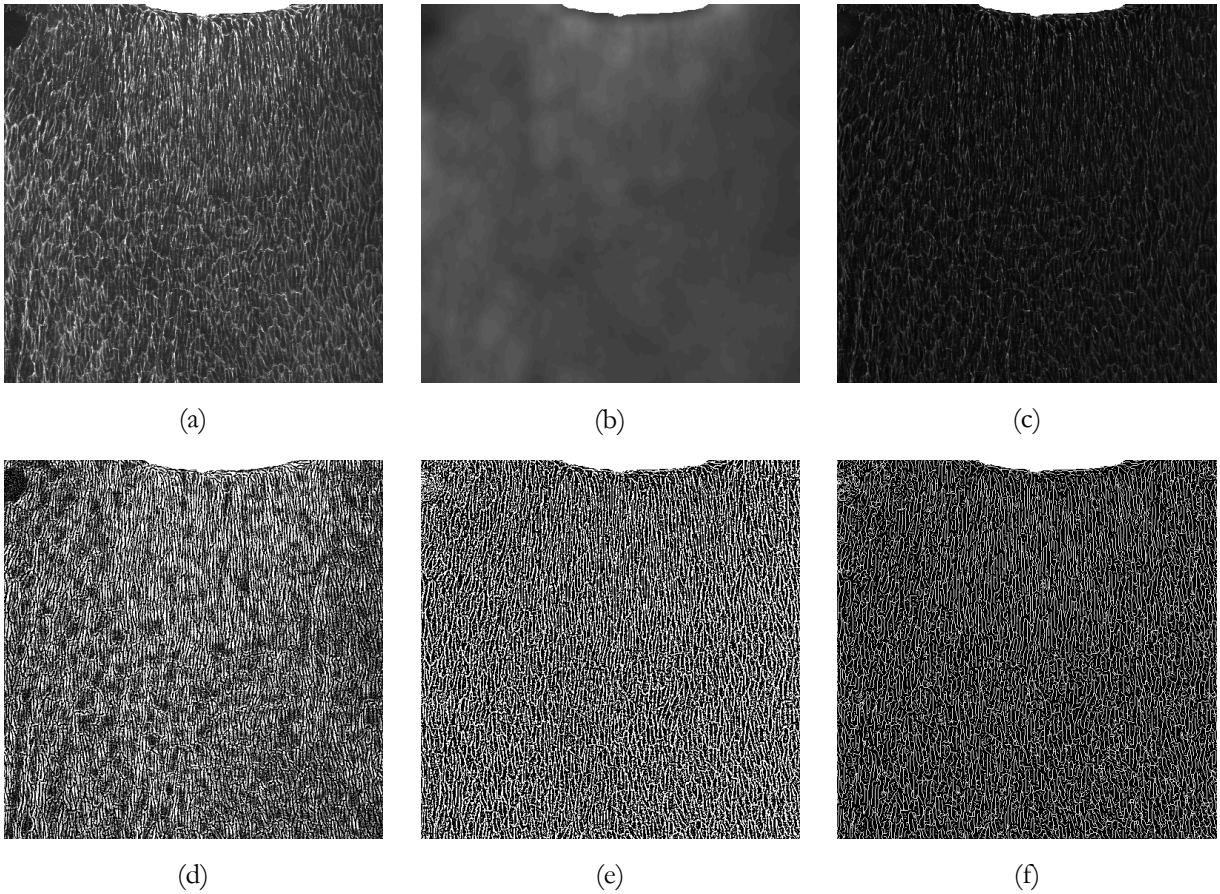


Figure 3.6: Overview of automated skeletonising algorithm: (a) Original CD31 MIP. (b) effective flatfield correction generated from (a). (c) Flattened MIP obtained by dividing (a) by (b) and subtracting the mean intensity of (b). (d) Result of convolution of (c) with unbiased edge finding kernel. (e) Manually selected threshold applied to (d). (f) Skeletonize plugin applied to (e). All images are 512×512 pixels, representing a 775×775 μm square.

between images, no common set of segmentation parameters (averaging filter radius, edge detection kernel size, threshold) was found to work for all images. The example shown below shows the results for a single image and can be taken to be a proof-of concept for this boundary segmentation algorithm (Fig 3.6). Further development is needed to remove observer bias, introduced through selection of the segmentation parameters described above, and this part of the study was not pursued further.

3.3 Results

3.3.1 Outliers

Statistical outliers were identified by applying Chauvenet's criterion iteratively on the extreme data points at each location: upstream (U), downstream (D), left (L) and right (R) of the ostium. Data from the images corresponding to these outliers were excluded in further analysis. The spread of the remaining data is shown in the boxplots in figure 3.7 with the outliers in each location shown in red.

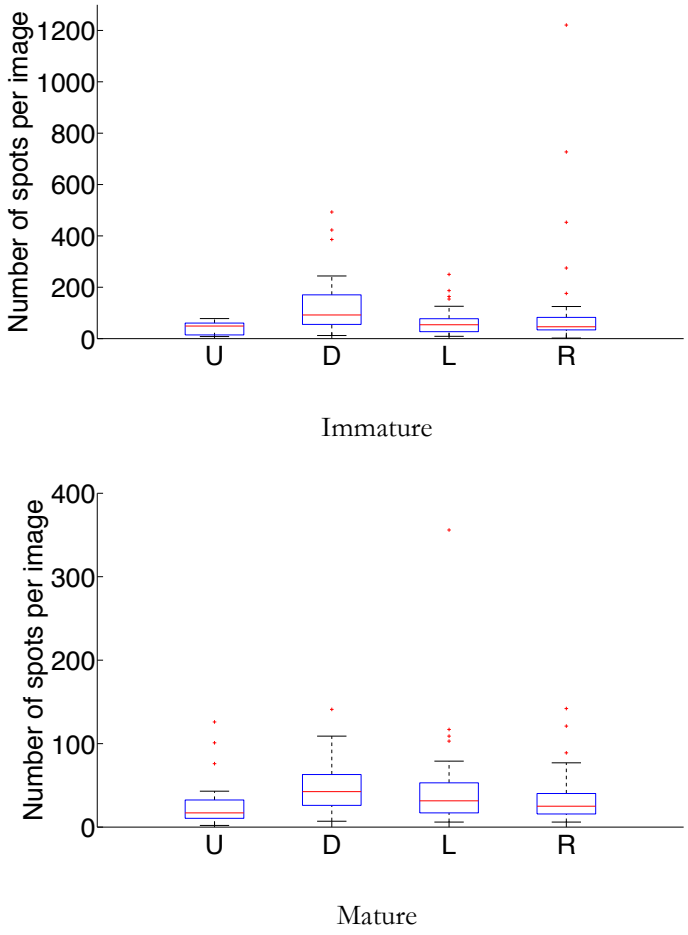


Figure 3.7: Boxplots showing number of spots identified in dextran uptake images. Outliers were identified by sequentially testing Chauvenet's criterion on maximum and minimum data points and are shown in red.

In both age groups, the majority of outliers occurred at the lateral (La) locations (ie: left and right) as opposed to the medial (Me) locations (ie: upstream and downstream). It was also noted that outliers tended to occur in consecutive branches in individual animals: All the immature outliers at the right location correspond to images from two animals. Similarly, two out of the three mature outliers at the right location originated from the same animal.

A similar pattern was observed in the downstream outliers: All three immature downstream outliers originated from one animal. Upstream outliers did not follow the same pattern with all originating from separate animals. However it should be noted that there were no upstream outliers in the immature; only in the mature group.

3.3.2 Qualitative comparisons

Qualitative comparisons of the distribution of spots around the ostia were made by summing the binary hotspot images produced by the segmentation algorithm. The immature pattern appears similar to previously reported patterns of Rh-BSA uptake in immature rabbits, with most spots occuring in a downstream triangle

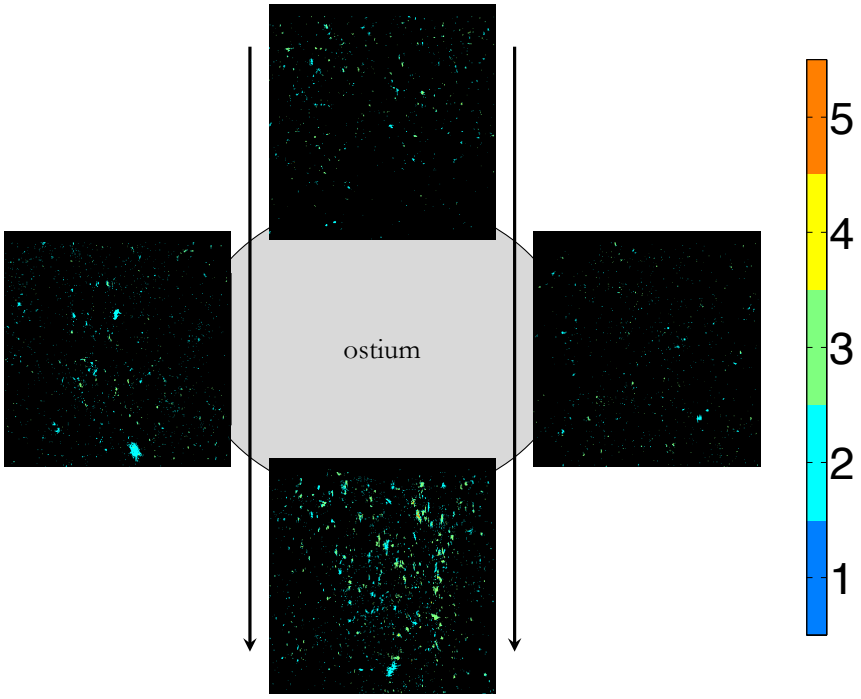


Figure 3.8: Summation of maps of hotspot occurence around intercostal ostia in immature rabbits. Arrows illustrate direction of predominant axial flow. (n=23-28)

(Fig 3.8). This pattern also corresponds to the EBA hotspot patterns in immature animals (Fig 2.5). There was no easily discernible pattern in the mature group (Fig 3.9) that corresponded to the pattern observed in the mature group of the EBA study (Fig2.6). The total number of spots in immature animals was significantly higher than in mature animals ($p = 5.1321 \times 10^{-9}$).

3.3.3 Statistical comparisons of hotspot occurrence between locations

At each location, hotspots counts were summarised as the mean number of spots counted in each image, shown in figure 3.10. Additionally, the left and right locations were grouped as lateral (La) locations and the upstream and downstream locations were grouped as medial (Me) locations. In the immature data, significantly more hotspots occurred downstream than upstream ($p = 8.4825 \times 10^{-5}$). Additionally, there were significantly more spots in the medial locations compared to the lateral locations ($p = 0.0156$). No other statistically significant differences of interest were found. In the mature data, there were also significantly more hotspots downstream of the ostia compared to upstream ($p = 3.4804 \times 10^{-6}$).

3.3.4 Validation of hotspot segmentation

As an internal validation of our segmentation algorithm, the mean background intensity of the images after hotspot removal was assessed at each location. As shown in figure 3.11, mean background intensity was constant at all the locations: unpaired t-tests on the data showed no significant differences between any pairs of locations. This supports the view that few hotspots had below-threshold intensities (otherwise, for

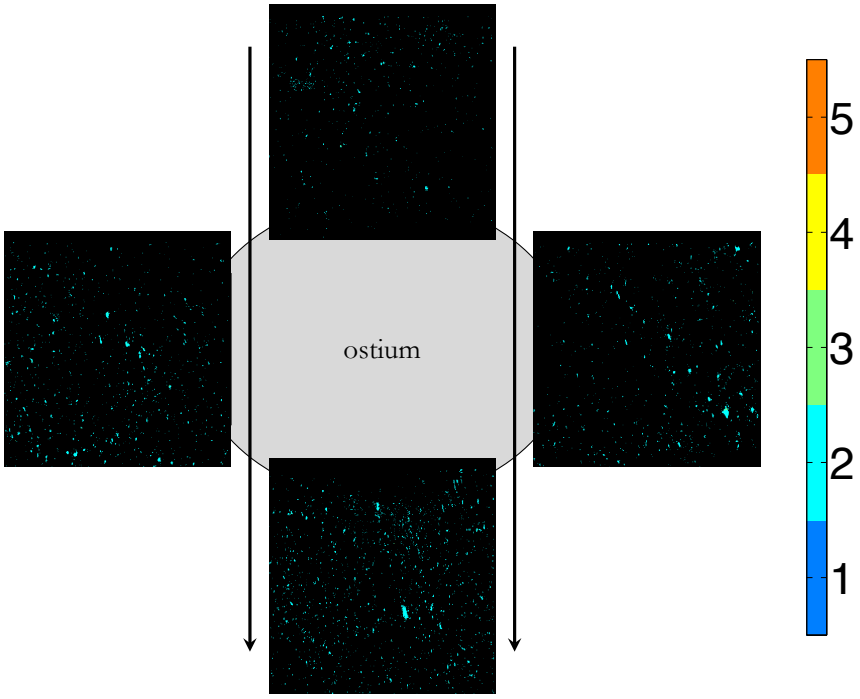


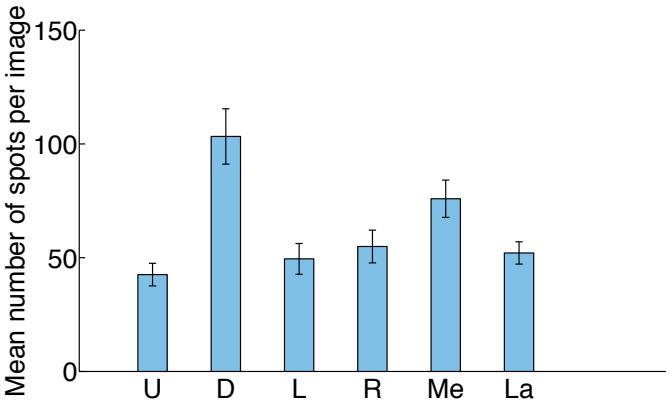
Figure 3.9: Summation of maps of hotspot occurence around intercostal ostia in mature rabbits. Arrows illustrate direction of predominant axial flow. (n=29-35)

example, we would have expected greater apparent background signal downstream of immature ostia than in other regions).

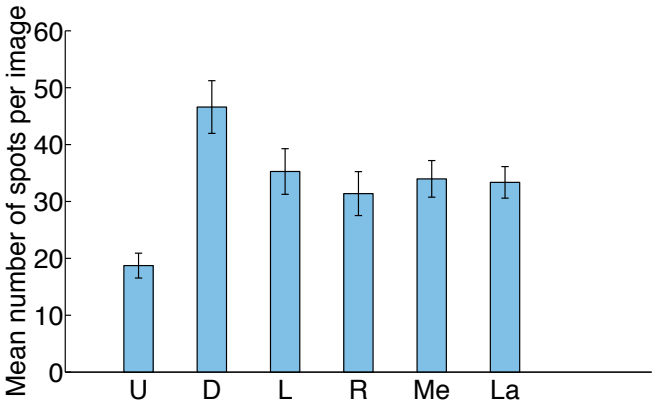
3.4 Discussion

The exclusion of the outliers can be justified by our previous observations of axially aligned streaks of elevated permeability that occur on either side of intercostal branch pairs in the rabbit aorta at all ages; they appear to be artefacts caused by mechanical damage caused when the aorta depressurises but still contains tracer (Baldwin et al., 1982, Bailey et al., 2015). As reported above, lateral outliers tended to occur in consecutive branches. This pattern is consistent with the presence of streaks of elevated permeability affecting consecutive branches.

The immature dextran hotspot pattern corresponds visually to the EBD hotspot and lesion prevalence patterns previously shown in chapter 2 and with previously published Rh-BSA patterns (Bailey et al., 2015). Upstream vs downstream and lateral vs medial comparisons of mean numbers of dextran spots confirm these qualitative observations: the same relation between these locations was observed in the mass transfer coefficient of Rh-BSA in similar regions of interest (See figure 3 in Bailey et al., 2015). This similarity in permeability patterns for two tracers which differ in mass almost 30-fold is further evidence for there being a continuum of junctional widths, an idea previously discussed in chapter 2. The fact that the mature pattern of dextran hotspots was different from the pattern of EBD hotspots and Rh-BSA uptake, where the highest levels were found lateral to branches, requires further investigation. Contrary to the interpretation of the data

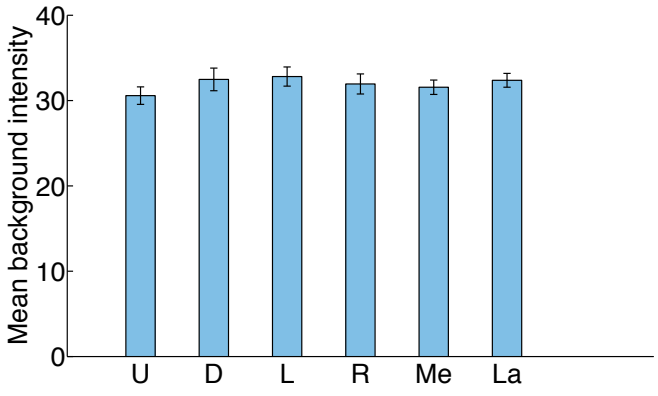


Immature

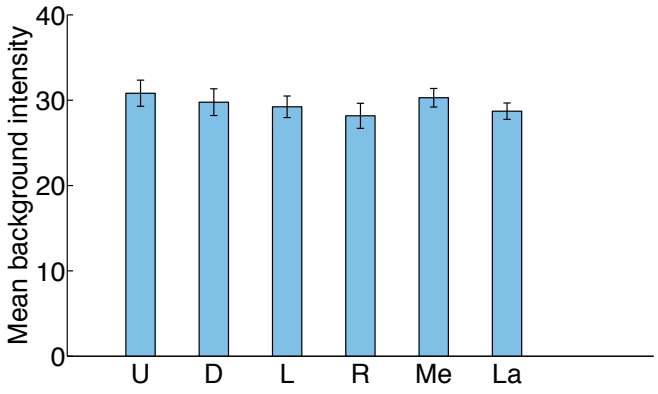


Mature

Figure 3.10: Average number of dextran hotspots occurring around rabbit intercostal ostia. Data shown as mean±SEM. Abbreviations: Upstream (U), Downstream (D), Left (L), Right (R), Medial (Me), Lateral (La). (Immature: $n = 23 - 28$; Mature: $n = 29 - 35$)



Immature



Mature

Figure 3.11: Average background fluorescence intensity of dextran uptake images. In both age groups, no statistically significant differences between the background intensities at each location were observed.

from immature rabbits, it does appear to indicate different transport routes.

3.4.1 Further work

The absence of the previously reported mature pattern for Rh-BSA complicates the interpretation of these results as they stand. From figures 3.8 and 3.9, it appears that this could have been caused by the data being influenced by artefacts on the edge of the ostium. Similar artefacts were avoided in our previous work by excluding the tissue directly adjacent to the branch mouth, which is known to be prone to artefacts introduced by manipulation of the tissue during staining and mounting. (An example of this is shown in figure 3.5). In previous work on Rh-BSA uptake, regions of interest were defined a set distance away from the edge of the branch mouth with positions defined relative to the geometric centre of the ostium. For the EBD study in chapter 2, grid squares containing any branch mouth pixel were excluded, thereby removing branch mouth artefacts. In the case of this study, without a full tile scan covering the entire ostium, this was not possible as the geometric centre of the ostium was not imaged. A crude alternative would be to crop all images so that only half of each image (the half furthest from the branch mouth) was used in the analysis. Visually, from figures 3.8 and 3.9, this would not be expected to change the trends observed in the immature images but could result in a mature spot pattern resembling the mature Rh-BSA uptake patterns (Bailey et al., 2015)

As mentioned in section 3.2.5.3, a clearer picture of the location of dextran hotspots in relation to the location of EC boundaries would provide a better understanding of the transport pathways for large molecules. The algorithm demonstrated above is highly sensitive to changes in its parameters so the current results are prone to observer bias as they are currently set manually. Methods to choose parameters based on the images need development to remove user input.

Additional insight may be obtained by analysing the areas and intensities of the spots, as was done in the EBD study. From figures 3.8 and 3.9, immature spots appear to be larger than in the mature images. Combined with there being more spots in immature images, this suggests total dextran uptake is greater in immature animals.

Chapter 4

Development of Methods to Determine Medial Mass Transport Properties

4.1 Introduction

In collaboration with Dr Andrew Comerford, a combined numerical/experimental workflow was developed to measure arterial wall transport properties. Development of all experimental and imaging/image processing techniques was carried out by the author and all the implementation for the numerical simulations was done by Dr Comerford. Techniques trialled are detailed below, accompanied with explanations justifying the choice of final methods. How these techniques were combined and applied to investigate the relationship between transmural pressure or VSMC tone on medial permeability is described in chapters 5 and 6 respectively.

4.2 Established Experimental Methods

4.2.1 Preparation of Fluorescent Protein Tracer

Rhodamine-labelled bovine serum albumin (Rh-BSA) was used as the fluorescent tracer in all experiments. It was prepared in-house by conjugating Sulforhodamine B acid chloride to BSA following a protocol adapted from Nairn (1964). All tracer preparation reagents were purchased from Sigma unless otherwise specified. 1.5 g sulphorhodamine B acid chloride was dissolved in 100 ml acetone, added drop-wise to 15 g BSA dissolved in 750 ml 0.5 M bicarbonate buffer (440 mM $NaHCO_3$, 57 mM Na_2CO_3, pH9.0) and stirred for 60 minutes in an ice bath.

Unbound rhodamine was separated from Rh-BSA by gel filtration: 180 ml samples were filtered through a column of Sephadex® G-25 beads (column diameter: 4 cm, column length: 70 cm; elution buffer: 0.25 × Ringer's solution: 2.25 g l^{-1} NaCl, 50 mg l^{-1} KCl, 50 mg l^{-1} $CaCl_2$, 25 mg l^{-1} $NaHCO_3$; flow rate: 20 ml min^{-1}). The fraction containing rhodamine-albumin was identified by measuring absorbance at 280 nm, 565 nm and 575 nm corresponding to the absorbance peaks of unbound albumin, unbound rhodamine and rhodamine-albumin. This fraction was dialysed against $\frac{1}{10}\times$ Tyrode's Salt Solution (TSS, 8.00 g l^{-1} NaCl, 0.20 g l^{-1} KCl, 0.20 g l^{-1} $CaCl_2$, 0.10 g l^{-1} $MgCl_2$, 0.05 g l^{-1} NaH_2PO_4, 1.00 g l^{-1} $NaHCO_3$, pH6.5) at 4 °C for 24 h. The

final protein solution in $\frac{1}{10}\times$ TSS was snap frozen in liquid nitrogen and lyophilised for storage at $-20\,°C$. Absorbance at 575 nm, total volume of eluent and total weight of solutes were recorded to calculate protein and fluorophore concentration.

For use in *ex vivo* experiments, a tracer solution was made up using $\frac{9}{10}\times$ TSS to contain $10\,mg\,ml^{-1}$ lyophilised Rh-BSA, accounting for the weight of salts remaining from the dialysis, and $30\,mg\,ml^{-1}$ unlabelled BSA in $1\times$ TSS. Any remaining free dye was removed by adding 0.5 % charcoal and stirring at room temperature for 1 h. The solids were removed by centrifugation (4 °C, 3000 ×g, 2×15 minutes) followed by filtration through a syringe filter with 0.2 µm pores.

4.2.2 Preparation of Glycerol-based Anti-fade Mounting Medium

A glycerol-based anti-fade mounting medium was prepared following a recipe adapted from Mukwevho et al. (2008). 36 g glycerol, 14.4 gram Mowiol® 4-88 and 93.6 ml distilled water were mixed at room temperature for 6 h. 14.4 ml 1 M Tris buffer (pH8.5) was then added and the whole mixture heated to 50 °C while stirring. Undissolved solids were removed by centrifugation at 5000 ×g for 15 minutes and the supernatant was decanted and allowed to cool to room temperature. 2 % N-propyl-galate was added and mixed until it dissolved. The mounting medium was stored in the dark at −20 °C.

4.2.3 Preparation of Poly(dimethylsiloxane)-lined petri dishes

Poly(dimethylsiloxane) (PDMS)-lined petri dishes were prepared as experiment chambers for *ex vivo* experiments. Sylgard 184 elastomer kit was purchased from VWR and used according to the manufacturer's instructions. Monomer base and initiator solution were mixed in a 9:1 ratio by weight. Once mixed, bubbles were removed by centrifugation at 500 ×g for 5 minutes and dissolved gasses were removed by placing in a vacuum chamber at −12 mmHg for 30 minutes. Any remaining bubbles were burst with a jet of air delivered from a bulb pipette. PDMS was cured at 55-65 °C for 2-4 h.

4.3 Development of *ex vivo* L_p and P Measurement Methods

Methods for *ex vivo* measurement of hydraulic conductance, L_p , have been published in the literature (Tedgui and Lever, 1984, Shou et al., 2006). Similar methods have been used to determine solute permeability, P , *in vitro* on EC monolayers (Cancel et al., 2007, Cancel and Tarbell, 2010, 2011). The general principal in all of these previous works involves measuring the flux that crosses a known area of vessel wall or EC monolayer. In the case of L_p measurements, the hydraulic flux is measured by tracking a bubble in a graduated capillary while the solute flux required to measure P is usually measured fluorimetrically. The *ex vivo* methods developed here aimed to make simultaneous L_p and P measurements on whole isolated arterial segments.

The short-term goal during the initial development of the *ex vivo* methods was to choose a suitable bifurcation in an animal model that would allow accurate measurement of L_p and P. (A bifurcation was

chosen so that effects of flow variation on P could be examined in future studies.) The carotid and aortic bifurcations in mice, rats and rabbits were identified as possible bifurcations for study. To narrow down this initial selection of possible arteries for study, an uncertainty analysis was first carried out using Microsoft Excel, taking estimates of typical dimensions of possible arteries and the associated uncertainties expected in each measurement (Section 4.3.1). Further, practicality of manually manipulating the remaining candidate bifurcations to *repeatedly* obtain useable *ex vivo* preparations was evaluated by dissection and corrosion casting of cadavers (Section 4.3.2). The external pressurisation/measurement circuit was designed and validated to ensure that *ex vivo* preparations were exposed to a known, constant transmural pressure (Section 4.3.3). Once the choice of vessel had been made, initial development of surgical procedures was carried out on cadavers before finally transferring the techniques into anaesthetised animals (Sections 4.3.4, 4.3.5). Final refinements of the technique were made over the course of the first set of experiments (Section 4.3.6). The final procedure carried out under terminal anaesthesia is presented in section 4.3.7.

4.3.1 Uncertainty Analysis

Expected values were estimated for all the measured dimensions (aortic and iliac diameters and lengths; cannula inner diameter) and their associated measurement tolerances. Vessel dimension estimates were based on measurements of vascular casts and in cadavers. Assuming a whole wall L_p in the order of magnitude of published values ($\sim 1 \times 10^{-7}\,\mathrm{cm\,s^{-1}\,mmHg^{-1}}$), hydraulic flux and bubble displacement over a 300 s time interval were back-calculated to determine the largest potential source of error in the final L_p value. Calculations were done for pressures within the physiological pressure range (80-120 mmHg) and the results at 100 mmHg are shown in table 4.1.

In all three animals, the largest source of error is the vessel surface area. Therefore the measurement tolerances in the vessel dimensions are the limiting factor. Larger errors are introduced as the surface area of the vessel decreases. Based on these observations, the larger the animal, the more accurate the final L_p value. Similar calculations were done for the carotid bifurcations of rabbits, rats and mice and they showed similar results: the rat carotid corresponded to the mouse aorta and the rabbit carotid corresponded to the rat aorta. The measurement error estimated for the mouse carotid bifurcation surface area was large ($\sim$20 %). If, after further feasibility checks, the mouse carotid were to be selected, the measurement methods for the bifurcation dimensions would have to be made more accurate to reduce this error.

	Measurement	Error	Percentage error	Unit
RABBIT				
Cannula inner diameter	1	0.01	1.00	mm
Displacement	12	0.05	0.42	cm
Measurement interval	300	0	0	s
Hydraulic Flux	3.14×10^{-4}		2.42	$cm^3\ s^{-1}$
Aortic diameter	3	0.01	0.33	mm
Aortic length	2	0.01	0.50	cm
Left iliac diameter	2	0.01	0.50	mm
Left iliac length	1	0.01	1.00	cm
Right iliac diameter	2	0.01	0.50	mm
Right iliac length	1	0.01	1.00	cm
Surface area	3.14		3.83	cm^2
RAT				
Cannula inner diameter	1	0.01	1.00	mm
Displacement	6	0.05	0.83	cm
Measurement interval	300	0	0	s
Hydraulic Flux	1.57×10^{-4}		2.84	$cm^3\ s^{-1}$
Aortic diameter	2	0.01	0.50	mm
Aortic length	1.5	0.01	0.67	cm
Left iliac diameter	1	0.01	1.00	mm
Left iliac length	1	0.01	1.00	cm
Right iliac diameter	1	0.01	1.00	mm
Right iliac length	1	0.01	1.00	cm
Surface area	1.57		5.17	cm^2
MOUSE				
Cannula inner diameter	1	0.01	1.00	mm
Displacement	1.44	0.05	3.47	cm
Measurement interval	300	0	0	s
Hydraulic Flux	3.77×10^{-5}		5.47	$cm^3\ s^{-1}$
Aortic diameter	1	0.01	1.00	mm
Aortic length	0.7	0.01	1.43	cm
Left iliac diameter	0.5	0.01	2.00	mm
Left iliac length	0.5	0.01	2.00	cm
Right iliac diameter	0.5	0.01	2.00	mm
Right iliac length	0.5	0.01	2.00	cm
Surface area	0.38		10.43	cm^2

Table 4.1: Preliminary uncertainty analysis for L_p Measurements

4.3.2 Feasibility Studies in Various Arteries

The uncertainty analysis left several candidate locations: rabbit and rat aortic and carotid bifurcations and mouse aortic bifurcations. To narrow down this selection, these locations were studied further using vascular casts, cadavers and veterinary anatomy texts.

Rat and mouse arterial vascular trees were corrosion cast using a protocol adapted from one already established in the group to cast rabbits. Male C57/BL6 mice were sacrificed by intraperitoneal (*i.p.*) injection of an overdose of sodium pentobarbitone (40 mg, Pentoject, Animalcare Ltd., York, UK). Male Sprague-Dawley (SD) rats were sacrificed using a slowly rising concentration of CO_2, following guidelines of the Laboratory Animal Science Association (LASA) and the Royal Society for the Prevention of Cruelty to Animals (RSPCA) (LASA and RSPCA, 2011): Rats were placed in a 36.4 l chamber into which CO_2 was introduced at an initial flow rate of $2\,\mathrm{l\,min^{-1}}$ for 2 min. The flow rate was then increased to $7\,\mathrm{l\,min^{-1}}$ for 6 min before allowing for a 10 min dwell time.

Immediately after death was confirmed by loss of corneal reflex and lack of chest movement and heart beat, a thoracotomy was performed and the left ventricle cannulated with a polyethylene cannula connected to a 5 ml (mouse) or 20 ml (rat) syringe filled with heparinised saline (10 USP units $\mathrm{ml^{-1}}$ heparin, $9\,\mathrm{g\,l^{-1}}$ NaCl). The right atrium was cut and the whole vascular network was perfused with the heparin-saline.

A low-viscosity acrylic resin (Batson's #17 Anatomical Corrosion Kit, Polysciences, Warrington, PA, USA) was prepared by mixing 20 ml monomer base, 1 ml promoter, 8 ml catalyst and 0.5 g white pigment. Bubbles were removed from the mixture by briefly placing in a vacuum chamber at -12 mmHg for 2 min. The mixture was placed into a 20 ml syringe and was connected to the left ventricular cannula as shown in figure 4.1. All tubing lengths were kept as short as possible to minimise elasticity in the system stemming from the compressibility of the air. The length of the tube connecting the 3-way tap at A to the manometer was 45 cm and was chosen to be the shortest possible length while still being long enough to avoid excess resin running into the manometer. Transmural pressure was measured using a digital differential manometer with one port left open to the atmosphere, the other connected to the left ventricle; the skin of the abdominal cavity opened. Care was taken to prevent the introduction of air bubbles into any part of the perfusion system; any that did enter were diverted towards the manometer by orienting tap A (Fig 4.1) so that its manometer connection was vertical.

The resin was pumped into the arterial tree at a flow rate of $5\,\mathrm{ml\,min^{-1}}$ until the intravascular pressure was measured to be 80 mmHg above atmospheric pressure. This pressure was maintained by pumping additional resin at $5\,\mathrm{ml\,min^{-1}}$ when the pressure dropped to 75 mmHg until the resin set, $\sim$35 min after initial mixing. This was evidenced by rapid heating of the mixture remaining in the syringe due to the exothermic nature of the polymerisation. Tap B was closed before disconnecting the pressurisation circuit from the carcass and

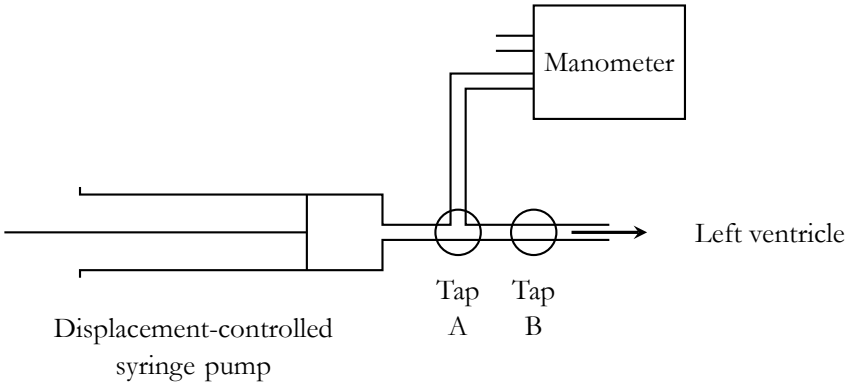


Figure 4.1: Setup of the apparatus used for making arterial casts of mice and rats.

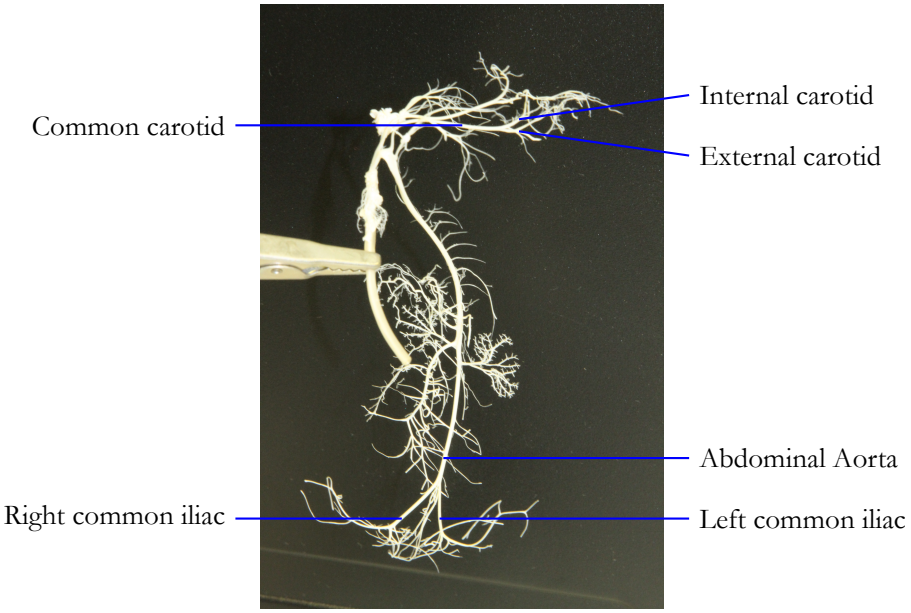


Figure 4.2: Photograph of rat arterial cast showing locations of vessel dimensions measured

the resin was allowed 24 h to fully polymerise at room temperature.

Carcasses were submerged in 25 % KOH at room temperature for 5 days before rinsing with warm water to remove any remaining tissue. A final wash in a detergent solution containing ∼5 % Decon90 (Decon Laboratories Ltd., Sussex, England) was done to remove any remaining fats.

Inner diameters of vessels were measured at locations detailed in 4.2. Additionally, variability in the branch locations was noted. Rabbit casts previously made by other group members were also studied. However, due to the large number of accessory arteries branching from the aorta and common iliacs in rabbit casts, and the variability in location of the caudal and inferior mesenteric arteries, rabbits were not included in further feasibility considerations.

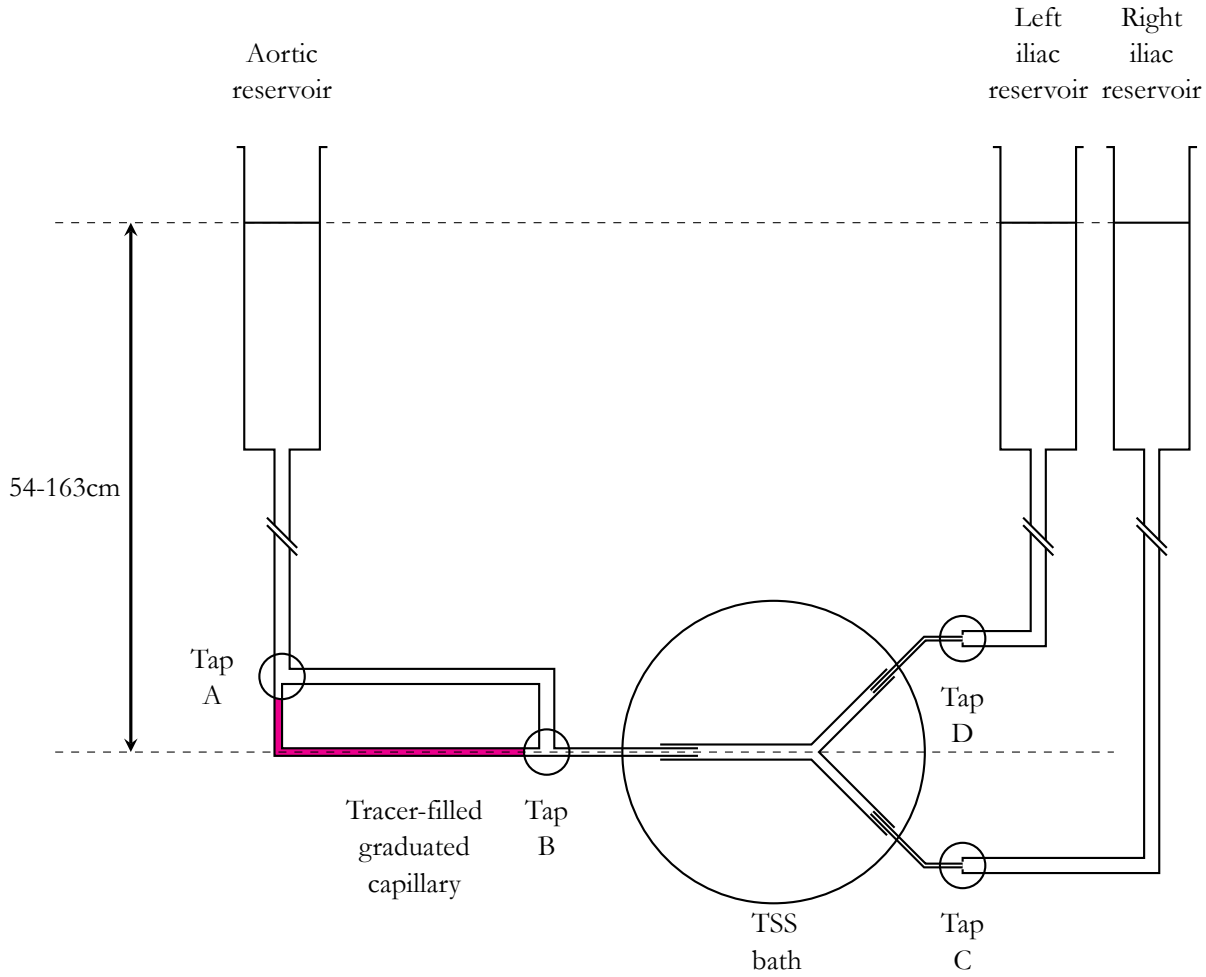


Figure 4.3: Setup of the apparatus used to apply a constant transmural pressure to vessels during isolation and during L_p and P measurements on isolated *ex vivo* vessel preparations. TSS bath: PDMS-lined 40 mm petri dish containing 5 ml TSS.

4.3.3 The External Pressurisation/Measurement Circuit

4.3.3.1 Development

A circuit to maintain a constant transmural pressure from suspended saline reservoirs was developed, following previously published work (Tedgui and Lever, 1984, Shou et al., 2006, Cancel and Tarbell, 2010). The circuit was intended both for use during isolation of arterial bifurcations and to make L_p and P measurements, thus a switching circuit was added to previous designs to introduce a tracer solution into the lumen after isolation. Following the results of the uncertainty analysis (Section 4.3.1), the cannula dimensions were chosen such that the tolerance in measuring bubble displacement was much lower than the error expected in calculating the vessel surface area. The final design was reached iteratively during the development of surgical procedures on cadavers (Section 4.3.4) and is shown in figure 4.3.

4.3.3.2 Validation

The setup was validated to check that the intended transmural pressure was indeed applied across the vessel wall and that the small transmural water flux was not causing a large pressure drop over the resistance of the cannulae. Two male Sprague-Dawley rats were sacrificed by asphyxiation in a rising concentration of CO_2 as described in section 4.3.2. The aortic bifurcation was isolated using a system of cannulae similar to that shown in figure 4.3, replacing the left iliac cannula with a pressure transducer and omitting the tracer from the tracer-filled capillary: the aortic cannula was inserted in the anterograde direction into the abdominal aorta just distal to the left renal artery and secured just distal to the ilio-lumbar arteries. A second cannula was inserted in a retrograde direction into the right femoral artery and secured at the distal end of the right common iliac artery. Saline supplemented with ∼1 % Evan's Blue Dye (EBD, Sigma) was perfused between the two cannulae to highlight any side-branches surrounding the aortic bifurcation and all visible side branches were ligated. A pressure transducer (Millar) was inserted through the left common iliac and advanced to the aortic bifurcation and secured with a ligature placed half way along the left common iliac. Finally, the right iliac cannula was closed using a three-way tap (Tap C in figure 4.3) and the aortic cannula was connected to the saline reservoir.

An initial approximate calculation of the external circuit's hydraulic resistance was done by assuming Poiseuille flow though the 50 cm long aortic capillary/cannula of 0.46 mm internal diameter and ignoring the resistance of the 2.5 mm internal diameter tubing connecting the reservoirs to the cannulae. Given a vessel area of 1 cm^2 and an expected L_p in the order of 1×10^{-7} $cm\,s^{-1}\,mmHg^{-1}$ at 100 mmHg, the flow rate was estimated at 1×10^{-5} $ml\,s^{-1}$. This would give a pressure drop of 4.31×10^{-1} mmHg. Thus the external resistance was expected to be negligible.

These estimates were confirmed by measuring the transmural pressure at reservoir heights at 10 cm increments from 0-180 cm (See figure 4.4).

4.3.3.3 Application: L_p and P measurement

L_p is defined as the volume flow rate of a given fluid across a unit area of material per unit pressure drop (Levick, 1987). Using the external pressurisation/measurement circuit, the transmural volume flow rate (Q) was measured for a known pressure drop (Δp): both iliac cannulae were closed to ensure the volume entering the vessel through the aortic cannula equalled the flux exiting the vessel over the entire vessel surface. The displacement of the distal meniscus (s_m) of a bubble placed in the graduated capillary was then measured at set time intervals (Δt) and the volume flow rate was calculated from the known inner diameter of the capillary ($\varnothing_i$) according to equation 4.1. The vessel surface area (A) was calculated from measurements of the vessel segment lengths, diameters and bifurcation angles depicted in figure 4.5 using equation 4.2. Finally, L_p was calculated according to equation 4.3.

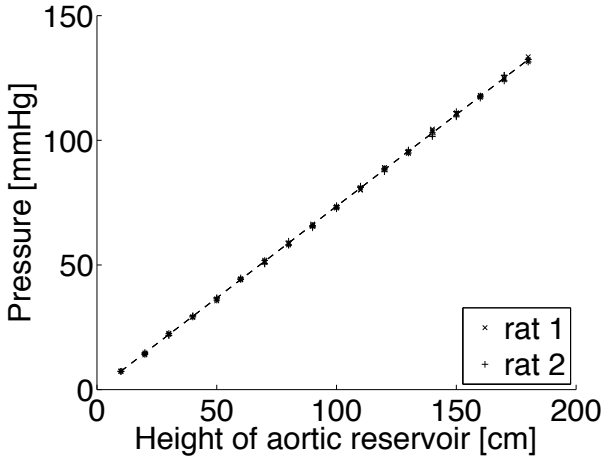


Figure 4.4: Validation of pressurisation/measurement circuit. The dashed line represents the theoretical relation between pressure and height of reservoir, given the density of Hg = 13.6 g cm^{-3}

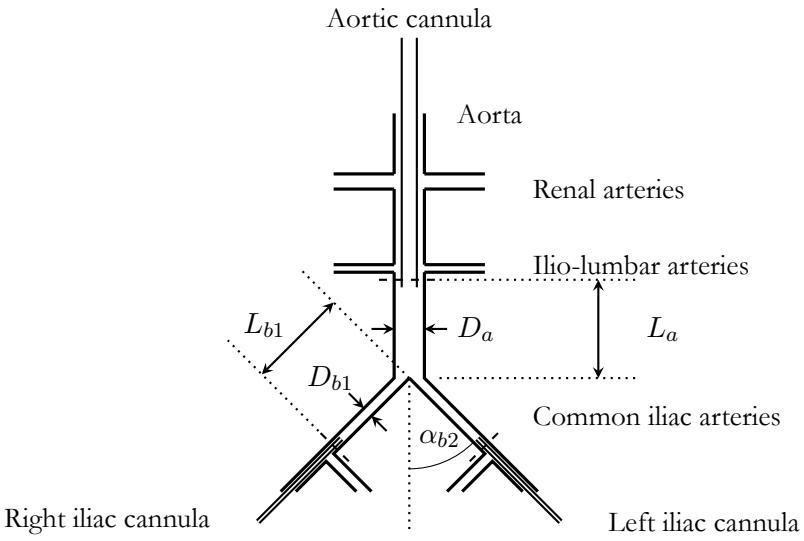


Figure 4.5: Diagram showing the vessel segment lengths, diameters and bifurcation angles measured in order to calculate vessel surface area and hence L_p and P . Ligatures securing cannulae are depicted with dashed lines.

$$Q = s_m \frac{\pi \varnothing_i^2}{4} \frac{1}{\Delta t} \tag{4.1}$$

$$A = \sum_{i=a,b1,b2} \pi D_i L_i - \sum_{i=b1,b2} \frac{\pi D_a^2}{8 \sin \alpha_i} \tag{4.2}$$

$$L_p = \frac{Q}{\Delta p A} \tag{4.3}$$

P was calculated by measuring abluminal tracer concentration fluorimetrically: 1 ml samples were measured using a fluorimeter (Jenway 6283; excitation 570 nm; emission 600 nm) at set time intervals and fluorescence readings were converted to abluminal tracer concentrations (C_{abl}) using a calibration curve, generated from dilutions of the luminal tracer solution. Hence the effects of any differences in luminal tracer concentration (C_{lum}) due to batch variation in tracer preparation would be annulled. Samples were returned to the abluminal bath after each reading so that the volume of the bath (V_{abl}) remained constant, ignoring any increase in V_{abl} due to Q. P was then calculated according to equation 4.4.

$$P = \frac{(\Delta C_{alb}/\Delta t) \times V_{abl}}{C_{lum} A} \tag{4.4}$$

4.3.4 Development of Procedures using Cadavers

Procedures were trialled, developed and practiced in both mice and rat cadavers. Fresh cadavers were used throughout to replicate tissue mechanical properties to simulate surgery as closely as possible as that was the ultimate goal of these procedures: to isolate vessels from animals under surgical anaesthesia to avoid damage to the vessels that would occur due to de-pressurisation following death.

4.3.4.1 Preparation of Cadavers for Mock Surgery

Ten attempts to isolate the mouse carotid bifurcation were made using a similar procedure, substituting the right and left femoral arteries for the internal and external carotid arteries and the aorta for the common carotid artery. Ten rats were used for both carotid bifurcation and aortic bifurcation isolation attempts to assess which bifurcation and animal would be most suitable for further development. In each trial run, L_p measurements were made to determine if the isolation attempt had been successful.

Male C57/BL6 mice (~25 g) were given 200 U heparin dissolved in 200 µl saline by *i.p.* injection. After 10 minutes, they were sacrificed by *i.p.* injection of an overdose of sodium pentobarbitone (40 mg). Male Sprague-Dawley rats (~200-300 g) were given 1000 U heparin dissolved in 1 ml saline by *i.v.* injection via the tail vein. After 2 minutes, they were sacrificed by *i.v.* injection of an overdose of sodium pentobarbitone (200-300 mg). Heparinisation was only necessary for these early trial runs in cadavers to prevent clotting of

the blood in the target bifurcations before our isolation attempts. Heparinisation was omitted in subsequent experiments in anaesthetised animals.

After confirmation of death, the left ventricle was cannulated with a polyethylene cannula as described in section 4.3.2 but without cutting the right atrium. To replicate the arterial pressure in an anaesthetised animal, the cannula was then connected to a saline reservoir containing saline supplemented with ∼1 % Evan's Blue Dye (EBD, Sigma) suspended ∼1.1 m above the carcass to give an arterial pressure of ∼80 mmHg. Any subsequent leaks would therefore be immediately apparent. These steps were omitted in subsequent experiments on anaesthetised animals as the beating heart would provide the positive transmural pressure and any leaks would be visible due to bleeding.

4.3.4.2 Early Carotid and Aortic Bifurcation Isolation Attempts in Mice and Rats

Ten attempts to isolate the abdominal bifurcation from mice while maintaining a constant transmural pressure were made using the procedure described below. A further ten attempts to isolate the mouse carotid bifurcation were made using a similar procedure, substituting the right and left femoral arteries for the internal and external carotid arteries and the aorta for the common carotid artery. Similarly, ten rats were used for both carotid bifurcation and aortic bifurcation isolation attempts to assess which bifurcation and animal would be most suitable for further development. In each trial run, L_p measurements were made to determine if the isolation attempt had been successful.

1. Cannulate left external femoral artery
    (a) Make a longitudinal incision through the skin of the upper thigh and expose the femoral artery by further blunt dissection, removing any excess fat
    (b) Detach the external femoral artery and vein from the underlying muscle and tie a ligature around both femoral artery and vein ∼1 mm distal to the intended cannulation point, leaving the ends of the ligature long
    (c) Tie a temporary ligature ∼2 mm proximal to the intended cannulation point
    (d) Place a loose ligature between the two previous ligatures, make a small incision into the femoral artery and insert the cannula, securing it with this central ligature
    (e) Tie the loose ends of the distal ligature around the cannula
    (f) Untie the proximal ligature and advance the cannula into the external iliac artery
    (g) Open the 3-way tap connected to the cannula to flush any blood from the tip of the cannula
2. Cannulate right external femoral artery by repeating the steps above
3. Access the abdominal aorta

(a) Perform a laparotomy by making a single midline incision through skin and abdominal muscle from a point ∼2 mm caudal to the sternum to the to a point ∼2 mm rostral to the scrotum

(b) Ligate the inferior mesenteric artery as close to the aorta as possible

(c) Cut the rectum, cauterising any bleeding that occurs

(d) Reflect the entire gut

(e) Ligate the ilio-lumbar arteries and caudal artery

(f) Open the 3-way taps on both femoral artery cannulae

4. Cannulate abdominal aorta

(a) Prepare three ligatures at the aortic cannulation point as in step 1:

i. Tight ligature just distal to the most distal renal branch

ii. Temporarily ligate ∼2 mm distal to the first ligature

iii. Loose ligature between the two previous ligatures

(b) Make a small incision between the two secured ligatures, insert the aortic cannula and secure with the central ligature

(c) Untie the temporary ligature and advance the cannula to a point just proximal to the most proximal ilio-lumbar branch and secure with another ligature as close to the end of the cannula as possible, leaving the ends of the ligature long

(d) Open the 3-way tap connected to the aortic cannula

(e) Perfuse the isolated bifurcation with a suspension of <106 μm diameter glass beads to occlude any small accessory arteries branching from isolated bifurcation and to block any leakage through the vasa vasorum internae

5. Secure cannula ligatures and attach isolated bifurcation to stereotactic tripod

(a) Advance both femoral cannulae to the iliac bifurcations and secure them with a ligature just proximal to the respective bifurcations, leaving the ends of the ligature long

(b) Bend the arms of the stereotactic tripod to match the lengths of the arterial segments *in situ* and tie the long ends of the cannula-securing ligatures to the arms

6. Remove bifurcation from abdomen

(a) Remove any adventitial fat from the isolated bifurcation and loosen it from all surrounding tissue by blunt dissection

(b) Cut ligated side-branches (e.g.: caudal, ilio-lumbar, femoral) just distal to their ligatures

(c) Remove bifurcation from the abdomen and place directly in a TSS bath

The sequence of placing three ligatures at each femoral cannulation site was designed to prevent de-pressurisation of the lumen proximal to the point of insertion (Step 1). Conversely, the sequence of ligatures was reversed for the aortic cannula to prevent collapse of the aortic bifurction, distal the the insertion point (Step 4a). Total time taken for the entire procedure was approximately 3 hours.

4.3.4.3 Final Choice of Bifurcation

Trial #	Weight [g]	Carotid L_p [cm s^{-1} mmHg]	Aortic L_p [cm s^{-1} mmHg]
Mouse			
1	23	-	-
2	22	-	-
3	24	-	5.35×10^{-8}
4	25	-	-
5	23	-	-
6	23	-	-
7	25	-	-
8	21	-	-
9	25	-	-
10	24	-	-
mean	23.5	-	5.35×10^{-8}
s.e.m	0.41	-	-
Rat			
1	289	-	4.75×10^{-8}
2	230	-	-
3	305	-	4.97×10^{-8}
4	201	-	-
5	250	-	-
6	321	-	4.87×10^{-8}
7	274	1.27×10^{-7}	-
8	283	-	-
9	295	-	9.29×10^{-8}
10	221	-	-
mean	266.9	1.27×10^{-7}	5.97×10^{-8}
s.e.m	13.2	-	1.10×10^{-8}

Table 4.2: Results of trial L_p measurements in mouse and rat carotid and aortic bifurcations. Dashes indicate missing data due to leakage of isolated bifurcation.

The L_p measurements made in the trial runs on mouse and rat carotid and aortic bifurcations are given in table 4.2. Failure of a trial run was determined when leakage of the coloured EBD-supplemented TSS was visible. Success rates on the carotid bifurcations were much lower than those on the aortic bifurcations as the vessels are of a much smaller diameter and they are only loosely tethered to surrounding soft tissue, making

cannulation more difficult. In fact, no cannulation attempts in the mouse carotid bifurcation worked. The success rate in rat aortic bifurcations was higher than in the mouse due to the larger vessel inner diameters. Therefore the rat aortic bifurcation was selected as the vessel and animal with which to continue development of procedures.

4.3.5 Transfer of Procedures to Anaesthetised Animals

For the early work under anaesthesia, inhalational methods were chosen due to the relatively long duration of the proposed procedure: the shortest successful trial run on rat abdominal aortas had taken ∼2.5 h from first insertion of cannula to final removal of the isolated bifurcation.

Rats were placed in an induction chamber into which isoflurane (IsoFlo®, Abbott Animal Health, IL, USA) was introduced at a concentration of 3-5 % in medical oxygen (BOC, UK) at a flow rate of 2-3 l$\,$min^{-1} until the animal lost its righting reflex. The animal was then placed in a supine position on a temperature-controlled heat mat at 37 °C and fitted with a face mask, delivering isoflurane at a concentration of 1.5-2.5 % in medical oxygen at a flow rate of 0.7-1 l$\,$min^{-1} until surgical anaesthesia was achieved, evidenced by the lack of pedal withdrawal reflex. Depth of anaesthesia was constantly assessed during surgery by observing breathing rate and periodically checked by testing for the absence of the pedal withdrawal reflex. Isoflurane concentration was adjusted to control depth of anaesthesia.

The procedure used in trial runs, as described in section 4.3.4, was used essentially unchanged for the first three attempts in anaesthetised animals. The only changes were in the preparation of the TSS: all TSS was placed in an incubator at 37 °C with a gas composition of 5 % CO_2, 95 % air for 24 h preceding the experiment. In subsequent attempts, refinements were made to the procedure with the aim of increasing the success rate and reducing the total time of the surgery.

4.3.6 Refinement of Surgical Techniques

In initial experiments, L_p and P were measured at 40 mmHg, 80 mmHg, 100 mmHg and 120 mmHg in that sequence in order to identify weaknesses in the preparations that might occur with increasing pressure.

4.3.6.1 Glass beads vs Cauterisation vs Ligation

During attempts to measure L_p and P at pressures >100 mmHg, leakages were very common, often occurring after successful measurements of L_p and P at lower pressures. Closer inspection of the vessel preparations showed that these leaks invariably occurred from accessory arteries or from the vasa vasorum internae, rather than tears or holes in the artery walls: Leaks from accessory arteries appeared as a jet of tracer at the end of short arterial segments; leaks from vasa vasorum internae appeared as more diffuse plumes of Rh-BSA in the abluminal bath adjacent to darkly-coloured vessel-like structures on the outer surface of the arteries. A simple adjustment of using glass beads of a mixture of diameters was tested: glass beads (⌀<106 µm, Sigma) were

suspended in TSS and placed in the aortic cannula before its insertion into the aorta. Convection through any leaks would then carry the particles into the leakage site, sealing the hole. This was trialled in two experiments however the problem was not solved. Therefore we sought an alternative to glass beads as a method for preventing convection through the vasa vasorum internae and accessory arteries.

Trials using a unipolar electrocautery scalpel were conducted with varying results: In four experiments in which leaks occurred at 100 mmHg, the larger accessory arteries were successfully sealed but repetition of the L_p measurements at 80 mmHg after cauterisation were always higher than the values obtained before the leaks. It is likely that the area of effect of the cautery was larger than the actual cauterised area, especially since it was a unipolar device; due to the geometry of the electrodes, control of the area exposed to a current density sufficient to cause coagulation is not as precise with unipolar devices compared to bipolar devices. Leakage through vasa vasorum could not be cauterised without causing electrical burn damage to the vessel surface.

The solution was to allow the blood to clot in the vasa vasorum and in the accessory arteries. This was done by surgically ligating all visible accessory arteries branching from the abdominal aorta and common iliacs before removing the blood from the lumen i.e. before inserting any cannulae. By ligating the arteries and cutting them just distal to the ligatures, blood clots forming in the occluded lumens of the accessory arteries added an extra barrier to leakage. Further, all the vessel segments that would end up as the isolated bifurcation were separated from the surrounding tissue and any periadventitial fat was removed by blunt dissection. Any bleeding through vasa vasorum exposed by these blunt procedures would then clot and prevent further leakage. Hence the order of the steps described in section 4.3.4.2 was reversed for the final surgical protocol (See section 4.3.7). An additional advantage to this strategy was that the blockage of the vasa vasorum with clots prevented tracer and water transport through them, allowing for a simple resistor model of the wall consisting of the intima and media in series without the complication of low-resistance paths in parallel.

4.3.6.2 Reducing the Duration of Anaesthesia

In addition to time savings coming just from repeating the procedures, changes to the procedure were made to reduce the total duration of the surgery to maximise the freshness of the tissue. It was found that the time taken to place iliac cannulas was reduced from 30 minutes to 15 minutes by aiming to cannulate the external iliac as oppose to the femoral arteries. Further, placing the cannula-securing ligatures all in one step reduced the number of tool changes required. Adding in the step in which all accessory arteries were manually ligated, rather than relying on glass beads to occlude them, initially increased the duration of the surgery but with practice, the whole surgery could be completed in 1 h

4.3.7 Final Surgical Protocol

The final protocol used for experiments, whose results are presented in subsequent results chapters (Chapters 5 and 6), is presented here:

4.3.7.1 Pre-operative Preparation

Male Sprague-Dawley rats (225-250 g, Charles River Laboratories, UK) were delivered >6 days prior to the scheduled experiment date. At the beginning of the week of the experiment, rats were re-located to the CBIS housing facilities to allow them to acclimatise to the new environment before experiments. They were fed a normal laboratory diet (LBS Biotechnology Ltd, UK) *ad libitum* and housed under a 12h light cycle at 20-25 °C. On the day of the experiment, the rat was observed to check for normal behaviour and posture.

TSS was prepared the day preceding the experiment and dissolved gas concentrations were allowed to equilibrate in an incubator at 37 °C with a gas composition of 5 % CO_2 and 95 % air.

4.3.7.2 Anaesthesia

Anaesthesia was induced in an induction chamber with a slowly rising concentration of isoflurane, supplied by an inflow of medical oxygen of 2-3 l$\,$min^{-1} containing 3-5 % isoflurane. Upon loss of its righting reflex, the rat was placed on a preheated temperature-controlled heat mat at 37 °C in a supine position with its mouth and nose inserted into a face mask, delivering oxygen at a flow rate of 0.7-1 l$\,$min^{-1} containing 1.5-2.5 % isoflurane. Once loss of the pedal withdrawal reflex was observed, surgery commenced. Throughout the subsequent procedures, depth of anaesthesia was constantly assessed by observing breathing rate and periodically checking for the absence of the pedal withdrawal reflex. Isoflurane concentration was adjusted to control depth of anaesthesia.

4.3.7.3 Surgical Procedure

1. Access the abdominal aorta

    (a) Perform a laparotomy by making a single midline incision through skin and abdominal muscle from a point ∼2 mm caudal to the sternum to a point ∼2 mm rostral to the scrotum

    (b) Reflect the seminal vesicles and drain the bladder if necessary to gain better access to the aortic bifurcation

    (c) Ligate the inferior mesenteric artery as close to the aorta as possible

    (d) Cut the rectum, stopping any bleeding that occurs by ligating or clamping with haemostats

    (e) Reflect the entire gut

    (f) Place two pairs of haemostats on each testicular artery and cut between them to gain better access to the abdominal aorta

(g) Ligate the ilio-lumbar arteries, caudal artery and any other accessory arteries that branch from the abdominal aorta or common iliac arteries, cutting each branching artery distal to the ligation point

(h) Clear all perivascular fat surrounding the abdominal aorta and common iliac arteries

(i) Place a ligature just distal to each iliac bifurcation and prepare a knot without tightening

(j) Place three ligatures spaced 1-2 mm apart just distal to the most distal renal artery:

i. Prepare a knot in the proximal and central ligatures without tightening

ii. Prepare a temporary knot in the distal ligature without tightening

2. Cannulate the left external iliac artery

(a) Make a longitudinal incision through the skin of the upper thigh and expose the femoral artery by further blunt dissection

(b) Follow the femoral artery to its origin on the external iliac artery and separate the artery and vein from the adjacent nerve and surrounding muscle, cutting the nerve if necessary to prevent involuntary spasm of the limb.

(c) Place three ligatures spaced 1-2 mm apart at the distal end of the external iliac artery:

i. Prepare a knot in the distal and central ligatures without tightening

ii. Prepare a temporary knot in the proximal ligature without tightening

(d) Open the 3-way tap connected to the cannula to ensure no bubbles are introduced during cannulation

(e) Tighten the distal ligature, then the temporary proximal ligature

(f) Cannulate between the central ligature and the distal ligature and secure the tip by tightening the central ligature

(g) Release the temporary proximal ligature and advance the cannula <1 mm beyond the iliac ligature placed in step 1i and tighten to secure the cannula, leaving the ends long

(h) If any blood is visible in the cannula, gently flush by temporarily raising the iliac reservoirs. Then adjust the level of the iliac reservoirs to there is no net flow of TSS into or out of the vessel

3. Cannulate the right external femoral artery by repeating the steps above

4. Cannulate abdominal aorta using the ligatures placed in step 1j:

(a) Open the 3-way tap connected to the aortic cannula to ensure no bubbles are introduced during cannulation

(b) Tighten the proximal ligature, then the temporary distal ligature

(c) Cannulate between the central ligature and the proximal ligature and secure the tip by tightening the central ligature

(d) Loosen the temporary distal ligature and advance the cannula <1 mm beyond ligature and re-tie it with a permanent knot to secure the cannula

5. Bend the arms of the stereotactic tripod to match the lengths of the arterial segments *in situ* and tie the long ends of the cannula-securing ligatures to the arms

6. Remove bifurcation from the abdomen and place directly in a temperature-controlled TSS bath at 37 °C

4.4 Development of Sample Preparation and Imaging Methods

Much of the development of the sample preparation and imaging methods described below was performed using test samples from zero-pressure experiments performed on thoracic aortic rings.

4.4.1 Preservation of Pressurised Structure

4.4.1.1 Chemical Fixation of Elastin

In order to obtain realistic images of wall structure in vessels subjected to physiologically relevant transmural pressures, it was necessary to obtain fixation of all the elastic components of the wall while still in the stressed configuration. Otherwise, elastic recoil once the pressure is removed would have introduced artefacts into the images e.g. wavy or wrinkled elastic lamellae in the tunica media. Elastin is well-known for being difficult to fix with common aldehyde fixation (Fung and Sobin, 1981), retaining it's elasticity even after prolonged fixation in a deformed state.

NaClO has been reported in the literature as a suitable fixative for elastin (Urry et al., 1988). Another possibility is to dehydrate specimens in their stressed configurations: Since much of the elastic recoil of elastin arises due to hydrophobic interactions of its constituent amino acids (Urry and Parker, 2002), complete dehydration while tissue is held in the stressed configuration may reduce any recoil artefacts.

Simple tests were devised to determine the suitability of several fixatives: Rat aortic segments were equilibrated for 24 h in TSS containing 1 % Rh-BSA. Excess tracer was washed off in PBS and samples were held in longitidunal extension by pinning to PDMS-lined dishes. They were then incubated at room temperature in the different fixatives overnight. For each fixative, half the samples were dehydrated through a graded ethanol series (50 %, 70 %, 90 %, 95 % and 100 %) while still pinned and the other half were released from the PDMS before dehydration. To account for differences in elasticity depending on the origin of the aortic segment, four different aortas were each cut into ten segments. They were then randomly assigned to a par-

ticular treatment combination. The combinations of treatments are summarised in table 4.3. Incubating in PBS was used as a negative control. 15 % formaldehyde is the standard fixative used in the laboratory because it was previously shown to be highly effective at fixing Rh-BSA in arterial tissue for confocal microscopy. Formal sublimate was prepared by first preparing a 15 % solution of formaldehyde. >6 % $HgCl_2$ was then added and mixed for 30 minutes to make a saturated solution. Excess salt was allowed to settle under gravity and the supernatant was carefully decanted. Tests of NaClO as a potential fixative were conducted following the methods outlined in Urry et al. (1988). The concentration of NaClO in laboratory bleach (Teepol) was determined by redox titration to be 3.72 M and was diluted in PBS to obtain a 0.58 M solution.

The original length (l_o), length during fixation (l_d) and final length after fixation and dehydration (l_a) of each sample were measured using digital callipers under a steromicroscope and the results expressed as percentage of strain retained after fixation and dehydration ie: Percentage of strain fixed= $\frac{\frac{l_a - l_o}{l_o}}{\frac{l_d - l_o}{l_o}}$

Treatment #	Fixative	State of tissue during dehydration
1	PBS	Stretched
2	PBS	Relaxed
3	15 % formaldehyde	Stretched
4	15 % formaldehyde	Relaxed
5	6 % $HgCl_2$	Stretched
6	6 % $HgCl_2$	Relaxed
7	Formal sublimate	Stretched
8	Formal sublimate	Relaxed
9	0.58 M NaClO	Stretched
10	0.58 M NaClO	Relaxed

Table 4.3: Summary of fixatives used in fixation and dehydration trials. Treatments 1 and 2 were included as negative controls.

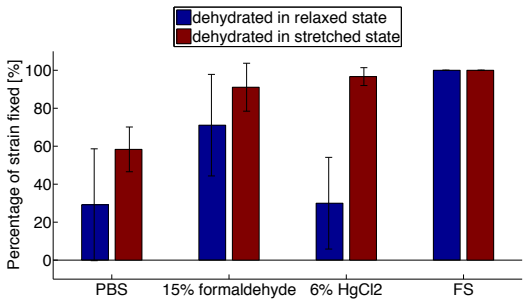


Figure 4.6: Results of fixation and dehydration trials: dehydration of stretched samples resulted in less recoil for all fixatives. FS performed best of all the fixatives, preserving 100 % of the strain.

At the end of these tests, it was noted that the samples placed in the NaClO were completely discoloured; the tracer had evidently been bleached in that fixative solution as even the solution was colourless. Therefore the final lengths of these samples were not recorded. From the elongation results, formal sublimate was

clearly the best option, combined with dehydration in the stressed configuration (Figure 4.6).

Further optimisation of the fixation with formal sublimate was done to reduce the exposure time required but to still achieve 100 % fixation of elongation and good fixation of the Rh-BSA tracer. Aortic segments were stretched by pinning to PDMS-lined petri dishes as described above and incubated in formal sublimate for 5 min, 10 min, 15 min, 30 min, 60 min and 120 min at room temperature. All samples were then dehydrated through a graded ethanol series as before and final elongation was measured. There was no difference between all samples fixed for >10 min. From previous work by other lab members, 10 min fixation in 15 % formaldehyde is insufficient to ensure fixation of all Rh-BSA molecules in the tissue; the established *in vivo* protocol calls for 30 min perfusion fixation with 15 % formaldehyde *in situ* followed by overnight post-fixation in 15 % fomaldehyde. Taking these two previous points into consideration, the final fixation protocol used in all further studies consisted of a 30 min fixation with formal sublimate, an overnight fixation in 15 % formaldehyde and dehydration through a graded ethanol series, all with the tissue in the stressed state.

4.4.1.2 Cryoembedding

One problem with using $HgCl_2$ as a fixative is its toxicity. Therefore snap-freezing arteries while still pressurised was considered as a possible alternative to prevent elastic recoil. Rat aortic segments were prepared as described in section 4.4.1.1 and snap-frozen by submerging in an isopentane bath, pre-chilled in liquid nitrogen. As expected, elongation was perfectly preserved in the frozen tissue. Due to its speed and simplicity, this technique was used as the basis for a Master's project to attempt 3D reconstruction of serial sections of stressed tissue (See section 4.4.3.1).

4.4.2 Epoxy embedding

Embedding samples in an epoxy resin would take advantage of the optical clearing effect caused by the refractive indices of most epoxy resins being similar to that of oil-based immersion media used in light microscopy. This approach would then open up the possibility of using the confocal microscope to image large tissue volumes, limited only by the working distance of the available oil-immersion lenses.

Segments of thoracic aorta obtained from rat carcasses were used as test samples and were dehydrated in a graded ethanol series (50 %, 70 %, 90 %, 95 % and 100 %), changing solutions every 10 minutes at room temperature. A final dehydration step in 100 % ethanol was done overnight. Samples were then placed in two changes of propylene oxide (PO).

Epoxy embedding medium (TAAB) was prepared by mixing 24 g Embed 812, 16 g dodecenyl succinic anhydride, 10 g methyl nadic anhydride and 1.3 ml Benzyldimethylamine. Air bubbles created by mixing were removed by centrifugation at 500 ×g for 5 minutes. Infiltration in epoxy was done through a graded series of epoxy/PO mixtures in the following ratios: 1:1; 2:1 and 100 % epoxy, changing solutions approximately every 12 h. After a final 24 h incubation in fresh 100 % epoxy, blocks were cured at 65 °C for 48 h.

4.4.3 Physical Sectioning and Image Volume Reconstruction vs 3D Imaging Techniques

With both epoxy and cryoembedding methods available, there were two possible approaches to obtain image volumes of the 3D structure of the arterial media: (1) physical sectioning and 2D imaging, followed by image registration and image volume reconstruction; or (2) optical sectioning using the z-stack imaging capabilities of the confocal laser scanning microscope (CLSM). Two alternative hybrid options were to image z-stacks of thick sections using a confocal microscope to reduce the number of image registrations required or block-face imaging on a custom-built apparatus developed in the department. All options were explored before settling on a final choice.

4.4.3.1 Image Registration of Thick Cryosections

To test the feasibility of reconstructing image volumes from thick cryosections, an MSc. project student, Cheuk Wong, was tasked with cutting 20 µm cryosections, imaging them as z-stacks using a CLSM and developing a code in MATLAB® to align, reconstructing image volumes by registering sequential slices.

Segments of rat thoracic aorta were infiltrated with a 1 % Rh-BAS tracer solution, fixed in 15 % formaldehyde overnight and placed in a cryoprotectant solution of PBS containing 20 % sucrose at 4 °C for 8 h. Cryoembedding was done using OCT cryoembedding medium (Tissue-Tek®, USA): embedding chambers were filled with OCT before placing aortic segments, orienting the longitudinal axis perpendicular to the surface of the embedding medium. Any bubbles present in the OCT were removed with a needle. An isopentane bath was cooled in a liquid nitrogen bath for 20 minutes before lowering the embedding chambers into the isopentane, only submerging them to the level of the OCT so that no bubbling occurred on the surface. Blocks were trimmed and cut using a cryomicrotome, collecting sequential sections at a thickness of 20 µm on standard glass slides and dehydrated in air.

Sections were mounted in the mounting medium prepared as described in section 4.2.2 using standard #1.5 coverslips and imaged using a CLSM (Leica TCS SP5, Leica Microsystems GmbH, Germany). Autofluorescence and Rh fluorescence images were taken using a 20 × mixed immersion lens (Leica, 20×/0.70). Autofluorescence was excited at 488 nm and its emission imaged between 495-555 nm. Rh was excited at 561 nm and its emission imaged between 585-620 nm.

Attempts to reconstruct serial slices into a complete image volume were made using MATLAB. The technique was based on control point registration wherein a user identified corresponding points in 2 consecutive slices. Although the project reached a proof of concept stage, succesfully aligning 2 consecutive slices, the quality of the reconstruction was highly dependent on the number of points selected. Thus high-quality reconstructions would require too much user input to be an efficient solution. Block-face imaging and optical sectioning were pursued in favour of this labour-intensive technique.

4.4.3.2 Block-face imaging: the Histocutter

A 3D histology technique based on imaging the freshly cut face of a block containing embedded tissues was trialled. Unlike traditional histology, where light is transmitted through thin slices of samples to acquire images, the block face is imaged using a camera which records light reflected off it, by-passing the disadvantages of traditional sectioning including distortion of slices and the high chance of losing slices within a serial set of sections.

The apparatus includes a fluorescent light source (X-CITE® 120PC Q, Lumen Dynamics), two filter sets (480/535 nm, 560/645 nm), a microscope (Nikon AZ100; magnifications: 1×, 2×, 3×, 4×, 5×, 6×, 7×, 8×) and a CCD camera (Alta U16, Apogee) are all mounted on a rigid bed with their optical axes aligned with the resting block position on an automatic microtome (RM2265, Leica Microsystems). An in-house code coordinates the individual components, acquiring serial 2D block face images: after each slice, the microtome arm returns the block to the same position each time, within the field of view (FOV) of the camera and the new block-face is imaged in 2D. As the block is advanced in the microtome, a 3D image of the sample is re-created.

Preliminary samples were made to test its applicability in generating 3D image volumes with sufficiently high resolution to resolve VSMCs to obtain geometries for fluid flow simulations. Resolution in the z-direction is limited by the microtome's minimum slice thickness of 0.5 μm and the light penetration depth into the block face. For a typical VSMC axial length of hundreds of microns, the 0.5 μm slice thickness would be sufficient. Attempts were made to limit light penetration by adding fluorescence-absorbing dye Sudan Black B (0.5 %, 1 %, 2 %, 4 % and 8 %) to epoxy embedding medium: 10 μm fluorescent beads suspended in 2 % agarose gel were embedded in Sudan black-supplemented epoxy. Since VSCM dimensions in the radial and circumferential directions are on the order of tens of microns, tests were conducted to see what x-y resolutions could be obtained by imaging a graticule at the available camera magnifications.

Epoxy containing >4% Sudan black did not cure completely. The remaining bead samples failed in limiting light penetration as light was evidently penetrating the blocks too easily: beads under the surface were being imaged at least 10 μm before they were at the block face. Thus z-resolution would effectively be in the tens-of-microns range.

x-y pixel resolutions of 1.67 μm and 0.2952 μm were obtained at 2× and 8× magnification with FOVs of 6.83 mm and 1.0 mm respectively. However, pincushion distortions were observed on the edges of the images so the useable FOV in reality was much smaller. Additionally, it should be note that these pixel resolutions are not equivalent to the maximum spatial resolution determined by the numerical aperture of the optical train. With numerical apertures of the camera lenses in the range of 0.2-0.4, we decided that the theoretical maximum x-y resolution of this instrument ($\sim$ 0.7-1.5 μm) was not sufficient to justify further attempts.

4.4.3.3 Optical Sectioning: 3D Confocal Imaging

Taking advantage of the optical properties of the epoxy-embedded tissues, optical sectioning using the Leica TCS SP5 was used to remove any need for physical sectioning and image registration. The only limitations associated with this approach were drop-off of signal intensity with increasing depth due to attenuation of both the excitation laser and the emitted fluorescence. These limitations were overcome in post-processing of the image volumes (See section 4.6).

The lateral resolution of confocal imaging is typically 2-3 times better than the axial resolution. Fibre and VSMC alignment in the tunica media is known to range from circumferential to helical. To make best use of the resolution available in the x-y plane, samples were oriented to obtain longitudinal sections so that the short axes of the VSMCs would be imaged in the higher resolution x-y plane and the long axes would be imaged in the lower resolution z-axis.

Preparation of the epoxy-embedded samples for confocal imaging was done using a low-speed rotating saw (Isomet) and wafering blades (Buehler). Excess embedding medium was cut from tissue blocks to produce cuboidal blocks of epoxy completely surrounding the bifurcation. The large faces of the cuboid were oriented parallel to the plane of the bifurcation (ie: the frontal plane of the rat). The final cut to reveal the imaging face was made in the frontal plane of the bifurcation, bisecting the aorta and both common iliac arteries to reveal two cut faces, each showing a longitudinal section of the vessels. To help orient the embedded tissue for the final cut through the bifurcation, a custom sample holder was designed to hold epoxy blocks glued to standard microscopy slides. Due to the thickness of the wafering blade, only one of these cut faces coincided with the centreline of the vessels so only one side was used for imaging. The chosen cut face was finally polished using graded abrasive papers (Buehler, 3M), lubricating the cut with water, to produce an imaging face.

4.4.4 Final Choice of Embedding, Sample Preparation and Imaging Method

After considering the advantages and disadvantages of cryo- vs. epoxy embedding and physical vs optical sectioning and block face imaging, a final decision was made to employ the methods of formal sublimate pressure fixation, epoxy embedding and optical sectioning using a confocal microscope for all experiments. The final protocol is presented below:

1. Formal sublimate fixation of tissue to preserve stressed configuration. While the tissue is held in the required stress state at room temperature:
   (a) Submerge tissue in formal sublimate fixative (15 % formaldehyde saturated with $HgCl_2$) for 30 min
   (b) Exchange the formal sublimate for 15 % formaldehyde and incubate overnight

(c) Dehydrate the tissue through a graded ethanol series (50 %, 70 %, 90 %, 95 % and 100 %), changing solutions every 10 minutes.

2. Complete dehydration: Remove stress from tissue and place in two changes of 100 % ethanol: 2 h for the first change; >12 h for the second

3. Epoxy infiltration and curing:

   (a) Place tissue in two changes of propylene oxide (PO): 2 h for the first; >12 h for the second

   (b) Place tissue in a 1:1 epoxy/PO mixture for 12 h

   (c) Place tissue in a 2:1 epoxy/PO mixture for 12 h

   (d) Place tissue in freshly prepared 100 % epoxy for 12 h

   (e) Place tissue in freshly prepared 100 % epoxy for 24 h

   (f) Cure at 65 °C for 48 h

4. Block cutting and imaging face polishing:

   (a) Cut samples into a cuboidal shape with the plane of the bifurcation lying parallel to the largest faces of the cuboid

   (b) Glue cuboidal blocks to standard microscopy slides and cut the blocks in the plane of the bifurcation

   (c) Polish the imaging face using water-lubricated abrasive papers, progressing up to 25000 grit

5. Optical sectioning:

   (a) Using a 40× oil immersion lens (Leica, 40×/1.25-0.75 oil HCX PL APO CS), locate the apex of the aortic bifurcation

   (b) Using the Leica *Mark and Find* feature, set up ∼100 µm deep z-scans at both lateral walls of the aorta, 2 mm proximal to the bifurcation apex

   (c) Scan using the settings in table 4.4

4.5 Development of Methods to Determine Rh-BSA Distribution and Available Space

To obtain geometries for numerical simulations of water transport through the arterial media, methods to determine the geometry of the tissue containing larger water-filled pores (i.e. large enough for albumin penetration) within the tunica media were developed. Many of the techniques required here are simplifications of methods developed in section 4.3 for the measurement of L_p and P in isolated bifurcations. Hence the techniques detailed in this section are presented more or less as the final methods used.

Scan parameter	Setting
Image dimension	2048×2048 pixels
Pixel width	0.130 µm
Pixel height	0.130 µm
z-step	0.168 µm
Excitation 1	458 nm
Emission 1	460-520 nm
Gain 1	799 V
Excitation 2	561 nm
Emission 2	568-620 nm
Gain 2	479 V

Table 4.4: Scan settings used to obtain high resolution 3D images of arterial tissue embedded in epoxy using the serial optical sectioning technique

4.5.1 Determination of Time Required to reach Equilibrium

In order to determine the Rh-BSA distribution at equilibrium, we first had to determine the time taken to reach a steady state of diffusion across the arterial wall. A simple experiment was done to determine this time.

Rat abdominal bifurcations were isolated from cadavers using an adapted protocol based on the method described in section 4.3.4.2 as the surgical procedures had not been fully developed at the time. The step involving cannulation of the left ventricle was omitted (Section 4.3.4.1) and all solutions were supplemented with 100 USP units ml^{-1} penicillin, 100 µg ml^{-1} streptomycin, 50 µg ml^{-1} gentamycin and 2.5 µg ml^{-1} amphotericin (Sigma-Aldrich, UK) and filter sterilised. Isolated bifurcations were pinned to PDMS-lined petri dishes and tested for leaks by determining L_p at 40 mmHg. Isolations giving a value of L_p in the 10_{-8}mmHg range at 40 mmHg were used. The vessels were disconnected from the pressurisation system and the abluminal bath was filled with 5 ml TSS tracer solution of TSS containing 1 % Rh-BSA and 3 % unlabelled BSA; 4 % unlabelled BSA in TSS was placed in the lumen. The whole assembly was placed in a tissue culture incubator at 37 °C with a gas composition of 5 % CO_2 and 95 % air . Luminal tracer concentration was monitored for up to 72 h by perfusing 1 ml fresh TSS containing 4 % BSA through the lumen and collecting the perfusate. Fluorescence intensity of the samples was read using a spectrophotometer and converted to Rh-BSA concentrations using a standard calibration curve, constructed from serial dilution of the abluminal tracer solution. Results are shown as diffusive mass transport rate in figure 4.7.

Over the first 12 h the transport rate is seen to increase before reaching a steady state. Thus equilibrium tracer distributions are reached after 12 hours. After 40 h the transport rate is seen to increase again, suggesting deterioration of the tissue.

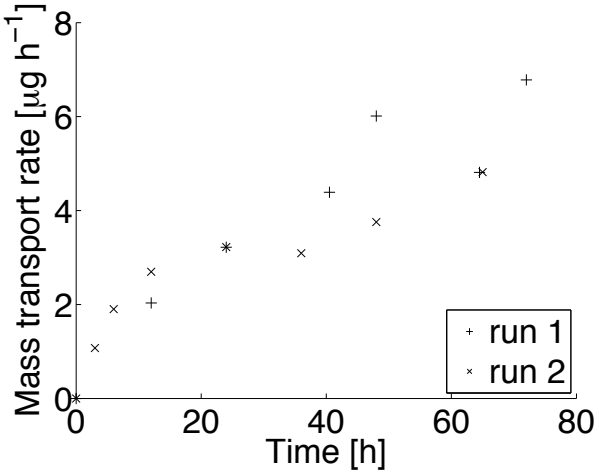


Figure 4.7: Results of 1-sided diffusion experiments performed to determine the minimum time required to reach equilibrium with Rh-BSA

4.5.2 Determination of Rh-BSA Distribution at Equilibrium

Male SD rats (300-350 g) were each given 1000 USP units heparin dissolved in 1 ml 0.9 % saline via *i.p.* injection. After 10 minutes, they were sacrificed by administering an overdose of sodium pentobarbitone (200 mg, *i.p.*). Their aortic bifurcations were carefully excised and cleaned of periadventitial tissue and pinned to a PDMS-lined petri dish containing 5 ml TSS. The lumen was gently flushed with a tracer solution of TSS supplemented with 1 % Rh-BSA, 3 % BSA, 100 USP units ml^{-1} penicillin, 100 μg ml^{-1} streptomycin, 50 μg ml^{-1} gentamycin and 2.5 μg ml^{-1} amphotericin. Finally, 5 ml tracer solution was added to the petri dish so that the vessels were just completely submerged and placed in an incubator at 37 °C with a gas composition of 5 % CO_2 and 95 % air for 6 h. The time interval of 6 h was chosen based on the results shown in the previous section; that 12 h was sufficient to reach steady diffusional transport. Setting up the same diffusion gradient from both sides of the arterial wall would be expected to more than halve the time taken to reach equilibrium. This was confirmed by inspection of cryosections taken through tissues that had been infiltrated for 3 h, 6 h, 12 h and 24 h with little change in the tracer distributions between 6 and 24 h.

The lumen and entire petri dish were briefly rinsed with fresh TSS before gently perfusing the lumen with 10 ml 15 % formaldehyde. The whole vessel preparation was then processed for 3D confocal imaging by fixation in formal sublimate, dehydration and epoxy embedding as described in section 4.4.4.

4.5.3 Determination of Rh-BSA Distribution at Steady State

After completion of L_p and P measurements, all vessel preparations were fixed by perfusion at pressure. The abluminal surface of the vessel was gently washed with fresh TSS. Excess tracer was rinsed from the lumen by opening both ilic cannula and briefly raising the iliac reservoirs 10 cm above the aortic reservoir. Pressure was then maintained by keeping the iliac cannulae open, closing the aortic cannula and lowering

the iliac reservoirs back to their original height. Samples were then processed for 3D confocal imaging as described in section 4.4.4.

4.6 Development of Image Processing Methods

4.6.1 Accounting for Signal Attenuation with Depth

The limitation of light attenuation inherent in optical sectioning can be overcome using a simple post-processing technique relying on the assumption that the brightest few pixels of each z-slice in the z-stack should be of similar intensity. (Note that the samples were not imaged from the intimal to the adventitial surface, which would have given rise to real depthwise variations in intensity.) Therefore scaling all pixel intensities within individual z-slices by some factor that causes a certain percentage of pixels in each slice to be saturated corrects for any depth-attenuation in intensity. This was implemented using the *Enhance Contrast* plugin in ImageJ.

4.6.2 Image Volume Rotation for Axis Alignment

The recurrent issue of sample orientation in embedding techniques was only partially addressed by careful block cutting in section 4.4.4. Image volume rotations were performed in FIJI to approximately align the radial, axial and circumferential axes of the tissue to the x,y and z axes of the image stack.

4.6.3 Semi-automation of image processing

As image volumes were too large to perform contrast enhancement and volume rotations using standard ImageJ and FIJI plug-ins, a custom script was written in ImageJ scripting language to run the algorithms on slices of the image volume in a semi-automated way, requiring input from a user to determine tissue bounding boxes and lines. The full code is included as Appendix B.

4.7 Computational simulations

The following section details how the effective permeability of selected subregions within the tunica media was determined. Confocal images of the equilibrium distribution of Rh-BSA in the rat abdominal aorta were obtained as described in section 4.5.2. All of the implementation for the new numerical solver was done by Dr A Comerford. The work involved in integrating the high resolution images into the computational method is the product of discussions between the author and A Comerford. The computational approach developed here was later applied with small modifications in chapters 5 and 6 to determine the effects of transmural pressure and tone, respectively, on the hydraulic conductance of arterial wall components.

4.7.1 Unsteady Brinkman's equation

The arterial media contains VSMCs embedded in an ECM comprised of structural protein filaments (eg: collagen and elastin fibres), proteoglycans, glycosaminoglycans and water. The L_p of the cell membranes

is much lower than that of the interstitium (Levick, 1987) so, although VSMCs are themselves water-filled domains, the water within VSMCs is in a separate compartment from the fluid in the porous domain that is the ECM. Since we are most interested in the flow through the ECM, the volume occupied by VSMCs can be treated as solid objects within a porous medium and flow through such a structure can be described by Brinkman's equation,

$$\frac{\partial \mathbf{u}}{\partial t} = -\nabla p + \nu \nabla^2 \mathbf{u} - \frac{\nu}{\boldsymbol{k}} \mathbf{u} + \mathbf{f}, \quad \text{in } \Omega^B \times [0, T] \tag{4.5}$$

$$\nabla \cdot \mathbf{u} = 0. \quad \text{in } \Omega^B \times [0, T] \tag{4.6}$$

where $\mathbf{u}$ is the velocity, p the pressure, ν the effective viscosity, $\boldsymbol{k}$ the Darcian permeability tensor and $\mathbf{f}$ a forcing term. The equation has been widely used for modelling transport in the arterial media (Wang and Tarbell, 1995, Huang and Tarbell, 1997, Tada and Tarbell, 2001, Dabagh et al., 2009b) as it can characterise the flow around solid obstacles embedded in a porous material (Khaled and Vafai, 2003), unlike Darcy's law; the additional term $\nu \nabla^2 \mathbf{u}$ allows for the formation of boundary layers around solid obstacles (ie: VSMCs).

4.7.2 Effective permeability

To simplify the fluid-mechanical properties of the media, we aimed to represent blocks of medial tissue as equivalent blocks of a hypothetical homogenous tissue. That is, for a given hydraulic gradient, the net hydraulic fluxes through both the heterogeneous structure and the homogeneous equivalent are the same. The permeability of the homogenous block is then defined as the effective permeability ($\boldsymbol{k}_{\text{eff}}$) of the heterogenous block of arterial media.

This concept is illustrated in figure 4.8. The heterogeneous structure consists of a porous fluid-filled domain and a solid domain, $\Omega^B = \Omega^B_f \cup \Omega^B_s$, representing the ECM and VSMCs respectively. Flow in Ω^B is governed by Brinkman's equation (Eq 4.5).The boundary of the solid domain $\partial\Omega^B_s$ (red in Figure 4.8) represents the interface between the solid and fluid domains. The boundary of the fluid domain $\partial\Omega^B_f$ is shown in blue.

To avoid the influence of boundary conditions, we applied an oversampling approach (Hou and Wu, 1997): flow fields were calculated for the whole domain Ω^B and the effective permeability was calculated for a subregion, denoted by the dashed black square in figure 4.8. The size of the dashed black region can be close to the size of Ω^B since the boundary layer thickness is $O(\sqrt{k})$ (Huang and Tarbell, 1997) and, for biological porous materials, permeability values tend to be small, $O(10^{-18} m^2)$.

The equivalent homogenous block is represented as Ω^D and its effective permeability tensor can be calculated. Flow in this domain is governed by Darcy's Equation:

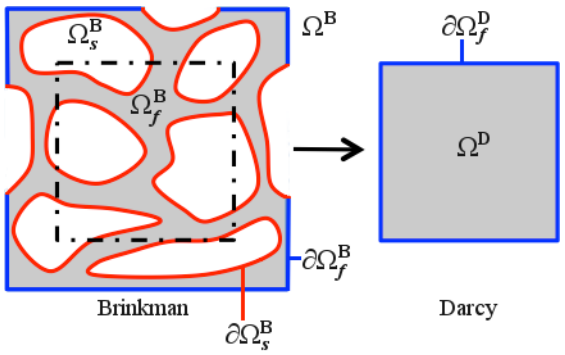


Figure 4.8: Calculating effective permeability by oversampling (After Comerford et al., 2015)

$$\langle \mathbf{u} \rangle = -\frac{1}{\nu} \boldsymbol{k}_{\text{eff}} \langle \nabla p \rangle \quad \text{in } \Omega^D \tag{4.7}$$

in which $\langle \mathbf{u} \rangle$ donates the volume average velocity and $\boldsymbol{k}_{\text{eff}}$ the permeability tensor, which is symmetric (i.e. $k_{ij} = k_{ji}$):

$$\boldsymbol{k}_{\text{eff}} = \begin{bmatrix} k_{rr} & k_{rz} & k_{r\theta} \\ k_{rz} & k_{zz} & k_{z\theta} \\ k_{r\theta} & k_{z\theta} & k_{\theta\theta} \end{bmatrix} \tag{4.8}$$

To calculate the full tensor, we form an over-determined system of linear equations by performing 3 numerical experiments in the three coordinate directions (r, z and θ). In each experiment, a pressure drop is applied to the domain in the relevant coordinate direction and the flow and pressure fields are determined in Ω^B. The resulting mean velocity field and pressure gradient are extracted from the dashed black region. This leads to the following matrix equation:

$$\mathbf{F}\mathbf{k} = \langle \mathbf{u} \rangle \tag{4.9}$$

$$\text{where} \quad \mathbf{k} = \begin{bmatrix} k_{rr} \\ k_{zz} \\ k_{\theta\theta} \\ k_{rz} \\ k_{r\theta} \\ k_{z\theta} \end{bmatrix} \quad \text{and} \quad \langle \mathbf{u} \rangle = \begin{bmatrix} \langle \mathbf{u} \rangle^1 \\ \langle \mathbf{v} \rangle^1 \\ \langle \mathbf{w} \rangle^1 \\ \langle \mathbf{u} \rangle^2 \\ \langle \mathbf{v} \rangle^2 \\ \langle \mathbf{w} \rangle^2 \\ \langle \mathbf{u} \rangle^3 \\ \langle \mathbf{v} \rangle^3 \\ \langle \mathbf{w} \rangle^3 \end{bmatrix},$$

$$\mathbf{F} = \begin{bmatrix} \langle \nabla p \rangle_r^1 & 0 & 0 & \langle \nabla p \rangle_z^1 & \langle \nabla p \rangle_\theta^1 & 0 \\ 0 & \langle \nabla p \rangle_z^1 & 0 & \langle \nabla p \rangle_r^1 & 0 & \langle \nabla p \rangle_\theta^1 \\ 0 & 0 & \langle \nabla p \rangle_\theta^1 & 0 & \langle \nabla p \rangle_r^1 & \langle \nabla p \rangle_z^1 \\ \langle \nabla p \rangle_r^2 & 0 & 0 & \langle \nabla p \rangle_z^2 & \langle \nabla p \rangle_\theta^2 & 0 \\ 0 & \langle \nabla p \rangle_z^2 & 0 & \langle \nabla p \rangle_r^2 & 0 & \langle \nabla p \rangle_\theta^2 \\ 0 & 0 & \langle \nabla p \rangle_\theta^2 & 0 & \langle \nabla p \rangle_r^2 & \langle \nabla p \rangle_z^2 \\ \langle \nabla p \rangle_r^3 & 0 & 0 & \langle \nabla p \rangle_z^3 & \langle \nabla p \rangle_\theta^3 & 0 \\ 0 & \langle \nabla p \rangle_z^3 & 0 & \langle \nabla p \rangle_r^3 & 0 & \langle \nabla p \rangle_\theta^3 \\ 0 & 0 & \langle \nabla p \rangle_\theta^3 & 0 & \langle \nabla p \rangle_r^3 & \langle \nabla p \rangle_z^3 \end{bmatrix}.$$

The subscripts (r,z,θ) denote the components and superscripts (1,2,3) denote the applied pressure drop in the radial, axial and circumferential directions, respectively. Equation 4.9 is then solved using QR-factorisation, to determine the six independent components of $\boldsymbol{k}_{\text{eff}}$. Since it is symmetric and positive definite (all non-zero components are positive as negative permeability has no physical meaning in this context), we can diagonalise the tensor:

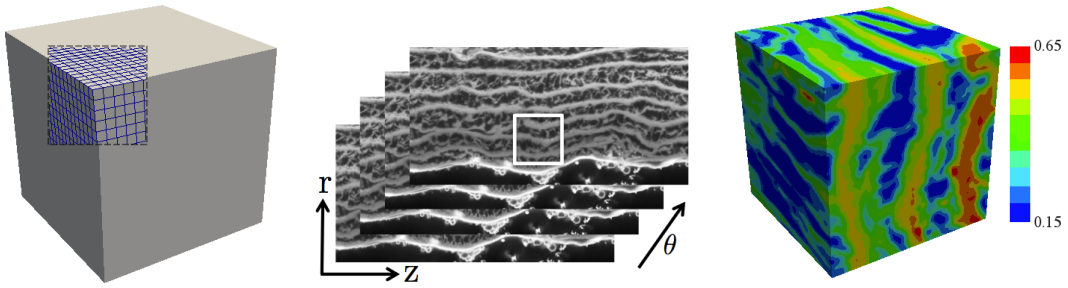
$$\boldsymbol{k}_{\text{eff}} = \begin{bmatrix} \lambda_1 & 0 & 0 \\ 0 & \lambda_2 & 0 \\ 0 & 0 & \lambda_3 \end{bmatrix} \tag{4.10}$$

in which λ_1 , λ_2 and λ_3 are the eigenvalues that represent the principal permeabilities, associated with eigenvectors $\mathbf{v_1}$, $\mathbf{v_2}$ and $\mathbf{v_3}$ which are the principal directions along which transport occurs.

4.8 Geometry and fictitious solid objects

Brinkman's equation (Eq 4.5) was solved on a domain that was discretised using the spectral/hp element library *nektar*++, using a new solver for flow in porous media implemented by A Comerford (Comerford

et al., 2015). The spectral/hp method is similar to the finite element method in that the domain is decomposed into tessellated, non-overlapping elements but differs in that the expansion within each element is high order, depicted in figure 4.9(a). Thus error in the numerical solution is minimised by either refinement of the mesh or increase in the order of the polynomials.



(a) Computational domain with inset showing quadrature points overlaid

(b) Example confocal image stack on which tracer intensity is sampled. White box represents example location where intensity is sampled.

(c) Example computational domain with normalised intensity image data at the quadrature points

Figure 4.9: Sequence of steps to transfer confocal image data to the quadrature points. (After Comerford et al., 2015)

Fluorescence intensity values were transferred from confocal images to the computational mesh, providing both a geometric representation of the medial structure and the relative permeability of the different components of the media. In the confocal images of the equilibrium distribution of Rh-BSA, fluorescence intensity of the ECM was treated as a measure of local permeability with brighter pixels representing locations with higher permeability. Selected regions of interest from the confocal images (Fig 4.9(b)) were overlaid onto the computational space and the intensity values were sampled at each quadrature point. Intensity values were normalised to the maximum image intensity and assigned at each quadrature point, giving a normalised tracer distribution extracted onto the computational mesh (Fig 4.9(c)).

To include the impermeability of VSMCs into the computational domain, permeability in the vicinity of VSMCs was lowered by adding a penalisation parameter ε to the Darcy term ($\frac{\nu}{\boldsymbol{k}}\mathbf{u}$) in equation 4.5:

$$\frac{\nu k^{-1}}{\varepsilon}\mathbf{u} \tag{4.11}$$

$$\varepsilon = \varepsilon_{fluid} = 1$$

$$\varepsilon = \varepsilon_{solid} \to 0$$

As ε approaches zero, velocity also tends to zero so the region becomes nearly impermeable. After

manual thresholding of the confocal images to identify VSMCs, ε was assigned at each quadrature point in a similar manner to the normalised intensity values described above.

In this fictitious solid obstacle method, VSMC boundaries are only weakly imposed. An alternative approach would be to enforce the boundaries by exactly meshing the solid obstacles. To compare the two methods, the results of simulations of pressure-driven flow around fictitious solid obstacles were compared against meshed solid obstacles for several 2D geometries. The resulting velocity and pressure contours were qualitatively similar and the effective permeability obtained from the two methods differed by less than 1 %. Further, it was found that setting $\varepsilon = 0.01$ was sufficient to capture solid obstacles (Comerford et al., 2015). For complex 3D geometries such as the arterial media, exactly meshing the fluid/solid boundaries would be a complex task. Since we are interested in mean effective permeability properties, this level of complexity is not necessary - the fictitious domain method yields similar results, as shown by our validation examples. Similar methods have previously been implemented for non-boundary fitted mesh methods for the incompressible Navier-Stokes equations (Khadra et al., 2000), porous media (Hwang and Advani, 2010) and solid mechanics (Düster et al., 2008).

Chapter 5

Medial Hydraulic Resistance as a Function of Transmural Pressure

5.1 Introduction

Atherosclerosis is a disease that is thought to be initiated by patchy accumulation of macromolecules in the arterial wall, as discussed previously. Chapters 2 and 3 focused on patterns of endothelial permeability as a potential explanation of the spatial heterogeneity of the disease. However, trying to explain patterns of accumulation by only looking at endothelial permeability inherently makes the assumption that the influx of macromolecules is the dominant process; instead, accumulation is an imbalance between influx and efflux of macromolecules. To investigate how this imbalance arises, we need to understand the transport of macromolecules through each layer of the concentric arrangement of tissues that make up the arterial wall.

The macromolecules of interest are large (eg LDL) and for molecules of this size, the Péclet number (Pe) is substantially greater than one (Baldwin et al., 1997, Hwang et al., 2001) so the main mechanism of transport is advection: the transport of dissolved molecules, carried by the flow of the solute. Transport of large molecules in the arterial wall is also of interest to the arterial stent community as it has implications on drug delivery to the arterial media. Studies of the anti-proliferative drug paclitaxel have shown the additional complexity that Pe is inhomogeneous through the arterial wall (Creel et al., 2000). As advection is the main transport mechanism, understanding the macromolecular transport that underlies the development of arterial disease and the efficacy of drug delivery requires characterisation of the local arterial wall transport properties for water.

The earliest work on the structural determinants of hydraulic conductance (L_p) focused on *ex vivo* measurements of water flux across segments of arteries (Tedgui and Lever, 1985, Shou et al., 2006). In a few studies, measurements were made before and after selective removal of various wall components, in an attempt to define the causes of the resistance to transmural water flow (Weinberg et al., 1997). Interpretation of such experiments is complicated by the collapse of the wall to fill the spaces occupied by the missing compo-

nents. Tedgui and Lever (1984) and Shou et al. (2006) measured L_p before and after mechanical removal of the endothelium in order to obtain L_p for the intact and denuded wall and, by subtraction, to estimate L_p for the endothelium alone. In such experiments, the removal of the endothelium introduces two complications. Firstly, removal of the endothelium may alter properties of underlying layers of the wall by removing a source of vasoactive agents (e.g. endothelin, a vasoconstrictor whose release is pressure dependent). Secondly, removal of the endothelium artificially elevates the hydraulic flux that the remaining arterial wall is exposed to, increasing tissue compaction in these layers.

More recently, numerical simulations of water flux across the wall have been performed, trying to overcome limitations inherent in experimental methods. In such studies, the geometry of the arterial media is typically simplified as a regular array of cylinders in 2D or 3D, approximating the arrangement of VSMCs, embedded in a porous medium or fibre matrix simulating the extracellular matrix (Wang and Tarbell, 1995, Huang and Tarbell, 1997, Dabagh et al., 2009b). Viewed in conjunction with earlier experimental work on the distribution volume of macromolecules in the arterial wall (Caro et al., 1980, Winlove et al., 1982, Caro and Lever, 1983, Baldwin et al., 1983), discussed previously (see chapter 1), these models can be taken to be a proof-of-concept for the idea that medial resistance to transport may have a role to play in determining macromolecular accumulation; here we aim to determine the permeability of structures more closely representing the true anatomy of the media in normal physiology.In the previous chapter, we demonstrated a numerical method based on high-resolution confocal images of the arterial media to determine the permeability of realistic medial structures obtained by equilibrating a fluorescent tracer, Rh-BSA, into arterial tissue. Here, we apply a similar method to determine the permeability of medial tissue under physiological transmural pressure and longitudinal stretch.

Alignment of ECM fibres and VSMCs in the arterial media creates heterogeneous strain fields that cause non-linear deformation of the structure when transmural pressure is altered (Holzapfel et al., 2000), resulting in cellular reorganisation. The dependence of medial permeability on this deformation is a well-known characteristic of the arterial wall but poorly understood: experimental observations of diameter and L_p show non-linear relationships with pressure (Baldwin et al., 1997, Shou et al., 2006). Previous studies modelling this dependence (Johnson and Tarbell, 2001, Klanchar and Tarbell, 1987) assumed a relationship between permeability and deformation based on models of articular cartilage (Mow et al., 1980), and, as above, used an idealisation of the true medial geometry.

The aim of this study was to determine the effects of transmural pressure within the physiological range, on the hydraulic resistance of the entire wall, the tunica media and, by subtraction, the intima. The development and validation of the experimental and numerical methods applied here are detailed in chapter 4. Slight modifications to the computational approach to study the effects of transmural pressure on water flux

through the arterial media are detailed below. Their integration into a combined computational/experimental workflow is covered in section 5.2.1. A final aim of this study was to obtain a constitutive relationship to describe the dependence of the arterial medial hydraulic permeability on tissue deformation.

5.2 Methods

5.2.1 Overview: Interconnection of experimental and computational methods

The workflow shown in figure 5.1 details the interconnections between the numerical and experimental techniques employed. Steady state hydraulic flux was measured across *ex vivo* arterial segments of known surface area at four pressures (40 mmHg, 80 mmHg, 100 mmHg and 120 mmHg) including the physiological pressure range (Fig 5.1 a). From these experimental measurements, L_p was calculated (Fig 5.1 b). Steady state distributions of Rh-BSA were obtained for the entire arterial wall using methods developed to fix and image tracer distributions within tissues in stressed configurations (See section 4.4.4). Briefly, for the duration of L_p measurements, the luminal solution was supplemented with Rh-BSA which was fixed by perfusion under the same pressure upon completion of L_p measurements using formal sublimate. The tissue was processed for epoxy embedding and serial optical sections were taken using a confocal microscope to produce high resolution 3D image volumes of the wall. Cuboidal sub-regions within the tunica media were randomly selected for further computational study (Fig 5.1 c): Image volumes were projected onto a structured computational grid and VSMCs were removed using a penalty parameter, effectively setting the permeability of VSMCs to zero. The surrounding ECM was given a permeability based on previous models of porous media that have been validated experimentally (Kim and Tarbell, 1994, Ethier, 1991). The chosen value of $k_{ECM} = 1.32 \times 10^{-18}\,\mathrm{m}^2$, represents the mean of values reported. For each block, the flow field resulting from a simulated pressure drop in each of the three coordinate directions was calculated by solving Brinkman's equation using a solver for flow in porous media, implemented in the spectral/hp element library *nektar++* (Fig 5.1 d). The results of the three numerical experiments for each block were used to calculated an effective permeability for the medial block $\boldsymbol{k}$ (Fig 5.1 e). The medial structure was examined in each medial block: VSMCs were identified by manual thresholding in FIJI and solid volume fraction change of the medial block within this pressure range was obtained (Figure 5.1f). To check for observer bias in this manual step, two observers independently set thresholds for each image volume: no systematic error was found between the two observers' values which only differed by up to 4 intensity values in each of the 8-bit images (256 levels). Parametric non-linear regression fits of these experimental and numerical data were used to obtain a constitutive relationship between medial permeability and solid volume fraction (Figure 5.1g). The intimal resistance, R_{INT}, was determined from wall and medial hydraulic resistances, R_{WALL} and R_{MED} (Figure 5.1h).

The work presented in this chapter is a collaboration between the author and Dr. A Comerford. All experiments and imaging were done by the author. The methods involved in image processing were developed

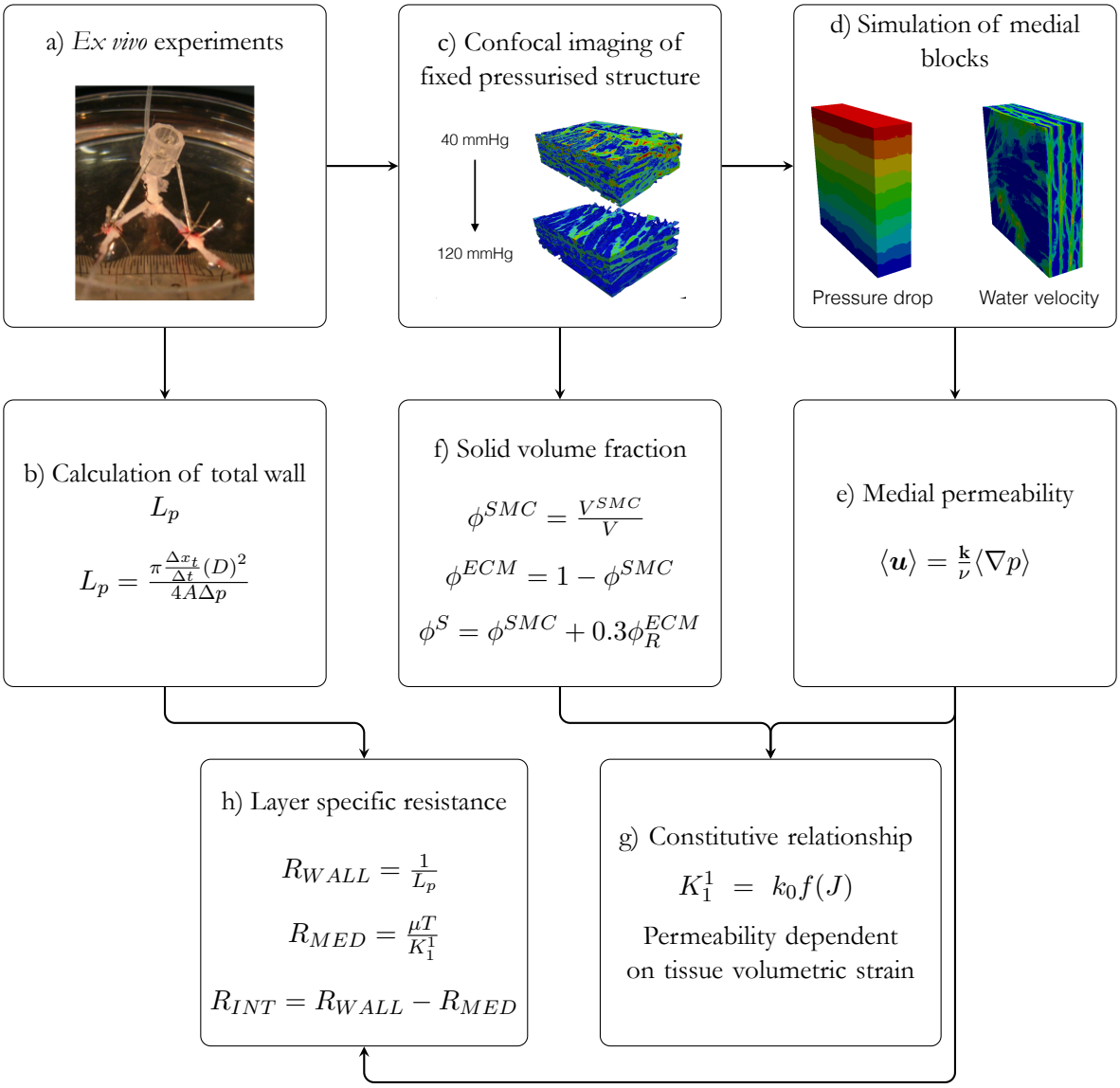


Figure 5.1: Flowchart depicting major steps in the combined computational/experimental method used to determine the relation between hydraulic resistances of arterial wall components and transmural pressure

by the author and applied by both A Comerford and the author. The methods involved in numerical experiments to obtain effective permeability and the constitutive relation between tissue deformation and medial permeability were the result of discussion between the author and A Comerford and were all implemented by A Comerford. Simulations using the resulting code were run by both A Comerford and the author using the CX1 supercomputer at Imperial College High Performance Computing facility.

5.2.2 *Ex vivo* experiments

5.2.2.1 Animals

All animal procedures complied with the Animals (Scientific Procedures) Act 1986 and were approved by the Local Ethical Review Panel of Imperial College London. Nine male Sprague Dawley rats (266±6g;

mean±SEM; Charles River, UK) were housed under a 12h light cycle at 20-25°C. They were fed a normal laboratory diet (LBS Biotechnology Ltd, UK) *ad libitum*.

5.2.2.2 Vessel isolation

The distal abdominal aorta and proximal iliac arteries were cannulated and removed from animals anaesthetised with isoflurane as described in section 4.3.3.3. The key steps in the process were preventing collapse or over-pressurisation of the arteries during the isolation by connecting the vessel to a system of reservoirs providing a constant hydrostatic pressure (Tedgui and Lever, 1984, Forster and Weinberg, 1997a) and preventing elastic recoil by tying the cannulae to a stereotactic tripod before removal of the vessels from the body to maintain arterial segment lengths and the bifurcation angle at their *in vivo* values. The whole *ex vivo* preparation was placed into a temperature-controlled TSS bath at 37°C that had been pre-equilibrated with 95% air 5% CO_2.

Figure 4.3 shows the system used to perfuse the vessel at pressure *ex vivo*. TSS supplemented with 1% Rh-BSA and 3% unlabelled BSA was introduced into the lumen and the abluminal TSS was replaced with TSS containing 4% unlabelled BSA.

5.2.2.3 Whole wall hydraulic conductance

Steady state L_p was measured at 4 transmural pressures: 40 mmHg, 80 mmHg, 100 mmHg and 120 mmHg. As described in section 4.3.3.3, outward hydraulic flux was limited to occur through the vessel wall by closing both iliac cannulae. The volume flow rate, Q, across the arterial wall was then measured by tracking bubble displacement in the graduated tracer capillary. Abluminal fluorescence was monitored over time and steady state transport was observed when fluorescence intensity increased linearly with respect to time; flow rate measurements were then taken for 25 minutes. From preliminary experiments, it was observed that 20 minutes was sufficient to achieve steady state hydraulic and tracer flux. Transient changes in flux during this period were attributed to creep of the tissue after exposure to a new pressure. Each *ex vivo* preparation was exposed to each pressure once, allowing 20 min for a steady state to be reached each time before recording the steady hydraulic and tracer fluxes for 25 minutes. The order of pressures was randomised to account for bias arising from time elapsed after isolation. Hydrostatic pressure was changed at a rate of 20mmHg/min. The outer surface area, A, of the bifurcation was determined from measurements of the arterial segment lengths, diameters and branching angles, and L_p was then calculated as $L_p = \frac{Q}{\Delta p A}$.

5.2.3 Microscopy and image processing

5.2.3.1 Fixation at pressure and embedding

The aortic bifurcations were fixed and dehydrated whilst maintaining the transmural pressure used for the final L_p measurement and without removing the vessel from the stereotactic apparatus as described in section

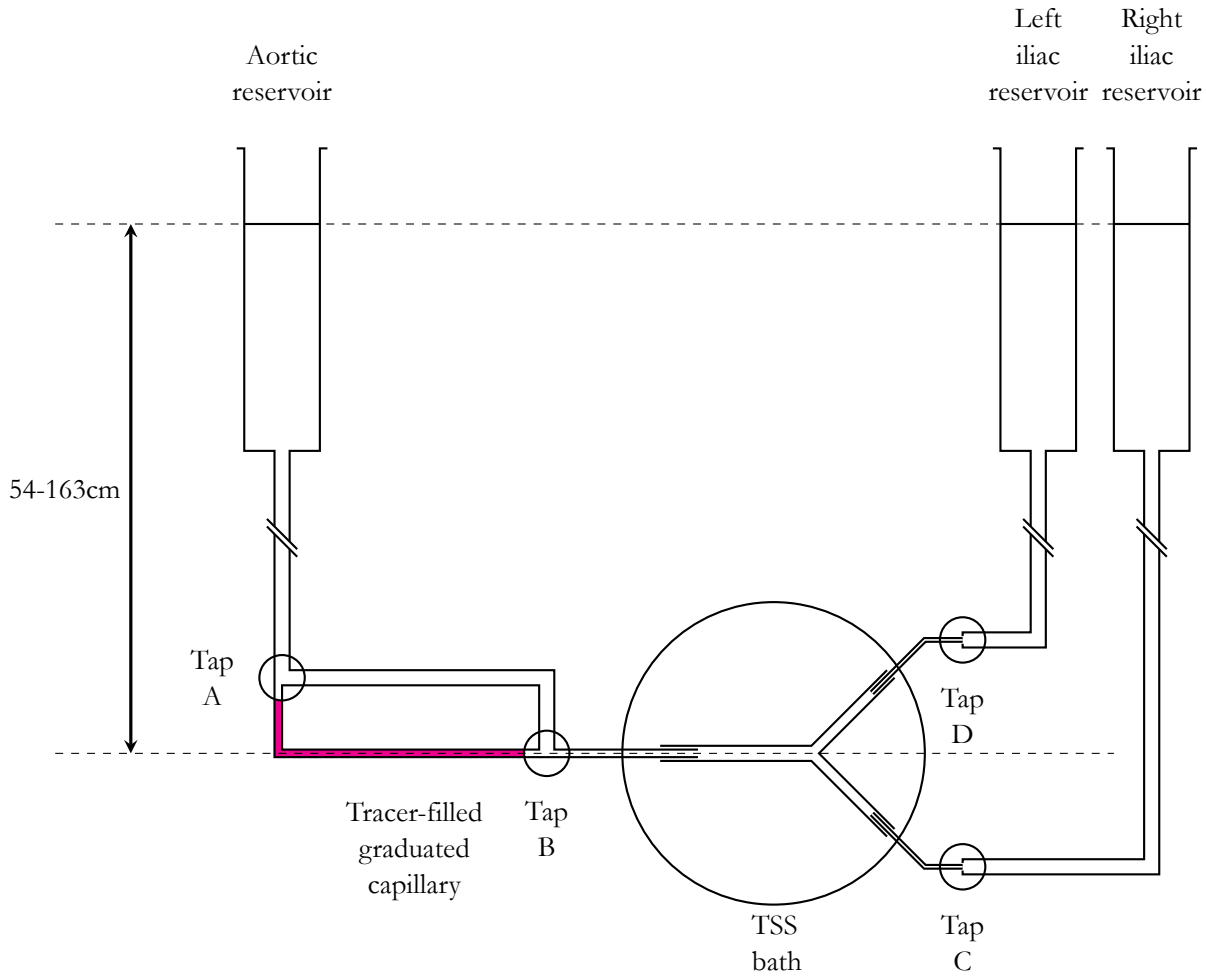


Figure 5.2: Setup of the apparatus used to apply a constant transmural pressure to vessels during isolation and during L_p and P measurements on isolated *ex vivo* vessel preparations.

4.4.4. The key step was the use of formal sublimate as the fixative followed by complete dehydration with the tissue held in its pressurised, stretched state, thus ensuring preservation of the medial structure in its stressed state.

5.2.3.2 Confocal microscopy

The lateral walls of vessels fixed at each pressure were imaged in 3D at a position 2mm proximal to the apex of the bifurcation using the methods described in section 4.4.4, also used in Comerford et al. (2015). Briefly, embedded arteries were cut in the frontal plane so that the cut face showed a longitudinal section. The cut face was polished and then imaged using an inverted laser scanning confocal microscope (Leica, TCS SP5) with the z-axis of the z-stack aligned perpendicular to the cut face.

5.2.3.3 Image processing

Image processing, to correct for intensity attenuation with depth, was performed using Fiji (Schindelin et al., 2012) as described previously (Comerford et al., 2015) but with the addition of three image volume rotations to align the imaging axes to the cylindrical coordinates of the aorta. A custom script was written in ImageJ scripting language to perform the rotations and intensity corrections as described in section 4.6.3. After rotation and attenuation correction, five blocks were extracted from images of three pieces of tissue fixed at each pressure within the physiological range (80, 100 and 120mmHg.). Additionally, two blocks were extracted from a single tissue specimen fixed at 40mmHg.

5.2.4 Effective permeability

Effective permeability describes the permeability of a hypothetical, uniform region of tissue that exhibits the same overall fluid mechanical properties as a real region of tissue with a non-uniform microstructure. We recently published our approach to determining the effective permeability of the arterial media (Comerford et al., 2015), detailed in section 4.7.2. Briefly, we first determine the flow around VSMCs in a representative region of the realistic microstructure obtained from confocal imaging data (Figure 5.1c). Flow around solid objects (ie: VSMCs) embedded in a porous matrix (ie: ECM) is described by Brinkman's equation (see Wang and Tarbell, 1995, Huang and Tarbell, 1997, Comerford et al., 2015). This process is performed in each of the coordinate directions of the arterial wall (radial, axial and circumferential directions) and from these simulations we can determine mean volumetric velocity ($\langle \mathbf{u} \rangle$) and pressure gradients ($\langle \nabla p \rangle$). Using Darcy's law:

$$\langle u \rangle = \frac{\mathbf{k}}{\nu} \langle \nabla p \rangle \tag{5.1}$$

where ν is the kinematic viscosity and $\mathbf{k}$ is the permeability tensor:

$$\mathbf{k} = \begin{bmatrix} k_{rr} & k_{rz} & k_{r\theta} \\ k_{rz} & k_{zz} & k_{z\theta} \\ k_{r\theta} & k_{z\theta} & k_{\theta\theta} \end{bmatrix} \tag{5.2}$$

we can form an over-determined system of equations that can be solved using a least squares approach to find the components of $\mathbf{k}$. This tensor can be diagonalised to find the principal components of fluid transport of the arterial wall (K_1^1 is the radial component and K_1^2 and K_1^3 are the two transverse components).

A difference between the study in chapter 4 and the present study is that in the previous one the local concentration of fluorescent tracer was used to estimate the local porosity of the ECM, as well as to identify VSMCs, whereas in the present study it was only used to identify VSMCs. The reasoning for that change arises from the differences between the experiments on which the studies are based: in the earlier experiments, no transmural pressure gradient was applied and hence tracer concentrations could reach an equilibrium; in the present study, equilibration was prevented by the application of pressure, meaning that the local tracer concentration could result from transport gradients as well as variation in porosity. While it would be wrong to assume fluorescence intensity represents ECM porosity in the present study, the VSMCs are impermeable to the tracer so it is still possible to use the images to identify the VSMCs by thresholding. The ECM in which the VSMC were embedded was assumed to have a uniform porosity and was assigned a permeability based on previous models of porous media, which have been validated against experimental data (Kim and Tarbell, 1994, Ethier, 1991); the chosen value, $k_{ECM} = 1.32 \times 10^{-18}$ m^2, represents a mean of the reported values (range: $1.22 - 1.43 \times 10^{-18}$ m^2). The same value was used at all applied pressures for two reasons: (i) the changes in the volume of the ECM were small (radial compression of the ECM measured by the method in section 5.2.6 was $\sim$5%), and (ii) the partitioning of water between different compartments of the ECM is complex and it is possible that applied stresses could increase, decrease or not affect the hydration of the part of the ECM through which the majority of water transport occurs. (For example, although increasing the transmural pressure reduced ECM volume, it might have moved water from the relatively impermeable fibrous protein compartment to the more permeable glycosaminoglycan component).

5.2.5 Porous media mixture theory

To obtain a constitutive relation describing the dependence of medial permeability on tissue deformation, we first sought to describe the deformation of the media. Porous media mixture theory is often applied to describe the mechanics of hydrated biological tissues, comprised of a mixture of fluid and solid constituents. In the case of arterial walls, the VSMCs can be treated as solid components since they are impermeable to water and therefore incompressible. The ECM occupies the remainder of the tissue volume and is comprised

of both solids (eg: collagen and elastin fibres) and a fluid, water. Deformation of soft biological tissue leads to interstitial fluid transport, which can be summarised by the biphasic theory of Mow et al. (1980). A small volume (dV) of porous medium comprises a volume of solid (dV^S) and volume of fluid (dV^F). This allows us to define the volume fraction (ϕ^S, ϕ^F) of each of the two components:

$$\phi^S = \frac{dV^S}{dV}, \quad \phi^F = \frac{dV^F}{dV} \tag{5.3}$$

For a saturated mixture (ie: there are no void spaces) these fractions must obey the saturation condition (Holmes and Mow, 1990):

$$\phi^S + \phi^F = 1 \tag{5.4}$$

For a given deformation, $\boldsymbol{F}$, the volume in the deformed state, relative to the volume in the reference configuration, V_R, is given by:

$$V = JV_R \tag{5.5}$$

where $J = det\boldsymbol{F}$. Thus we can write the solid volume fraction in the reference state:

$$\phi^S_R = J\phi^S \tag{5.6}$$

Several permeability constitutive relationships have been proposed for articular cartilage under deformation (see e.g. Holmes and Mow, 1990, Ateshian et al., 1997, Ateshian and Weiss, 2010). Following Ateshian and Weiss (2010), we write the constitutive relationship for the permeability of arterial media ($\mathbf{K}$) in the form:

$$\mathbf{K} = \sum_{a=1}^{3} K_1^a \mathbf{M}_a \tag{5.7}$$

where $\mathbf{M}_a = \mathbf{A}_a \otimes \mathbf{A}_a$ restricts the permeability to three orthogonal planes of symmetry in the arterial wall - radial (a=1) and two transverse planes (a=2,3) - and K_1^a is a function of the relative volume change (J), given by:

$$K_1^a = k_0 f(J) \tag{5.8}$$

where k_0 is the permeability at 0mmHg and $f(J)$ describes how the permeability changes with pressure-driven deformation. (In the arterial wall the circumferential and axial permeability will also depend on the orientation of the VSMCs.) k_0 and $f(J)$ can be determined using our method in section 5.2.4 for tissue pressurised at different transmural pressures.

5.2.6 Solid volume fraction

The confocal images were transformed onto the quadrature points of the computational mesh (64000 mesh elements, 8×10^6 quadrature points). Manual thresholding of the fluorescence intensities was used to divide the volume into two compartments, the volume occupied by the VSMCs (V^{VSMC}) and the remaining volume, occupied by the ECM. The volume fraction of the VSMCs (ϕ^{VSMC}) and ECM (ϕ^{ECM}) of a medial block with volume V can then be defined by:

$$\phi^{VSMC} = \frac{V^{VSMC}}{V} \text{ and } \phi^{ECM} = 1 - \phi^{VSMC} \tag{5.9}$$

Given that the ECM of the arterial wall contains 70 % water at 0 mmHg (Azeloglu et al., 2008), we determined that the remainder must be solid components such as protein filaments. Therefore we attributed 30 % of the ECM volume to be solid in the unpressurised artery. Hence $\phi^S$was defined as in equation 5.3 to include the solid constituents of the ECM. The value of 70% water reduces as the arterial wall is pressurised due to closure of pores. These closures are intrinsically included in the value of ϕ^{VSMC}, since the value is taken from the confocal data at each pressure.

$$\phi^S = \phi^{VSMC} + 0.3\phi_R^{ECM} \tag{5.10}$$

Equation 5.10 was evaluated for each pressure (40, 80, 100 and 120mmHg) and the change in volume fraction of the solid constituents in the wall - (J in equation 5.6) - was determined.

As a simple check of the permeability and solid volume fraction change results, we made estimates of radial compression by measuring the average ECM compression between VSMCs and the average VSMC thickness within the medial blocks. ECM compression was evaluated by summing the distances between VSMCs in the radial direction in a 1D measurement across the total wall thickness for transmural pressures of 80 and 120mmHg. The percentage change in ECM thickness was then determined from these two measurements. A similar approach was used to determine the mean VSMC width: the total VSMC thickness in the radial direction was determined and divided by the number of VSMCs.

5.2.7 Intimal hydraulic resistance

Using our combined computational/experimental approach it is possible to decompose the wall resistance, R_{WALL} into medial and intimal components. The arterial wall was treated as an electrical resistor network, where the intimal and medial layers provide resistances in series to water flow that add to give R_{WALL} for the entire wall. (The adventitia is ignored as it is assumed to provide little resistance to transport, relative to the media and intima due to its loose structure). R_{WALL} was obtained from the *ex vivo* experiments described in section 5.2.2.3. For the medial layer, the permeability can be reformulated as a medial resistance (R_{MED})

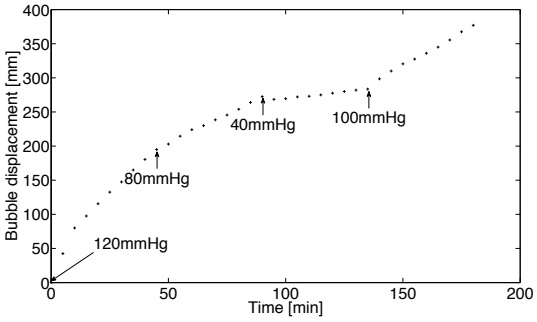


Figure 5.3: Sample trace showing bubble displacement during measurement of hydraulic flux: Pressure changes are indicated by arrows. Vessel creep and 'sealing' observed within the first 10 minutes of the experiment. Steady state hydraulic flux is obtained thereafter and re-established within 5 minutes of each new pressure being exerted.

based on thickness (T) data from the confocal images and the viscosity of water (μ):

$$R_{MED} = \frac{\mu T}{K_1^1} \tag{5.11}$$

The thickness is an average of the mean medial thickness of all tissue blocks ($T = 40\mu$m). Finally, using these results, R_{INT} can be expressed as:

$$R_{INT} = R_{WALL} - R_{MED}. \tag{5.12}$$

5.3 Results

5.3.1 Hydraulic conductance of the whole wall

The methods described in section 5.2.2.3, were used to measure L_p as a function of transmural pressure in the physiological range. An example trace showing bubble displacement over the course of an example experiment is shown in figure 5.3.

A sigmoidal function was fitted to the data using parametric non-linear regression. The selection of this function was based on the physical constraint that no convection occurs when the transmural pressure is 0mmHg and on the observation that L_p plateaus at high pressure within experimental error (Figure 5.4).

5.3.2 Permeability of the media

The results of the numerical simulations for permeability versus pressure are shown in Figure 5.5 for the radial, and the principal transverse components. The principal transverse directions do not align with the cylindrical or axial coordinates of the artery wall since VSMCs are not perfectly aligned with these directions; transport occurs preferentially along the direction of VSMC and lamellar orientation. The dotted lines were determined by parametric non-linear regression; the sigmoidal function was motivated by the distribution

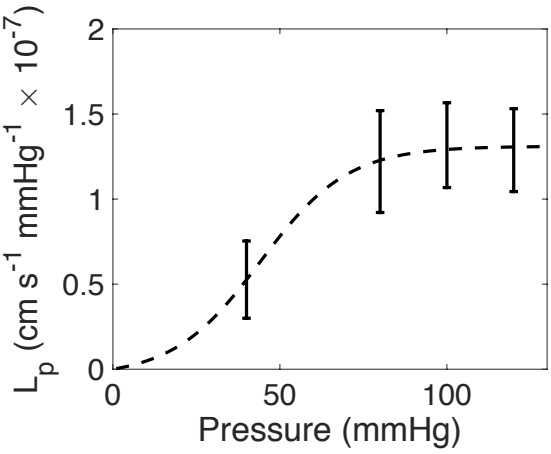
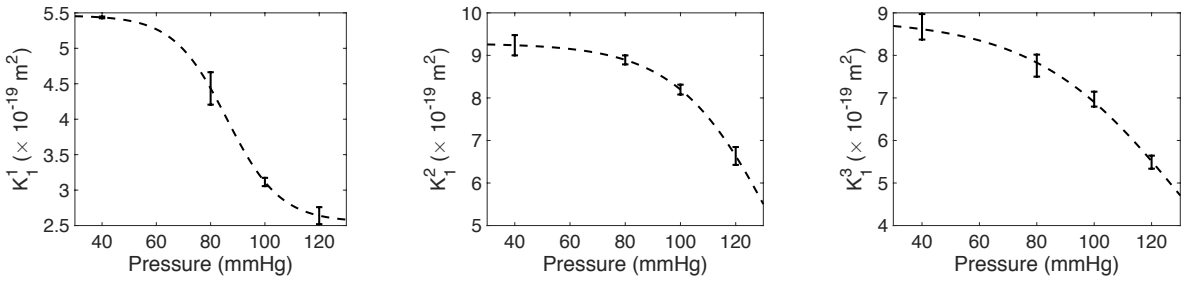


Figure 5.4: Relationship between L_p with pressure in the physiological range. Data are represented as mean ± SEM (n=7-8)



(a) (b) (c)

Figure 5.5: Relationship between permeability and pressure in the principal axes of the arterial wall. (a) radial component, K_1^1 (b) transverse component, K_1^2 (c) transverse component, K_1^3. n=5 for data at 80, 100 and 120mmHg, error bars represent SEM; n=2 at 40mmHg, error bars represent range.

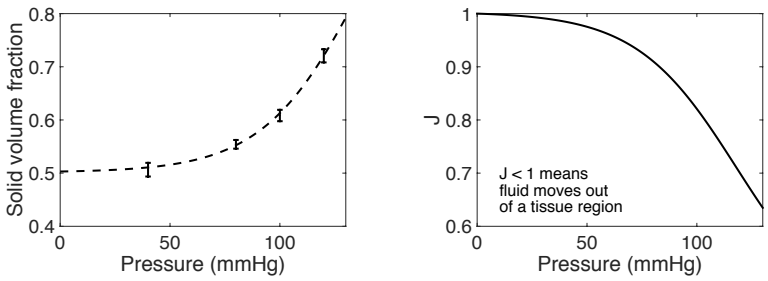
of the data (which showed small gradients of permeability at both high and low pressure) as well as by the physical constraint that the permeability will tend to zero as the pressure is elevated.

5.3.3 Solid volume fraction of the media

The solid volume fraction of the media is shown in Figure 5.6(a). As above, a sigmoidal function was fitted to the data by parametric non-linear regression, enabling the reference solid fraction ($\phi_R^S = 0.503$) to be determined. The increase in ϕ^S with pressure is due to compression of the ECM, which drives water out. Between 80 and 120mmHg, the absolute solid volume change was 23.4% and the ECM compression in the radial direction (obtained by method described in section 5.2.6) was 4.9% across the entire medial block. The ratio $\frac{\phi^S}{\phi_R^S}$ gives J (Equation 5.6), which is shown in Figure 5.6(b).

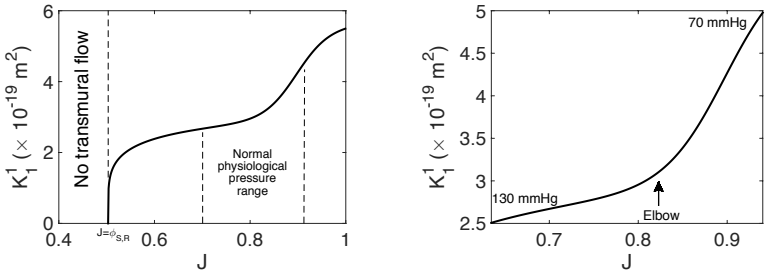
5.3.4 Empirical constitutive relationship

For the constitutive relationship we focus purely on the radial direction, since transverse pressure gradients in the wall are small compared to those in the radial direction. The relationship, shown in Figure 5.7, is



(a) (b)

Figure 5.6: Structural deformation of media due to arterial pressurisation. (a) Medial solid volume fraction increases with pressure (b) Volumetric change of solid components of the media



(a) (b)

Figure 5.7: Constitutive relation between radial medial permeability and tissue deformation. (b) Enlarged range of interest within the normal physiological range, denoted by the dotted lines in (a).

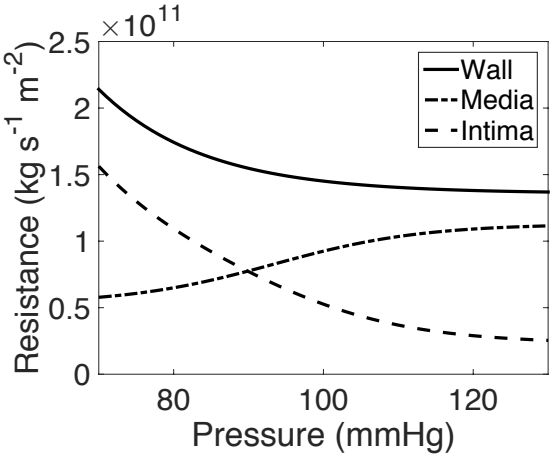


Figure 5.8: Relationship between R_{WALL}, $R_{MED}$and $R_{INT}$with pressure in the physiological range

described by the following equation:

$$K_1^1 = k_0 \left(\frac{1-\phi^S}{1-\phi_R^S} \right)^m \left[p_1 + \frac{p_2}{1+e^{(J-p_3)p_4}} \right] \tag{5.13}$$

The use of sigmoidal fits in section 5.3.2 between permeability and pressure and in section 5.3.3 between solid volume fraction and pressure dictated the mathematical form of the relation between permeability and solid volume fraction: since the two former relations are sigmoidal, this constitutive relation must also be sigmoidal.

The unknown parameters were determined by parametric nonlinear regression of the permeability and volume change data to be: $k_0 = 5.4623, m = 0.2, p_1 = 0.5463, p_2 = 0.4824, p_3 = 0.8964$ and $p_4 = 29.23$. Equation 5.13 can be separated into three distinct parts: the permeability in the reference state (k_0); a conservation constraint, $\frac{1-\phi^S}{1-\phi_R^S}$; and the physical behaviour derived from our computational/experimental approach, $p_1 + p_2/(1+e^{(J-p_3)p_4})$. The conservation constraint is a high-pressure physical constraint: when the pores that hold water are fully closed ($\phi^S = 1$; $J = \phi_R^S$), no transmural flow occurs. This theoretical limit would occur only at pressures well beyond the physiological range. The permeability in the physiological range is shown enlarged in Figure 5.7(b).

5.3.5 Intimal hydraulic resistance

R_{INT} was calculated using equation 5.12, where R_{WALL} was calculated as the reciprocal of experimental total wall L_p data and R_{MED} from equation 5.11. $R_{INT} < R_{MED}$ for pressures above 90mmHg (Figure 5.8).

5.4 Discussion

The hydraulic conductance of the whole wall, measured in our *ex vivo* experiments, more than doubled in the sub-physiological transmural pressure range (40-80 mmHg) but then remained constant in the physiological

range (80-120 mmHg). As L_p is defined as flow per unit area per mmHg pressure gradient, wall thickness is not taken into account. As wall thickness was observed to not change significantly, L_p remaining constant over the range 80-120 mmHg would mean an increase in hydraulic flux of 50 %. The dependence of aortic L_p on pressure has varied between previous studies: like us, Baldwin et al. (1992), Baldwin and Wilson (1993) and Shou et al. (2006) obtained a plateau over the physiological range, but Tedgui and Lever (1984) found a substantial decrease in L_p as pressure increased; Baldwin and Wilson (1993) and Shou et al. (2006) showed a decrease in L_p from sub-physiological to physiological pressure whereas Baldwin et al. (1992) found L_p was constant over this range. Within the physiological range of pressures, these studies also gave lower values of L_p than obtained here, presumably reflecting their use of a larger animal species and/or the thoracic aortic segment, and hence thicker test specimens.

This variation in the literature may reflect the complexity of the physical and biophysical interactions between pressure and wall thickness. On a purely physical level, increased transmural pressure results in an increase of the pressure force acting on the vessel wall and an increase in the solvent drag forces acting throughout the wall, both of which will affect wall thickness. Increased pressure will distend the vessel and thus, through the Poisson effect, will tend to reduce wall thickness. The extent of the distension will depend on the material properties of the wall; the thoracic aorta used in the four studies listed above is likely to be more elastic than the abdominal segment used here. Vessel distension would also change the internal stress field within the tissue, resulting in changes in hydration and therefore further changes in wall thickness. The increase in solvent drag forces would also have an effect on wall thickness, but the direction of change is hard to predict. Considering flow through a compressible sponge, analogous to the wall tissue, the sponge will be stretched by solvent drag if it is anchored at its upstream surface but will be compacted if it is anchored at its downstream surface. Because of the concentric layering of more and less distensible components in the wall, the actual response of the aorta to increased transmural flow is hard to predict. From a biophysical viewpoint, increased pressure force stimulates the Bayliss myogenic response of the VSMCs to stretch: As described above, an increase in transmural pressure leads to vessel distension, activating stretch-activated channels leading to a Ca^{2+}-mediated contraction. The increase in solvent drag forces can also induce VSMC contraction (Ainslie et al., 2005), further complicating the change in wall thickness. Net effects of all these factors, and of endothelium-derived vasoactive agents, on wall thickness have been measured: Baldwin et al. (1992) found a decrease in wall thickness as pressure was increased from 50 to 100mmHg, but no further change when pressure was increased to 150mmHg. In our experiments, no significant changes in thickness were observed throughout the pressure range.

Realistic microstructures obtained from confocal images of tissue fixed at different pressures were used to compute medial permeability: mapping the uptake of a fluorescent extracellular fluid-phase marker in three

dimensions allowed separation of the tissue into VSMC and ECM compartments with sub-micron spatial resolution, avoiding the assumptions of idealised medial architectures in earlier work. No free parameters were required in the simulations and only one value was taken from the literature: the average permeability of the ECM. Several values have been reported (Dabagh et al., 2009a, Wang and Tarbell, 1995, Huang and Tarbell, 1997), so it is possible that the actual ECM permeability differs slightly from the chosen value. The shape of the K_1^1 versus pressure curve would not change if the value were altered, but the absolute magnitude would. This was confirmed by increasing and decreasing the value of k_{ECM} by 20 % and repeating our permeability simulations to observe the effect of any error in the k_{ECM} value on the calculated medial resistance (Note that this 20% tolerance is much greater than the 7% range in the literature values for k_{ECM}). The calculated medial resistances consistently lay below the experimentally measured total wall resistance at all pressures, meaning the intimal resistance was never negative, so the magnitudes are at least plausible.

The simulations showed that an increase in pressure within the physiological range leads to a substantial decrease in K in all three principle axes. Variability between simulations based on different tissue samples obtained at the same pressure was small, and the changes with pressure were large in comparison, supporting the view that the trends observed with pressure are reliable. We attribute the decrease in K_1^1 to deformation of the arterial wall under increased pressure causing ECM compaction. This compaction, resulting from pore closure, was evident visually in the confocal data and confirmed by computing ϕ^S: as pressure increased from 80 to 120mmHg, the absolute volume reduction of the ECM was 23.4%. Radial compression of the ECM, obtained by the method described in section 5.2.6, was 4.9% over the same pressure range. The VSMCs, which can be considered nearly incompressible, are brought into closer proximity to one another due to ECM compaction. Additionally, the cells become thinner due to stretching. Between 80 and 120mmHg, the mean number of VSMCs per block in the radial direction increased from 3.47 to 4.34 and the mean cell width decreased from 2.11 to 1.83μm. This further increases the resistance to paracellular water transport.

Our proposed constitutive relationship captures the above observations and relates radial permeability to strain in the arterial wall for the first time (Figure 5.7). The relationship between the permeability of soft biological tissues and volume change (or volumetric strain) is well studied in the area of articular cartilage and ligament mechanics (Ateshian and Weiss, 2010, Holmes and Mow, 1990, Ateshian et al., 1997, Weiss and Maakestad, 2006). Narrowing of intercellular channels as described above accounts for more than ~80% of the permeability change within the physiological range, justifying our assumption that the ECM permeability is constant with pressure in the physiological range is valid. Note that the 'elbow' in Figure 5.7(b) is not an artefact arising from the fitting of a sigmoidal function to the permeability data (Figure 5.5(a)) - it arises from a similar kink in the relation between pressure and the change in solid volume (Figure 5.6(a)). Our results differ from previous models and assumptions (Simon et al., 1998, Klanchar and Tarbell, 1987, Johnson and Tarbell,

2001) presumably because we derived our deformation relationship from experimental data and considered the medial microstructure.

Our image-based numerical simulations also demonstrated the anisotropy of medial permeability and that this anisotropy is pressure dependent. At 80mmHg the permeability in the transverse direction was 2 times larger than in the radial direction; at 100mmHg this ratio increased to 2.6 but at 120mmHg it reduced slightly to 2.5, suggesting that additional pressurisation might further reduce anisotropy. *In vivo*, the largest pressure gradient occurs in the radial direction. Transverse components are significantly smaller, but they can arise in areas where geometrical undulations and uneven wall deformation occur.

The directionally varying trend can be explained as follows: ECM compaction causes K_1^1 to reduce at a lower pressure than $K_1^{2,3}$ due to intracellular channels narrowing preferentially in the radial direction; a result of the largest pressure gradient occuring in the radial direction. Upon wall distension, tissue stiffening in the transverse plane occurs preferentially along principal directions related to the orientation of collagen (Holzapfel and Ogden, 2010); collagen and VSMCs have similar orientations in the arterial media (Holzapfel et al., 2002). Combined, these effects promote water transport in the transverse direction, which can be considered a low resistance transport pathway, relative to radial transport. This elevated transverse flow prevents radial compression of the ECM, in a fashion analogous to hydrodynamic lubrication maintaining a gap between bearing surfaces, delaying the drop-off of permeability in the transverse directions.

A number of experiments have attempted to determine endothelial L_p by applying an electrical resistor analogy to measurements of water flux obtained before and after removal of the endothelial layer (Tedgui and Lever, 1984, 1985). As already noted, the unstated assumption that L_p for the rest of the wall is unchanged by this procedure may be incorrect since solvent drag is increased and because a source of vasoconstrictors and vasodilators has been removed. An alternative approach has been to directly measure L_p of endothelial monolayers cultured on porous substrates *in vitro* (Cancel and Tarbell, 2010, 2011) with known L_p . The drawback of this method is that the artificial environment may not fully replicate the barrier properties of the endothelium; it is known that these monolayers have elevated permeability to small proteins such as albumin that, like water, are transported through intercellular junctions.

In the present study, the combination of experimental and numerical techniques gave L_p for the whole wall and for the media, with both measurements coming from fully intact tissues, thus avoiding the limitations introduced by removal of the endothelium. Hence L_p for the intima could be obtained by subtraction. Note that we define the intimal L_p to be the hydraulic conductance of both the endothelium and any underlying structures between it and the media (ie: the basal lamina of the endothelium, intimal connective tissue and the internal elastic lamina). The implicit assumption that all the adventitia was removed when the vessel was cleaned is unlikely to be critical because the adventitia has a loose structure that is assumed to not

offer much resistance to water flux compared to the intima and media. The results presented in Figure 5.8 demonstrate that the R_{INT} is the largest component of R_{WALL} below 90mmHg whilst the medial layer dominates above 90mmHg; At 80mmHg the medial layer represents $\sim$40% of the R_{WALL}, while at 120mmHg it represents $\sim$80%. This dominance will likely increase for thicker walled arteries, in which the media contributes a higher percentage of the wall thickness; the vessel used in the present study had a medial thickness of $40 \pm 2.4\mu$m. Intimal resistance appeared to decrease with pressure. We hypothesise that this results from pressure-induced stretch of the endothelium, and the resulting shortening of the intercellular junctions. Stretch of the endothelium is known to increase permeability to albumin (Fry, 1973).

The methods applied in this study could be used to quantify other transport properties of tissue, such as diffusivity. Recently, Levin et al. (2004) showed that transmural and transverse diffusivities in segments of the calf carotid artery were significantly different for a variety drugs and macromolecules. Using our computational/experimental approach we could characterise anisotropy of drug/macromolecule diffusion in more specific locations (e.g. at sites prone to, or protected from, disease), and understand how microstructural reorganisation affects diffusivity. The binding kinetics of such drugs and their uptake by the cells would require the addition of sink terms in both the ECM domain and the SMC boundaries in our governing equations but the framework to support such investigations is already established in this study. Although, as previously discussed, the transport of LDL is advection-dominated and is the main molecule of interest with regards to the response-to-influx theory of atherosclerosis, the transport of smaller molecules is of interest when considering alternative theories of atherosclerosis (eg: oxygen in the anoxemia theory of atherosclerosis Björnheden et al., 1999) where diffusion is the dominant transport mode.

The methods employed in this study have a number of limitations. First, arteries *in vivo* are exposed to pulsatile pressures but both our experimental and numerical studies used steady pressures. It is unclear how cyclical pressure changes would affect the microstructure of the wall as the characteristic times of the cardiac cycle is much shorter than the timescales used in our steady state experiments. Second, we have treated the ECM as a homogenous medium whereas it is actually composed of different compartments of differing resistance to water flow and - potentially - different levels of water loss under applied pressure. To include such further detail would require the development of sample preparation and imaging techniques that are able to distinguish and resolve these structures.

Chapter 6

Medial Hydraulic Resistance as a Function of Medial Tone

The aim of this study was to determine the effects of altered vascular tone on the hydraulic resistance of the entire wall, the tunica media and the intima. The workflow shown in figure 6.1 details the interconnections between the numerical and experimental techniques employed. The development of all the methods used in this study are detailed in chapter 4. Some adaptations to the *ex vivo* experiments were done specifically for this study and the preliminary work and final adaptations are described in this chapter.

6.1 Introduction

The uptake of lipid-carrying plasma macromolecules is thought to be a key step in the development of atherosclerosis (Weinberg, 2004, Tarbell, 2003, 2010). The characteristically patchy accumulation of such macromolecules is the result of complex transport mechanisms into and within the arterial wall, which are only partially understood. Given that much macromolecular transport is advective (Tedgui and Lever, 1985), elucidating the mechanisms of water transport is a key step towards understanding macromolecular accumulation in the arterial wall. The study in chapter 5 demonstrated that medial hydraulic resistance accounts for most of the total wall hydraulic resistance within the physiological pressure range, even in the relatively thin-walled rat aortic bifurcation. The medial permeability in athero-prone arteries is therefore of great interest.

The medial layer of the arterial wall consists of VSMCs surrounded by a complex network of elastin, collagen and proteoglycans. Changes to the structure of this layer are likely to have an impact on the transport of water and solutes across the wall. Chapter 5 investigated the influences of changes in structure resulting from alteration of transmural pressure. It was found that the structural rearrangement of the solid components of the media gives rise to a nonlinear relation between permeability and wall strain. However, there is also an active mechanical mechanism - VSMC contraction - that could alter medial (and hence wall) permeability through effects on structure. VSMCs alter their tone or actually contract (i.e. shorten along their long axis) depending on the transmural pressure gradient; under isobaric conditions, the luminal diameter decreases and wall thickness increases (Rachev and Hayashi, 1999).

VSMC contraction can be induced by the nervous system, by chemical signals transported in the blood, by

mechanical stimuli such as stretch of the wall (Zulliger et al., 2002), and by locally-released paracrine mediators (Ludmer et al., 1986). Hypertension and obesity are examples of systemic causes associated with increased VSMC tone (Fridez et al., 2001, Meyer et al., 2013). Both are important risk factors for atherosclerosis, and may act at least in part by influencing medial transport properties. Examples of local effects are the endothelial paracrine signalling through mediators such as endothelin (ET-1) and nitric oxide (NO) (Bourque et al., 2011). More recently, the role of perivascular adipose tissue in VSMC tone control has been reported, which acts via another set of vasoactive molecules that are still yet to be identified (Meyer et al., 2013). An important implication of these sources of paracrine signalling is the potential for there to exist heterogeneous distributions of vasodilators and vasoconstrictors within the tunica media, leading to spatially varying medial permeability. This could be the basis of a mechanism to account for the patchy distribution of macromolecular accumulation and atherosclerosis. The effective radius of action of NO can be roughly estimated from its diffusion coefficient ($8.48\times10^{-10}\mathrm{m}^2/\mathrm{s}$, Liu et al., 2008)and *in vivo* half-life ($\sim$2s, Thomas et al., 2001) to be $\sim 100\mu m$, about 1.25$\times$ the radius of an EC. Thus gradients of such vasoactive signalling molecules could elicit responses of VSMC tone of approximately the same scale.

Here, we have applied our combined numerical/experimental method (Comerford et al., 2015) to investigate the effects of VSMC tone on the transmural water transport properties of the whole arterial wall and its component layers. Effects of noradrenaline-induced VSMC contraction on transmural water flux were obtained by direct measurement, effects on medial permeability were obtained by numerical methods using experimentally-derived boundary conditions, and intimal hydraulic resistance was obtained by subtraction.

6.2 Methods

6.2.1 Overview

The effect of noradrenaline (NA)-induced vasoconstriction on arterial wall hydraulic conductance, L_p, was investigated using an *ex vivo* preparation of the rat abdominal rat aorta (Figure 6.1a,b) described previously (Chooi, Comerford et al., 2015). To distinguish between VSMCs and extracellular matrix (ECM) of the wall, and hence to provide boundary conditions for the numerical simulations of medial transport, bovine serum albumin (BSA) labelled with the fluorescent dye, rhodamine (Rh-BSA), was added to the luminal fluid and its transport was allowed to reach a steady state across the arterial wall. Following completion of the L_p measurements, the Rh-BSA was chemically fixed by perfusion at pressure and its distribution was imaged by confocal microscopy (Figure 6.1c). Image volumes were transformed onto a structured computational grid and VSMCs were removed from the domain using a penalty parameter[1], effectively treating the SMCs as impermeable objects, to give realistic geometries of the tunica media for flow simulations. Flow was simulated in medial tissue blocks driven by pressure gradients imposed in each of the three orthogonal axes

[1]This parameter drives the permeability towards zero if the meshed region is within a VSMC.

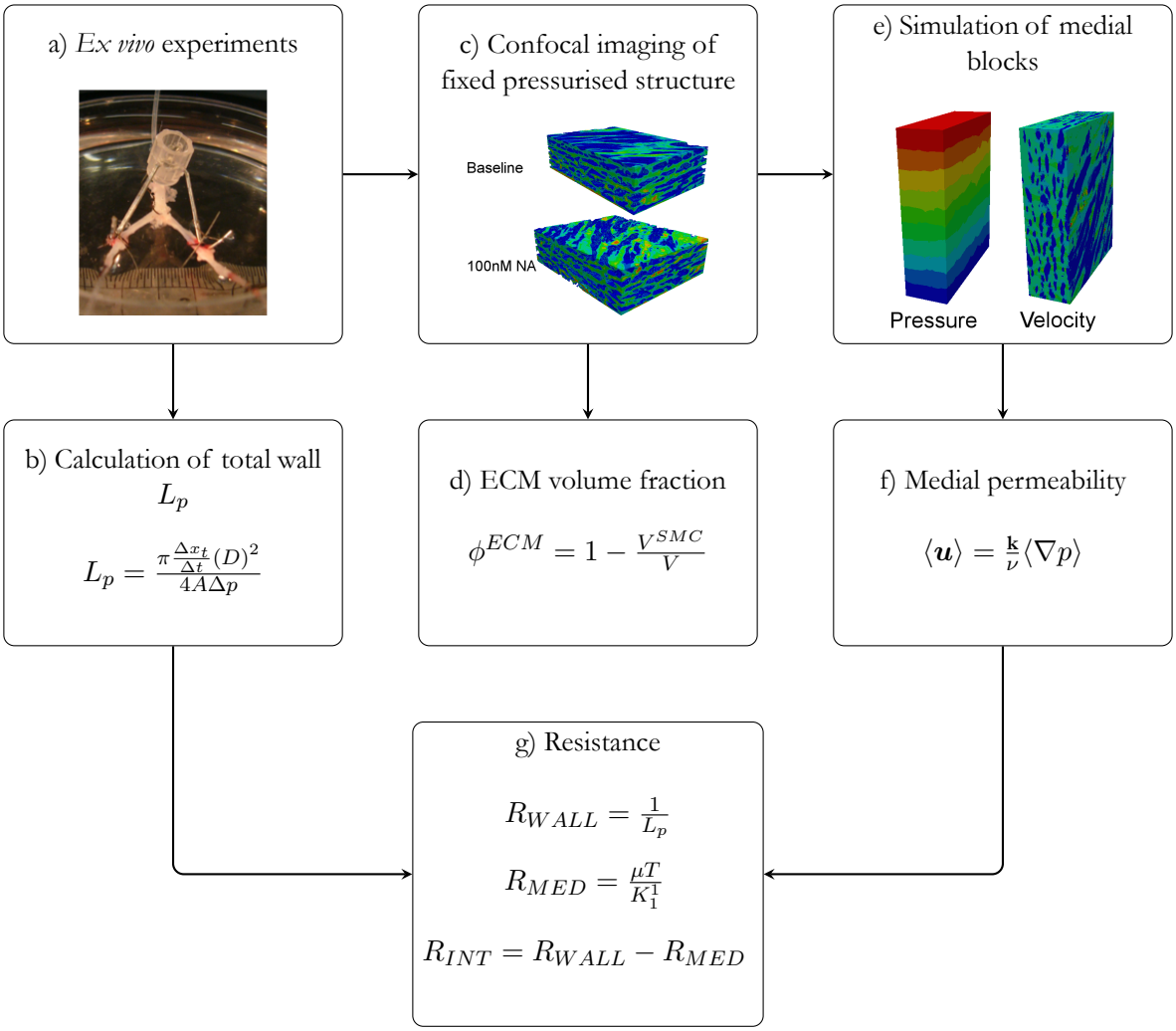


Figure 6.1: Flowchart depicting major steps in the combined computational/experimental method used to determine the effects of elevated vascular tone on the hydraulic resistance of arterial components

and the intrinsic permeability was calculated (Figure 6.1e,f). The permeability of the ECM was assumed to remain unchanged under the influence of NA. ECM volume fraction was also quantified in each medial block (Figure 6.1d). Medial thickness was measured from confocal images that were rotated and aligned with the radial direction. The total wall hydraulic resistance was finally decomposed into medial and intimal components by subtracting computationally-obtained medial resistance from experimentally-measured whole wall resistance, thus elucidating the effects of NA-induced vasoconstriction on medial and intimal hydraulic resistance (Figure 6.1g).

6.2.2 Animals

All animal procedures were approved by the Local Ethical Review Panel of Imperial College London and complied with the Animals (Scientific Procedures) Act 1986. Eight male Sprague Dawley rats (271.5±6.5g; mean±SEM; Charles River, UK) were fed a normal laboratory diet (LBS Biotechnology Ltd, UK) *ad libitum*

and housed under a 12h light cycle at 20-25°C.

6.2.3 Vessel Isolation

The *ex vivo* methods used in this study were based the method used in chapter 5. Briefly, animals were anaesthetised with isoflurane and the distal abdominal aorta and proximal iliac arteries were cannulated and removed. A system of reservoirs provided a constant hydrostatic pressure (Tedgui and Lever, 1984, Forster and Weinberg, 1997a) and prevented collapse or over-pressurisation of the arteries during the isolation. The cannulae were tied to a stereotactic tripod to maintain arterial segment lengths and the bifurcation angle at their *in vivo* before removal of the vessels from the body. The whole *ex vivo* preparation was placed into a temperature-controlled bath of Tyrode's Salt Solution (TSS; composition in g/l was 8 NaCl, 0.2 KCl, 0.2 $CaCl_2$, 0.1 $MgCl_2$, 0.05 NaH_2PO_4, 1 $NaHCO_3$, 1 glucose; pH 6.5) at 37°C that had been pre-equilibrated with 95% air 5% CO_2.

Figure 6.2 shows the system used to perfuse the vessel at pressure *ex vivo*. TSS supplemented with 1% Rh-BSA and 3% unlabelled BSA was introduced into the lumen and the abluminal TSS was replaced with TSS containing 4% unlabelled BSA.

6.2.4 Hydraulic Conductance Experiments with Noradrenaline

Steady state L_p at 100 mmHg was measured on arteries exposed to an increasing concentration of NA using methods described previously (See section 4.3.3.3). Baseline L_p in the absence of NA was measured in each specimen. NA concentration in the abluminal bath was then increased stepwise (1nM, 100nM, 10μM), allowing the water transport to reach steady state after each increase in concentration before re-measuring L_p.

6.2.5 Microscopy and image processing

6.2.5.1 Fixation of VSMC tone at pressure and embedding

Steady state tracer distributions at 100nM NA were obtained after completion of L_p measurements. Vessels were placed into a fresh abluminal saline bath containing 100nM NA until steady state transmural flux was reached. Fixation and dehydration followed immediately as described previously (See section 4.4.4). The stretch induced by the 100mmHg transmural pressure and the original vessel lengths and angles were maintained by performing the fixation without removing the vessel from the stereotactic and perfusion apparatus. The lumen and abluminal surface of the bifurcation were briefly rinsed with fresh TSS and the abluminal bath was replaced with formal sublimate (6% $HgCl_2$, 15% formaldehyde) for 30 minutes. (The use of mercuric chloride prevented elastic recoil of the vessel when it was released from the apparatus. The vessel was post-fixed in 15% formaldehyde overnight, dehydrated in a graded ethanol series (50%, 70%, 90%, 95%, 100%), and embedded in epoxy resin (EPON 812, TAAB) as described previously (Comerford et al., 2015). Baseline

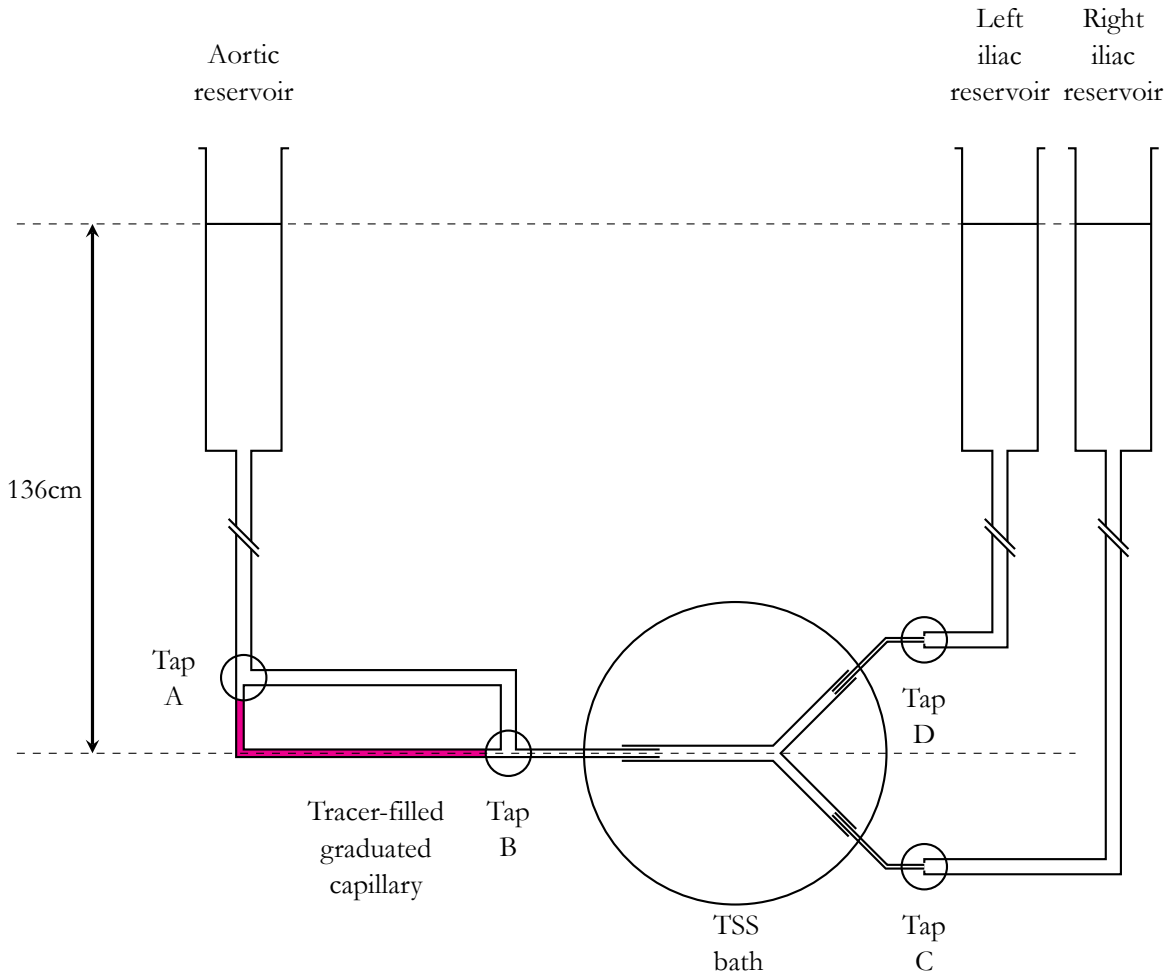


Figure 6.2: Setup of the apparatus used to apply a constant transmural pressure to vessels during isolation and during L_p and P measurements on isolated *ex vivo* vessel preparations. The reservoir height of 136 cm corresponds to a transmural pressure of 100 mmHg that was used for all experiments in this study

tracer distributions obtained in the study of chapter 5 were used.

6.2.5.2 Confocal microscopy

The lateral walls of vessels fixed at each concentration were imaged in 3D at a position 2mm proximal to the apex of the bifurcation (For full details, see section 4.4.4 and Comerford et al. 2015). Briefly, embedded arteries were cut in the frontal plane so that the cut face showed a longitudinal section. The cut face was imaged using an inverted laser scanning confocal microscope (Leica, TCS SP5) with the z-axis of the z-stack aligned perpendicular to the cut face. Rhodamine fluorescence was excited at 575nm; emission was imaged at 585-595nm.

6.2.5.3 Image processing

Four blocks were extracted from images of three pieces of tissue fixed at 100nM NA. A correction for intensity attenuation with depth was performed using Fiji (Schindelin et al., 2012) as described previously (Comerford et al., 2015) and three image volume rotations were applied to align the imaging axes to the cylindrical coordinates of the aorta. Medial thickness was measured after image rotations were applied.

6.2.6 Effective Permeability

To determine the effective permeability of a porous medium, the flow field must be determined. Flow around solid objects embedded in a porous matrix is described by Brinkman's equation (Wang and Tarbell, 1995, Huang and Tarbell, 1997, Comerford et al., 2015). In the arterial media the solid objects are the VSMCs and the surrounding medium is the porous ECM. The chosen value for ECM permeability, $k_{ECM} = 1.32 \times 10^{-18}$ m^2, was taken from the mean of published values (Wang and Tarbell, 1995, Huang and Tarbell, 1997, Dabagh et al., 2009a). The same k_{ECM} was used at both baseline and constricted states (the implications of this assumption are discussed in section 6.4)

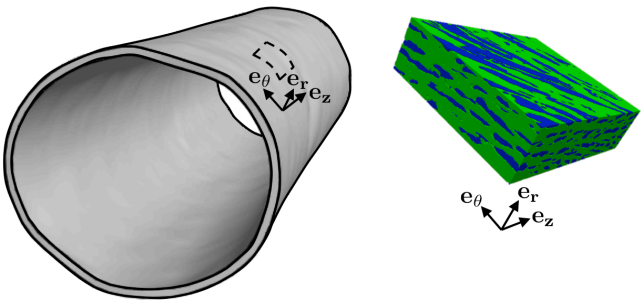


Figure 6.3: Extraction of a representative tissue region from confocal imaging of the fixed arterial media. The arterial geometry on the left shows the cylindrical coordinate system relative to the artery of an exemplar location for tissue extraction. The medial block on the right shows how the cylindrical coordinates of the artery are represented relative to the tissue block. $\mathbf{e_r}$, $\mathbf{e}_\theta$ and $\mathbf{e_z}$ are the radial, circumferential and axial directions, respectively.

Recently, we outlined an efficient approach to determine the effective permeability of the arterial media

(Comerford et al., 2015) and implemented it in the spectral/hp element framework Nektar++ (Cantwell et al., 2015). Briefly, in this approach we first determine the flow around VSMCs in a representative region of the realistic microstructure obtained from 3D confocal imaging data (Figure 6.3, the green tissue represents the extracellular matrix (ECM) and the blue regions the VSMCs). The flow field is determined in each of the main coordinate directions of the arterial wall (coordinates shown in Figure 6.3) subject to a pressure drop in that direction. From these simulations we can determine mean volumetric velocity ($\langle \mathbf{u} \rangle$) and pressure gradients ($\langle \nabla p \rangle$) Using Darcy's law:

$$\langle u \rangle = -\frac{\mathbf{k}}{\nu} \langle \nabla p \rangle \tag{6.1}$$

where ν is the kinematic viscosity and $\mathbf{k}$ is the permeability tensor:

$$\mathbf{k} = \begin{bmatrix} k_{rr} & k_{rz} & k_{r\theta} \\ k_{rz} & k_{zz} & k_{z\theta} \\ k_{r\theta} & k_{z\theta} & k_{\theta\theta} \end{bmatrix} \tag{6.2}$$

The volume averaged results are then combined to form an over-determined system of equations that can be solved using a least squares approach to find the components of $\mathbf{k}$. This amounts to a homogenisation of the microscale transport to provide a macroscopic description. The tensor in equation 6.2 can be diagonalised to find the principal components of fluid transport of the arterial wall (K_1^1 is the radial component and K_1^2 and K_1^3 are the two transverse components). As in chapter 5, we focus on the radial principal component since this is the dominant transport direction as it is the transmural pressure gradient with the largest magnitude

6.2.7 ECM Volume Fraction

The confocal data were transformed onto the quadrature points of the computational mesh (64000 mesh elements, 8×10^6 quadrature points). Thresholding fluorescence intensities divided the volume into two compartments: the volume occupied by the VSMCs and the remaining volume, corresponding to the ECM (V^{ECM}). The volume fraction of the ECM (ϕ^{ECM}) of a medial block with volume V can then be defined by:

$$\phi^{ECM} = \frac{V^{ECM}}{V} \tag{6.3}$$

Between the baseline and 100 nM NA the increase in volumetric strain generated within the ECM can be determined. This strain relative to the baseline is given by:

$$J = \frac{\phi^{ECM}}{\phi_B^{ECM}} \tag{6.4}$$

where ϕ_B^{ECM} is the volume fraction of the ECM in the baseline configuration.

6.2.8 VSMC aspect ratio

The aspect ratio (AR) of VSMCs in baseline and constricted conditions were calculated. In each block, utilising watershed segmentation, the VSMCs were separated in each slice of the image stack using the scikit-image processing library (van der Walt et al., 2014). This segmentation algorithm allows apparently connected VSMCs (e.g VSMCs might be pressed against each other) to be separated into two distinct cells. In brief, the confocal images were manually thresholded to form binary images. A distance map was generated by determining the local minima in pixel intensity in each VSMC and creating a map of distance from the nearest local minimum, thus the distance map now represented each VSMC as a mountain with their boundaries represented as valleys. The distance map was then inverted so each VSMC was represented as a basin, surrounded by a watershed. The watershed algorithm then floods the basins, which represent the VSMCs. The line on which two basins meet represents the boundary of two adjacent cells. For each cell, AR was determined, defined as the minor diameter over the major diameter. For each block the results were collected into 50 bins in the interval $AR \in [0, 1]$.

6.2.9 Intimal hydraulic resistance

Intimal hydraulic resistance, R_{INT} was determined by a combination of our experimental and computational results. Total wall hydraulic resistance, R_{WALL} was calculated from experimental measurements of L_p (Equation 6.5). Medial resistance, R_{MED}, was obtained from medial permeability (K_1^1) and thickness (T) from the confocal images and the viscosity of water (μ) (Equation 6.6). As the layers of the arterial wall are arranged in series, intimal resistance can be calculated (Equation 6.7).

$$R_{WALL} = \frac{1}{L_p} \tag{6.5}$$

$$R_{MED} = \frac{\mu T}{K_1^1} \tag{6.6}$$

$$R_{INT} = R_{WALL} - R_{MED}. \tag{6.7}$$

6.3 Results

6.3.1 Comparison of Hydraulic Conductance with and without NA

The methods described in section 6.2.4, were used to measure L_p as a function of NA concentration at a transmural pressure of 100 mmHg. An example trace showing bubble displacement over the course of an example experiment is shown in figure 6.4. Unsteady transmural hydraulic flux was observed upon increas-

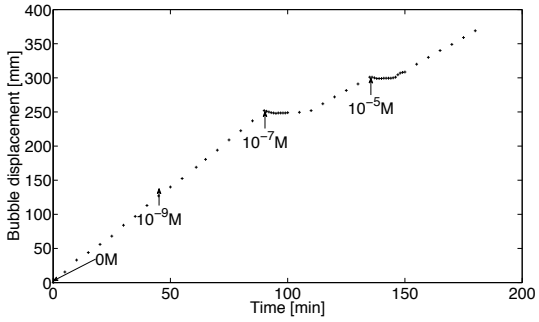


Figure 6.4: Sample trace showing bubble displacement during measurement of hydraulic flux: NA concentrations are indicated by arrows. Vessel creep and 'sealing' observed within the first 10 minutes of the experiment. Contractions observed at the beginning of the two highest concentrations. Steady state hydraulic flux is obtained after VSMC contractions reach steady tone.

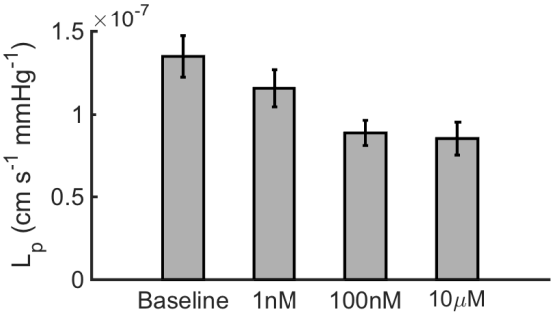


Figure 6.5: Total wall L_p was significantly reduced in the presence of NA at concentrations >100nM ($p = 0.004$, $n = 7$ at 100mM; $p = 0.001$, $n = 5$ at 10μM, paired t-tests). Error bars represent SEM.

ing NA concentration to the two highest concentrations. The durations of these periods of unsteady flux correspond to the typical time-scales taken for VSMC contraction reported in earlier studies (Furchgott and Bhadrakom, 1953) thus the reduction in luminal volume, indicated by backwards displacement of the bubble, was attributed to contraction of VSMCs.

Measurements of L_p showed that exposure of the artery to concentrations of NA of 100nM was sufficient to achieve a significantly lower conductance ($p = 0.004$, paired t-test) and that further increase in concentration did not produce a greater response (Figure 6.5). Hence all computational studies focused on two conditions: baseline (0M NA) and 100nM NA, henceforth referred to as the constricted condition.

6.3.2 VSMC contraction and Volume Fraction

The image slices shown in figure 6.6 represent a slice through 3D image volumes in baseline and constricted samples. The difference in VSMC size is visually evident: the baseline sample contains larger, wider cells than in the constricted tissue. Due to non-alignment of cells in the circumferential direction, some VSMCs appear smaller than others since VSMCs do not have uniform cross sectional area but rather have a fusiform shape (Clark and Glagov, 1985).

The visual observation in Figure 6.6(a,b) is characterised quantitatively by considering a histogram of the

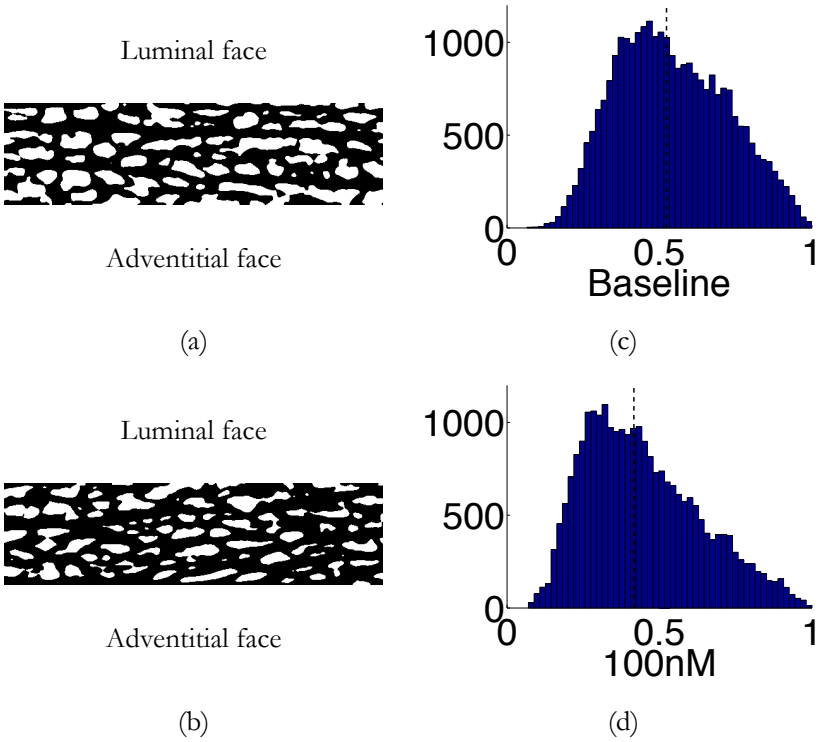


Figure 6.6: Thresholded image of a single slice of the 3D confocal stack through the media for typical baseline (a) and constricted (b) samples: white areas represent VSMCs; black areas represent ECM. (c) & (d): Decrease in aspect ratio of VSMCs during contraction. The black dotted line represents the median aspect ratio

VSMC ARs (Figure 6.6(c,d)). Between baseline and 100nM NA there is a shift of the histogram to the left demonstrating that the VSMCs are less elliptical in their contracted state (median AR values for baseline and contacted were 0.5232 and 0.4163, respectively).

6.3.3 Medial hydraulic permeability

Radial hydraulic permeability results from numerical simulations are shown in figure 6.8. K_1^1 in the constricted case was significantly higher than in baseline controls.

6.3.4 Decomposition of wall hydraulic resistance

As described in section 6.3.1, L_p in constricted arteries was significantly lower than in baseline controls ($p = 0.004$, paired t-test). Thus R_{WALL} was significantly higher in constricted arteries ($p = 8.87 \times 10^-4$, paired t-test). Paradoxically, a corresponding reduction in R_{MED} was observed: K_1^1 was significantly higher in constricted samples than in baseline ($p = 4.50 \times 10^-8$) and medial thickness (T), measured from confocal images, increased from 33.54±2.16μm to 40.20±2.68μm. These values were used in equation 6.6. Despite a 20% increase in medial thickness the 61% increase in K_1^1 produced an overall decrease in R_{MED}. Applying the electrical resistance analogy set out in section 6.2.9, a 2.5-fold increase in R_{INT} was observed (Figure 6.9).

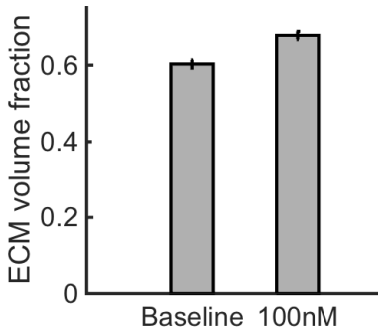
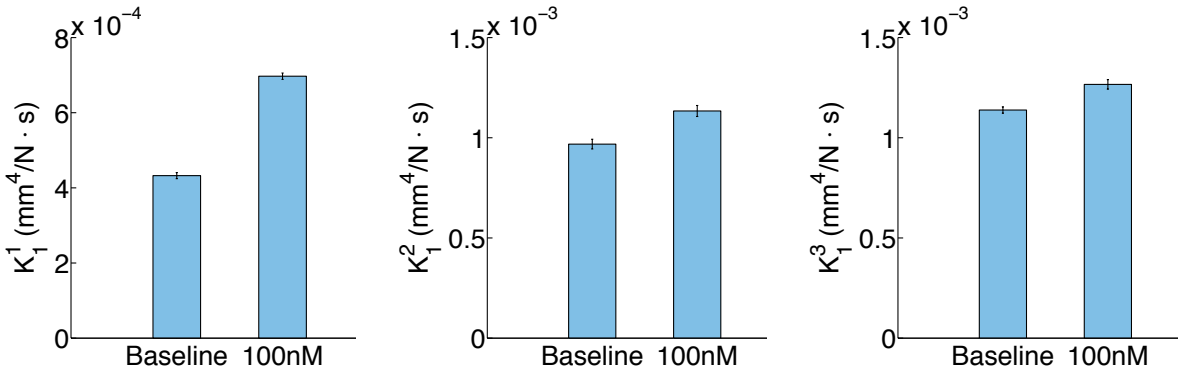


Figure 6.7: ECM volume fraction was significantly increased in the media of constricted arteries ($p = 9.12 \times 10^-4$ unpaired t-test). Error bars represent SEM. n=5 (baseline); n=4 (constricted).



(a) (b) (c)

Figure 6.8: Relationship between permeability and tone in the principal ages of the arterial wall. (a) Radial medial hydraulic permeability, K_1^1, was significantly increased in the constricted arteries ($p = 4.50 \times 10^-8$ unpaired t-test). Error bars represent SEM. n=5 (baseline); n=4 (constricted). (b) transverse component, K_1^2 (c) transverse component, K_1^3

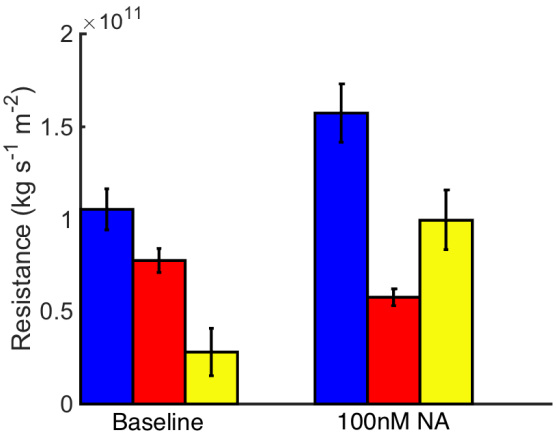


Figure 6.9: Decomposition of total wall hydraulic resistance: Blue=R_{WALL}; Red=R_{MED}; Yellow=R_{INT}. Error bars represent SEM. n=8 (baseline); n=7 (constricted).

6.4 Discussion

From L_p measurements (figure 6.5), it was clear that a 100nM NA concentration was sufficient to produce a significant decrease in L_p. Exposure of vessels to concentrations above this had no further effect.

During contraction, VSMCs change in shape, shortening along their long axis and widening in the other two axes (Seifter et al., 2005). The long axes of VSMCs are usually aligned at some angle away from the axis of the vessel (Holzapfel et al., 2002). Therefore an increase in medial thickness is expected upon constriction of an artery. Previously, it has been shown that following VSMC contraction the inner diameter decreases and the wall thickness increases to reduce circumferential stress (Rachev and Hayashi, 1999). In our experiments, the latter was observed with medial thickness increasing from $33.54\pm1.25\mu m$ in baseline controls to $40.2\pm1.34\mu m$ in constricted arteries (p=0.044).

In addition to change in medial thickness, we observed an increase in ϕ_{ECM} (Figure 6.7) between the baseline and 100 nM NA, leading to the 61% increase in K_1^1 (Figure 6.5). The increase in ϕ_{ECM} can be expressed in terms of a volumetric strain(J): between the baseline and 100 nM NA the volumetric strain in the wall increased by 11.7%, which suggests an increase in the available space for water transport to occur. The dilatation of the ECM under VSMC contraction is due to cell-generated forces pulling on the fibres of the ECM: contractile elements within VSMCs are known to be mechanically connected to extracellular fibres (eg: collagen) through integrins (Moiseeva, 2001, Ye et al., 2014, Bursa et al., 2011), causing a widening of intercellular channels as seen in figure 6.6 and increasing the strain in the matrix.

Contraction of VSMCs was seen to change their cross-sectional shape: in the baseline configuration, the cross-section of the VSMCs was more circular whilst in the constricted state, the VSMCs flattened in the radial direction, evidenced by a skew of the aspect ratio towards zero. This suggests that the known shortening on their long axis (approximately in the circumferential direction) results in an elongation in the axial direction.

The experimental data show that R_{WALL} increases upon NA-induced contraction. However, the medial permeability data, derived from fixed tissue at the end of each experiment, shows a decrease in R_{MED}. Although the decrease in R_{MED} may seem counter-intuitive, given the 20% increase in medial thickness, the increase in medial permeability (61%) outweighs the increase in medial thickness and thus dominates the behaviour of R_{MED}. R_{INT} must have increased during constriction to explain the overall increase in R_{WALL}. This is in line with the observations that the medial thickness increases, leading to a reduction in luminal surface area, over which the same number ECs must be distributed.

One limitation of this study arrises from applying a constant value of k_{ECM} for all simulations, taken from a mean of all values in the literature (Kim and Tarbell, 1994, Ethier, 1991). The inherent assumption here is that NA has no overall affect on k_{ECM}. Although VSMC contraction would open small pores in the ECM,

increasing the permeability, this effect would be small compared with the opening of intercellular spaces. This observation is backed up by figures 6.7 and 6.8, where a small ECM volume fraction change results in a large radial permeability change. Furthermore, since this study is a comparison of R_{MED} between constricted and baseline conditions, the exact value of k_{ECM} is not critical; the relative difference would remain constant for any other value of k_{ECM}. However, as R_{MED} lies below R_{WALL} and is in the right order of magnitude, the value of k_{ECM} used is likely to be similar to the true value.

Chapter 7

Conclusions

7.1 Summary of Key Findings

Addressing the five research aims highlighted in section 1.5, five key findings are summarised below.

The results of chapter 2 showed that patterns of EBA hotspots change in an age-dependent manner in a similar way to patterns of lesion prevalence but patterns of mitosis did not. Furthermore, no correlation between mitosis and EBA hotspot data was found in either immature or mature rabbits. This observation could suggest that other cell cycle events (eg: apoptosis) may be the dominant process underlying the formation of leaky junctions. However, strong correlations were found between hotspot uptake and non-hotspot uptake at both ages, suggesting that there is a common underlying mechanism for uptake through leaky junctions and normal junctions.

The study presented in chapter 3 showed similarities between the pattern of large molecule hotspots and patterns of EBA hotspots, lesion prevalence and Rh-BSA uptake in immature rabbits. Similarities between patterns of large molecule hotspot and mitosis were not found, supporting the idea of the existence of a continuum of junctional widths. In mature rabbits, the pattern of large molecule hotspots did not resemble the pattern of EBA hotspots, although it was different from the immature pattern. The reason for this discrepancy was not elucidated, but it is consistent with the view that small and large macromolecules have different transport routes, with different spatial distributions, in mature arteries. If correct, that would have significant implications for the relevance to atherosclerosis of the many published studies concerning arterial albumin transport.

Several experimental, imaging and numerical techniques were developed and validated (See chapter 4). Their application as part of a combined numerical/experimental workflow described in chapters 5 and 6 lead to a number of novel results, detailed below.

The study in chapter 5 determined the effective permeability of the arterial media at 3 transmural pressures within the physiological range. Volumetric strain of the medial structure was quantified and a constitutive relation between radial medial permeability and strain was derived from the experimental and numerical

results. Finally, the hydraulic resistance of the arterial wall was decomposed into an intimal and a medial component, showing that medial resistance is up to three times greater than intimal resistance within the physiological range. The resistances of the intima and media changed in opposite directions with applied pressure.

Chapter 6 showed that medial resistance in constricted arteries was lower than in unconstricted arteries. Additionally, the endothelial resistance was shown to be the dominant component of total wall resistance in constricted arteries. As with pressure, the effect of constriction on resistance was in the opposite direction for the intima and media.

7.2 Wider Applicability of Tools and Techniques Developed

The automated spot segmentation method in presented in chapter 2 can be applied to find local peaks in image data where background fluorescence is inhomogeneous but where the application of background flattening would adversely affect the data contained in the peaks. The statistical methods to evaluate significance of correlations between 2D maps also presented in chapter 2 can be applied to all 2D datasets in which spatial autocorrelation would artificially inflate significance and where paired data are unavailable. In cases where an *a priori* reason to expect linear relations exists, Spearman's correlation coefficient should be used instead of Pearson's rank correlation coefficient. This would only require the simple substitution of the in-built MATLAB functions.

The automated branch mouth masking algorithm presented in chapter 3 is applicable to all multi-channel image data sets where ostia or other cuts in the tissue (e.g. made for ease of sample mounting) exist. The spot segmentation algorithm can be applied to any image dataset where features of interest are expected to be of intensities far greater than the background intensity, and where the background intensity is spatially homogeneous.

Many of the methods described in chapter 4 can be applied, with minor modifications, to many other areas of study. The surgical methods developed for the isolation of arterial segments maintaining transmural pressure and vessel lengths throughout can easily be adapted to study other large arteries. Although the anaesthesia procedures could require revision, the basic method can also be adapted for use in other mammals. The sample preparation and embedding methods can be used in all studies requiring the fixation of stressed tissues in their deformed configurations. The 3D optical sectioning method is suitable for all soft tissue studies but compatibility of fluorophores with the solvents involved in the embedding should first be checked.

The combined numerical/experimental workflow described in chapters 5 and 6 could be applied to the study of any transport process through any porous tissue, provided 3D images of sufficient resolution showing its structure can be obtained.

7.3 Recommendations for Future Work

The leaky-junction cell turnover hypothesis of Weinbaum et al. (1985) postulates that enlarged cell junctions occur as a result of cell cycle events including mitosis and apoptosis. The studies presented in chapters 2 and 3 considered only the mitotic rate and found no correlation between patterns of mitosis and patterns of hotspot distribution. An obvious continuation of this work would be to obtain data on the apoptotic rate of ECs around intercostal ostia of age-matched rabbits.

In chapter 3, the mature pattern of large molecule hotspots did not match patterns of EBA hotspots and Rh-BSA uptake, suggesting a different transport mechanism could be involved. Furthermore, the work on EC boundary segmentation to determine if large molecule transport predominantly occurs through cell junctions was only pursued up to the point of a preliminary image processing algorithm. Points for further work on these aspects of the project are detailed in section 3.4.1.

The result of chapter 6, that endothelial hydraulic resistance is the dominant component of total wall resistance in constricted arteries requires further investigation into potential causes of this phenomenon.

7.3.1 Further development of experimental methods

The experimental methods to measure L_p and P presented in chapter 4 could be developed further. The substitution of the passive pressure reservoirs for an actively pressure-controlled circuit would allow measurements in arteries exposed to cyclic pressure variations, simulating the *in vivo* environment more closely. The technique could also be modified to allow spatially resolved measures of L_p and P to be made. Early attempts to do this by mounting a mock-up of the setup on the stage of an inverted confocal microscope to film the flux of tracer crossing the tissue over time failed due to convection in the abluminal bath. Future attempts might be more successful with inverted wide-field fluorescence imaging where heating of the abluminal bath is not confined to a small area. Finally, using a flow-controlled circuit instead of a pressure-controlled circuit could lead to interesting experiments to investigate the effects of changing the flow within the bifurcation by manipulating the ratio of the luminal flows in the daughter branches.

Bibliography

K. M. Ainslie, J. S. Garanich, R. O. Dull, and J. M. Tarbell. Vascular smooth muscle cell glycocalyx influences shear stress-mediated contractile response. *Journal of Applied Physiology*, 98(1):242--249, 2005.

S. M. Albelda, P. M. Sampson, F. R. Haselton, J. M. McNiff, S. N. Mueller, S. K. Williams, A. P. Fishman, and E. M. Levine. Permeability characteristics of cultured endothelial cell monolayers. *Journal of applied physiology (Bethesda, Md. : 1985)*, 64(1):308--322, 1988.

N. Anitschkow. Experimental atherosclerosis in animals. In E. Cowdry, editor, *Arteriosclerosis: A survey of the problem*, pages 271--322. Macmillan, 1933.

G. Ateshian and J. Weiss. Anisotropic hydraulic permeability under finite deformation. *Journal of biomechanical engineering*, 132(11):111004, 2010.

G. Ateshian, W. Warden, J. Kim, R. Grelsamer, and V. Mow. Finite deformation biphasic material properties of bovine articular cartilage from confined compression experiments. *Journal of biomechanics*, 30(11):1157--1164, 1997.

E. U. Azeloglu, M. B. Albro, V. A. Thimmappa, G. A. Ateshian, and K. D. Costa. Heterogeneous transmural proteoglycan distribution provides a mechanism for regulating residual stresses in the aorta. *American journal of physiology. Heart and circulatory physiology*, 294(3), 2008.

E. L. Bailey, E. Bazigou, P. S. Sowinski, and P. D. Weinberg. Mass transport properties of the rabbit aortic wall. *PloS one*, 10(3), 2015.

A. Baldwin, M. Lever, and C. Caro. Effect of noradrenaline, sodium nitrite and isosorbide dinitrate on albumin transport in the wall of the excised rabbit common carotid artery. *Atherosclerosis*, 46(1):1--11, 1983.

A. L. Baldwin and L. M. Wilson. Endothelium increases medial hydraulic conductance of aorta, possibly by release of EDRF. *The American journal of physiology*, 264(1 Pt 2), 1993.

A. L. Baldwin, C. P. Winlove, and C. G. Caro. Structural response of the rabbit thoracic aorta and inferior vena cava to in situ collapse. *Artery*, 10(6):420--439, 1982.

A. L. Baldwin, L. M. Wilson, and B. R. Simon. Effect of pressure on aortic hydraulic conductance. *Arteriosclerosis, Thrombosis, and Vascular Biology*, 12(2):163--171, 1992.

A. L. Baldwin, L. M. Wilson, I. Gradus-Pizlo, R. Wilensky, and K. March. Effect of atherosclerosis on transmural convection and arterial ultrastructure. *Arteriosclerosis, Thrombosis, and Vascular Biology*, 17(12): 3365--3375, 1997.

A. I. Barakat, P. A. Uhthoff, and C. K. Colton. Topographical mapping of sites of enhanced HRP permeability in the normal rabbit aorta. *Journal of biomechanical engineering*, 114(3):283--292, 1992.

S. E. Barnes and P. D. Weinberg. Contrasting patterns of spontaneous aortic disease in young and old rabbits. *Arteriosclerosis, thrombosis, and vascular biology*, 18(2):300--308, 1998.

S. E. Barnes and P. D. Weinberg. Strain-dependent differences in the pattern of aortic lipid deposition in cholesterol-fed rabbits. *Experimental and molecular pathology*, 71(2):161--170, 2001.

G. Bazzoni and E. Dejana. Endothelial Cell-to-Cell junctions: Molecular organization and role in vascular homeostasis. *Physiological Reviews*, 84(3):869--901, 2004.

F. P. Bell, J. B. Somer, I. H. Craig, and C. J. Schwartz. Patterns of aortic evans blue uptake in vivo and in vitro. *Atherosclerosis*, 16(3):369--375, 1972.

T. Björnheden, M. Levin, M. Evaldsson, and O. Wiklund. Evidence of hypoxic areas within the arterial wall in vivo. *Arteriosclerosis, Thrombosis, and Vascular Biology*, 19(4):870--876, 1999.

S. L. Bourque, S. T. Davidge, and M. A. Adams. The interaction between endothelin-1 and nitric oxide in the vasculature: new perspectives. *American Journal of Physiology - Regulatory, Integrative and Comparative Physiology*, 300(6):R1288--R1295, 2011.

M. Breakspear, M. J. Brammer, E. T. Bullmore, P. Das, and L. M. Williams. Spatiotemporal wavelet resampling for functional neuroimaging data. *Human brain mapping*, 23(1):1--25, 2004.

J. Bursa, R. Lebis, and J. Holata. Tensegrity finite element models of mechanical tests of individual cells. *Technology and health care: official journal of the European Society for Engineering and Medicine*, 20(2):135--150, 2011.

A. Callanan, Niall, Michael, and Tim. *Tissue-Engineered Extracellular Matrices (ECMs) as Adjuvant Scaffolds for Endovascular Aneurysmal Repair (EVAR)*. InTech, 2011.

L. M. Cancel and J. M. Tarbell. The role of apoptosis in LDL transport through cultured endothelial cell monolayers. *Atherosclerosis*, 208(2):335--341, 2010.

L. M. Cancel and J. M. Tarbell. The role of mitosis in LDL transport through cultured endothelial cell monolayers. *American Journal of Physiology - Heart and Circulatory Physiology*, 300(3):H769--H776, 2011.

L. M. Cancel, A. Fitting, and J. M. Tarbell. In vitro study of LDL transport under pressurized (convective) conditions. *American Journal of Physiology - Heart and Circulatory Physiology*, 293(1):H126--H132, 2007.

C. Cantwell, D. Moxey, A. Comerford, A. Bolis, G. Rocco, G. Mengaldo, D. De Grazia, S. Yakovlev, J.-E. Lombard, D. Ekelschot, B. Jordi, H. Xu, Y. Mohamied, C. Eskilsson, B. Nelson, P. Vos, C. Biotto, R. Kirby, and S. Sherwin. Nektar++: An open-source spectral/hp element framework. *Computer Physics Communications*, 192:205--219, 2015.

B. A. Caplan and C. J. Schwartz. Increased endothelial cell turnover in areas of in vivo evans blue uptake in the pig aorta. *Atherosclerosis*, 17(3):401--417, 1973.

C. G. Caro and M. J. Lever. Effect of vasoactive agents and applied stress on the albumin space of excised rabbit carotid arteries. *Atherosclerosis*, 46(1):137--146, 1983.

C. G. Caro, J. M. Fitz-Gerald, and R. C. Schroter. Atheroma and arterial wall shear observation, correlation and proposal of a shear dependent mass transfer mechanism for atherogenesis. *Proceedings of the Royal Society of London B: Biological Sciences*, 177(1046):109--133, 1971.

C. G. Caro, M. J. Lever, Z. Lever-Rudich, F. Meyer, N. Liron, W. Ebel, K. H. Parker, and C. P. Winlove. Net albumin transport across the wall of the rabbit common carotid artery perfused in situ. *Atherosclerosis*, 37 (4):497--511, 1980.

Y. L. Chen, K. M. Jan, H. S. Lin, and S. Chien. Ultrastructural studies on macromolecular permeability in relation to endothelial cell turnover. *Atherosclerosis*, 118(1):89--104, 1995.

J. M. Clark and S. Glagov. Transmural organization of the arterial media. the lamellar unit revisited. *Arteriosclerosis, Thrombosis, and Vascular Biology*, 5(1):19--34, 1985.

L. A. Clarke, Z. Mohri, and P. D. Weinberg. High throughput en face mapping of arterial permeability using tile scanning confocal microscopy. *Atherosclerosis*, 224(2):417--425, 2012.

P. Clifford, S. Richardson, and D. Hemon. Assessing the significance of the correlation between two spatial processes. *Biometrics*, 45(1):pp. 123--134, 1989.

A. Comerford, K. Y. Chooi, M. Nowak, P. D. Weinberg, and S. J. Sherwin. A combined numerical and experimental framework for determining permeability properties of the arterial media. *Biomechanics and modeling in mechanobiology*, 14(2):297--313, 2015.

R. M. Conroy, K. Pyörälä, A. P. Fitzgerald, S. Sans, A. Menotti, G. De Backer, D. De Bacquer, P. Ducimetière, P. Jousilahti, U. Keil, I. Njølstad, R. G. Oganov, T. Thomsen, H. Tunstall-Pedoe, A. Tverdal, H. Wedel, P. Whincup, L. Wilhelmsen, and I. M. Graham. Estimation of ten-year risk of fatal cardiovascular disease in europe: the SCORE project. *European Heart Journal*, 24(11):987--1003, 2003.

C. J. Creel, M. A. Lovich, and E. R. Edelman. Arterial paclitaxel distribution and deposition. *Circulation research*, 86(8):879--884, 2000.

S. G. Cremers, S. J. Wolffram, and P. D. Weinberg. Atheroprotective effects of dietary l-arginine increase with age in cholesterol-fed rabbits. *British Journal of Nutrition*, 105:1439--1447, 2011.

M. Dabagh, P. Jalali, and Y. T. Konttinen. The study of wall deformation and flow distribution with transmural pressure by three-dimensional model of thoracic aorta wall. *Medical engineering & physics*, 31(7):816--824, 2009a.

M. Dabagh, P. Jalali, and J. M. Tarbell. The transport of LDL across the deformable arterial wall: the effect of endothelial cell turnover and intimal deformation under hypertension. *American journal of physiology. Heart and circulatory physiology*, 297(3):H983--H996, 2009b.

M. E. DeBakey, G. M. Lawrie, and D. H. Glaeser. Patterns of atherosclerosis and their surgical significance. *Annals of surgery*, 201(2):115--131, 1985.

R. W. DeBlois, E. E. Uzgiris, S. K. Devi, and A. M. Gotto. Application of laser self-beat spectroscopic technique to the study of solutions of human plasma low-density lipoproteins. *Biochemistry*, 12(14):2645--2649, 1973.

A. Düster, J. Parvizian, Z. Yang, and E. Rank. The finite cell method for three-dimensional problems of solid mechanics. *Computer methods in applied mechanics and engineering*, 197(45):3768--3782, 2008.

P. Dutilleul, P. Clifford, S. Richardson, and D. Hemon. Modifying the t test for assessing the correlation between two spatial processes. *Biometrics*, 49(1):pp. 305--314, 1993.

R. Estrada, G. A. Giridharan, M.-D. Nguyen, T. J. Roussel, M. Shakeri, V. Parichehreh, S. D. Prabhu, and P. Sethu. Endothelial cell culture model for replication of physiological profiles of pressure, flow, stretch, and shear stress in vitro. *Anal. Chem.*, 83(8):3170--3177, 2011.

C. R. Ethier. Flow through mixed fibrous porous materials. *AIChE J.*, 37(8):1227--1236, 1991.

B. A. Ewins, J. Majewicz, T. J. Staughton, and P. D. Weinberg. Two-dimensional maps of short-term albumin uptake by the immature and mature rabbit aortic wall around branch points. *Journal of biomechanical engineering*, 124(6):684--690, 2002.

B. A. Forster and P. D. Weinberg. Changes with age in the influence of endogenous nitric oxide on transport properties of the rabbit aortic wall near branches. *Arteriosclerosis, Thrombosis, and Vascular Biology*, 17(7): 1361--1368, 1997a.

B. A. Forster and P. D. Weinberg. Evans' blue dye abolishes endothelium-dependent relaxation of rabbit aortic rings. *Atherosclerosis*, 129(1):129--131, 1997b.

P. G. Frank, S. E. Woodman, D. S. Park, and M. P. Lisanti. Caveolin, caveolae, and endothelial cell function. *Arteriosclerosis, Thrombosis, and Vascular Biology*, 23(7):1161--1168, 2003.

P. Fridez, A. Makino, H. Miyazaki, J.-J. Meister, K. Hayashi, and N. Stergiopulos. Short-term biomechanical adaptation of the rat carotid to acute hypertension: contribution of smooth muscle. *Annals of biomedical engineering*, 29(1):26--34, 2001.

D. L. Fry. Responses of the arterial wall to certain physical factors. In R. Porter and J. Knight, editors, *Atherogenesis: Initiating Factors*, pages 100+. Associated Scientific Publishers, 1973.

Y. C. Fung and S. S. Sobin. The retained elasticity of elastin under fixation agents. *Journal of biomechanical engineering*, 103(2):121--122, 1981.

R. F. Furchgott and S. Bhadrakom. Reactions of strips of rabbit aorta to epinephrine, isopropylarterenol, sodium nitrite and other drugs. *Journal of Pharmacology and Experimental Therapeutics*, 108(2):129--143, 1953.

D. C. Goff, D. M. Lloyd-Jones, G. Bennett, S. Coady, R. B. D'Agostino, R. Gibbons, P. Greenland, D. T. Lackland, D. Levy, C. J. O'Donnell, J. Robinson, J. S. Schwartz, S. T. Shero, S. C. Smith, P. Sorlie, N. J. Stone, and P. W. F. Wilson. 2013 ACC/AHA guideline on the assessment of cardiovascular risk. *Circulation*, 129(25 suppl 2):01.cir.0000437741.48606.98--S73, 2013.

H. Heinle and V. Lindner. The binding of evans blue to collagen and elastin in elastic tissue. *Archives of Physiology and Biochemistry*, 92(1):13--17, 1984.

R. A. Herrmann, R. A. Malinauskas, and G. A. Truskey. Characterization of sites with elevated LDL permeability at intercostal, celiac, and iliac branches of the normal rabbit aorta. *Arteriosclerosis, Thrombosis, and Vascular Biology*, 14(2):313--323, 1994.

M. Holmes and V. Mow. The nonlinear characteristics of soft gels and hydrated connective tissues in ultrafiltration. *Journal of biomechanics*, 23(11):1145--1156, 1990.

G. Holzapfel and R. Ogden. Constitutive modelling of arteries. *Proceedings of the Royal Society of London A: Mathematical, Physical and Engineering Sciences*, 466(2118):1551--1597, 2010.

G. A. Holzapfel, T. C. Gasser, and R. W. Ogden. A new constitutive framework for arterial wall mechanics and a comparative study of material models. *Journal of Elasticity*, 61(1):1--48, 2000.

G. A. Holzapfel, T. C. Gasser, and M. Stadler. A structural model for the viscoelastic behavior of arterial walls: Continuum formulation and finite element analysis. *European Journal of Mechanics - A/Solids*, pages 441--463, 2002.

T. Y. Hou and X. Wu. A multiscale finite element method for elliptic problems in composite materials and porous media. *Journal of computational physics*, 134(1):169--189, 1997.

Z. J. Huang and J. M. Tarbell. Numerical simulation of mass transfer in porous media of blood vessel walls. *American Journal of Physiology - Heart and Circulatory Physiology*, 273(1):H464--H477, 1997.

C.-W. Hwang, D. Wu, and E. R. Edelman. Physiological transport forces govern drug distribution for Stent-Based delivery. *Circulation*, 104(5):600--605, 2001.

W. Hwang and S. G. Advani. Numerical simulations of stokes--brinkman equations for permeability prediction of dual scale fibrous porous media. *Physics of Fluids*, 22:113101, 2010.

M. Johnson and J. M. Tarbell. A biphasic, anisotropic model of the aortic wall. *Journal of biomechanical engineering*, 123(1):52--57, 2001.

K. Khadra, P. Angot, S. Parneix, and J.-P. Caltagirone. Fictitious domain approach for numerical modelling of navier-stokes equations. *International Journal for Numerical Methods in Fluids*, 34(8):651--684, 2000.

A. R. Khaled and K. Vafai. The role of porous media in modeling flow and heat transfer in biological tissues. *International Journal of Heat and Mass Transfer*, 46(26):4989--5003, 2003.

W.-S. Kim and J. M. Tarbell. Macromolecular transport through the deformable porous media of an artery wall. *Journal of Biomechanical Engineering*, 116(2):156+, 1994.

N. Kingsbury. The dual-tree complex wavelet transform: A new technique for shift invariance and directional filters. pages 319--322, 1998.

M. Klanchar and J. M. Tarbell. Modeling water flow through arterial tissue. *Bulletin of mathematical biology*, 49 (6):651--669, 1987.

Y. Komarova and A. B. Malik. Regulation of endothelial permeability via paracellular and transcellular transport pathways. *Annual Review of Physiology*, 72(1):463--493, 2010.

LASA and RSPCA. Good practice for humane killing, 2011.

J. R. Levick. Flow through interstitium and other fibrous matrices. *Quarterly journal of experimental physiology (Cambridge, England)*, 72(4):409--437, 1987.

J. R. Levick. *An introduction to cardiovascular physiology*. Arnold, 2003.

A. Levin, N. Vukmirovic, C.-W. Hwang, and E. Edelman. Specific binding to intracellular proteins determines arterial transport properties for rapamycin and paclitaxel. *Proceedings of the National Academy of Sciences of the United States of America*, 101(25):9463--9467, 2004.

S. J. Lin, K. M. Jan, G. Schuessler, S. Weinbaum, and S. Chien. Enhanced macromolecular permeability of aortic endothelial cells in association with mitosis. *Atherosclerosis*, 73(2-3):223--232, 1988.

S. J. Lin, K. M. Jan, S. Weinbaum, and S. Chien. Transendothelial transport of low density lipoprotein in association with cell mitosis in rat aorta. *Arteriosclerosis (Dallas, Tex.)*, 9(2):230--236, 1989.

S. J. Lin, K. M. Jan, and S. Chien. Role of dying endothelial cells in transendothelial macromolecular transport. *Arteriosclerosis (Dallas, Tex.)*, 10(5):703--709, 1990.

V. Lindner and H. Heinle. Binding properties of circulating evans blue in rabbits as determined by disc electrophoresis. *Atherosclerosis*, 43(2-3):417--422, 1982.

X. Liu, P. Srinivasan, E. Collard, P. Grajdeanu, J. L. Zweier, and A. Friedman. Nitric oxide diffusion rate is reduced in the aortic wall. *Biophysical journal*, 94(5):1880--1889, 2008.

P. L. Ludmer, A. P. Selwyn, T. L. Shook, R. R. Wayne, G. H. Mudge, R. W. Alexander, and P. Ganz. Paradoxical vasoconstriction induced by acetylcholine in atherosclerotic coronary arteries. *New England Journal of Medicine*, 315(17):1046--1051, 1986.

M. R. Meyer, N. C. Fredette, M. Barton, and E. R. Prossnitz. Regulation of vascular smooth muscle tone by adipose-derived contracting factor. *PloS one*, 8(11), 2013.

Y. Mohamied, E. M. Rowland, E. L. Bailey, S. J. Sherwin, M. A. Schwartz, and P. D. Weinberg. Change of direction in the biomechanics of atherosclerosis. *Annals of biomedical engineering*, 43(1):16--25, 2015.

E. P. Moiseeva. Adhesion receptors of vascular smooth muscle cells and their functions. *Cardiovascular research*, 52(3):372--386, 2001.

V. C. Mow, S. C. Kuei, W. M. Lai, and C. G. Armstrong. Biphasic creep and stress relaxation of articular cartilage in compression: Theory and experiments. *Journal of biomechanical engineering*, 102(1):73--84, 1980.

E. Mukwevho, T. A. Kohn, D. Lang, E. Nyatia, J. Smith, and E. O. Ojuka. Caffeine induces hyperacetylation of histones at the MEF2 site on the glut4 promoter and increases MEF2A binding to the site via a CaMK-dependent mechanism. *American Journal of Physiology - Endocrinology and Metabolism*, 294(3):E582--E588, 2008.

C. L. Murphy. *Arterial Mass Transport in Relation to Flow*. PhD thesis, Imperial College London, 1998.

C. L. Murphy and M. J. Lever. Sulphorhodamine-B-labelled albumin uptake around the ostium of the renal artery in rabbits: changes with age. *Journal of vascular research*, 39(2):104--113, 2002.

R. Nairn. *Fluorescent Protein Tracing. Edited by R.C. Nairn ... Second Edition. [With Plates.]*. Edinburgh & London, 1964.

Y. Nakashima, A. S. Plump, E. W. Raines, J. L. Breslow, and R. Ross. ApoE-deficient mice develop lesions of all phases of atherosclerosis throughout the arterial tree. *Arteriosclerosis and thrombosis : a journal of vascular biology / American Heart Association*, 14(1):133--140, 1994.

R. M. Nerem, M. J. Levesque, and J. F. Cornhill. Vascular endothelial morphology as an indicator of the pattern of blood flow. *Journal of biomechanical engineering*, 103(3):172--176, 1981.

E. Nordmeier. Static and dynamic light-scattering solution behavior of pullulan and dextran in comparison. *J. Phys. Chem.*, 97(21):5770--5785, 1993.

G. Öjteg, K. Nygren, and M. Wolgast. Permeability of renal capillaries. i. preparation of neutral and charged protein probes. *Acta Physiologica Scandinavica*, 129(3):277--286, 1987.

N. Otsu. A threshold selection method from Gray-Level histograms. *Systems, Man and Cybernetics, IEEE Transactions on*, 9(1):62--66, 1979.

V. Peiffer, E. M. Rowland, S. G. Cremers, P. D. Weinberg, and S. J. Sherwin. Effect of aortic taper on patterns of blood flow and wall shear stress in rabbits: association with age. *Atherosclerosis*, 223(1):114--121, 2012.

V. Peiffer, A. A. Bharath, S. J. Sherwin, and P. D. Weinberg. A novel method for quantifying spatial correlations between patterns of atherosclerosis and hemodynamic factors. *Journal of biomechanical engineering*, 135(2), 2013a.

V. Peiffer, S. J. Sherwin, and P. D. Weinberg. Computation in the rabbit aorta of a new metric - the transverse wall shear stress - to quantify the multidirectional character of disturbed blood flow. *Journal of biomechanics*, 46(15):2651--2658, 2013b.

J. Petroff. Über die vitalfärbung der gefässwand. *Beitr Pathol Anat Allg Pathol*, 71:115--131, 1922.

D. Predescu and G. E. Palade. Plasmalemmal vesicles represent the large pore system of continuous microvascular endothelium. *The American journal of physiology*, 265(2 Pt 2), 1993.

A. Rachev and K. Hayashi. Theoretical study of the effects of vascular smooth muscle contraction on strain and stress distributions in arteries. *Annals of biomedical engineering*, 27(4):459--468, 1999.

B. Rippe, B.-I. I. Rosengren, O. Carlsson, and D. Venturoli. Transendothelial transport: the vesicle controversy. *Journal of vascular research*, 39(5):375--390, 2002.

E. M. Rowland, Y. Mohamied, K. Yean Chooi, E. L. Bailey, and P. D. Weinberg. Comparison of statistical methods for assessing spatial correlations between maps of different arterial properties. *Journal of biomechanical engineering*, 137(10), 2015.

D. Sage, D. Prodanov, J.-Y. Tinevez, and J. Schindelin. Daniel Sage: MIJ: Making interoperability between ImageJ and Matlab possible. In *ImageJ User & Developer Conference (IUDC'12)*, 2012.

J. Schindelin, I. Arganda-Carreras, E. Frise, V. Kaynig, M. Longair, T. Pietzsch, S. Preibisch, C. Rueden, S. Saalfeld, B. Schmid, J.-Y. Tinevez, D. J. White, V. Hartenstein, K. Eliceiri, P. Tomancak, and A. Cardona. Fiji: an open-source platform for biological-image analysis. *Nat Meth*, 9(7):676--682, 2012.

J. E. Schnitzer. gp60 is an albumin-binding glycoprotein expressed by continuous endothelium involved in albumin transcytosis. *The American journal of physiology*, 262(1 Pt 2), 1992.

A. Sebkhi and P. D. Weinberg. Age-related variations in transport properties of the rabbit arterial wall near branches. *Atherosclerosis*, 106(1):1--8, 1994a.

A. Sebkhi and P. D. Weinberg. Effect of dietary-cholesterol on the uptake of albumin by rabbit aortic-wall in-vivo. *JOURNAL OF PHYSIOLOGY-LONDON*, 479P:P77--P77, 1994b.

A. Sebkhi and P. D. Weinberg. Effect of age on the pattern of short-term albumin uptake by the rabbit aortic wall near intercostal branch ostia. *Arteriosclerosis, thrombosis, and vascular biology*, 16(2):317--327, 1996.

J. Seifter, D. Sloane, and A. Ratner. *Concepts in medical physiology*. Lippincott Williams & Wilkins, 2005.

Y. Shou, K.-m. Jan, and D. S. Rumschitzki. Transport in rat vessel walls. i. hydraulic conductivities of the aorta, pulmonary artery, and inferior vena cava with intact and denuded endothelia. *American Journal of Physiology - Heart and Circulatory Physiology*, 291(6):H2758--H2771, 2006.

Y. Shou, K.-m. Jan, and D. S. Rumschitzki. Transport in rat vessel walls. II. macromolecular leakage and focal spot size growth in rat arteries and veins. *American Journal of Physiology - Heart and Circulatory Physiology*, 292 (6):H2881--H2890, 2007.

B. R. Simon, M. V. Kaufmann, M. A. McAfee, A. L. Baldwin, and L. M. Wilson. Identification and determination of material properties for porohyperelastic analysis of large arteries. *Journal of biomechanical engineering*, 120(2):188--194, 1998.

H. Sinzinger, K. Silberbauer, and W. Auerswald. Quantitative investigation of sudanophilic lesions around the aortic ostia of human fetuses, newborn and children. *Blood vessels*, 17(1):44--52, 1980.

G. D. Sloop, R. S. Perret, J. S. Brahney, and M. Oalmann. A description of two morphologic patterns of aortic fatty streaks, and a hypothesis of their pathogenesis. *Atherosclerosis*, 141(1):153--160, 1998.

H. C. Stary, A. B. Chandler, R. E. Dinsmore, V. Fuster, S. Glagov, W. Insull, M. E. Rosenfeld, C. J. Schwartz, W. D. Wagner, and R. W. Wissler. A definition of advanced types of atherosclerotic lesions and a histological classification of atherosclerosis. *Circulation*, 92(5):1355--1374, 1995.

T. Staughton and P. D. Weinberg. Investigation of the role of endogenous nitric oxide synthesis in determining patterns of arterial wall permeability and diet-induced lipid deposition in the rabbit. In L. Clark, editor, *Trends in Atherosclerosis Research*, pages 123--144. Nova Biomedical Books, 2004.

D. Steinberg. Atherogenesis in perspective: Hypercholesterolemia and inflammation as partners in crime. *Nat Med*, 8(11):1211--1217, 2002.

M. B. Stemerman, E. M. Morrel, K. R. Burke, C. K. Colton, K. A. Smith, and R. S. Lees. Local variation in arterial wall permeability to low density lipoprotein in normal rabbit aorta. *Arteriosclerosis (Dallas, Tex.)*, 6 (1):64--69, 1986.

S. Tada and J. Tarbell. Fenestral pore size in the internal elastic lamina affects transmural flow distribution in the artery wall. *Annals of Biomedical Engineering*, 29(6):456--466, 2001.

J. M. Tarbell. Mass transport in arteries and the localization of atherosclerosis. *Annual Review of Biomedical Engineering*, 5(1):79--118, 2003.

J. M. Tarbell. Shear stress and the endothelial transport barrier. *Cardiovascular Research*, 87(2):320--330, 2010.

A. Tedgui and M. J. Lever. Filtration through damaged and undamaged rabbit thoracic aorta. *American Journal of Physiology - Heart and Circulatory Physiology*, 247(5):H784--H791, 1984.

A. Tedgui and M. J. Lever. The interaction of convection and diffusion in the transport of 131I-albumin within the media of the rabbit thoracic aorta. *Circulation research*, 57(6):856--863, 1985.

D. D. Thomas, X. Liu, S. P. Kantrow, and J. R. Lancaster. The biological lifetime of nitric oxide: implications for the perivascular dynamics of NO and o2. *Proceedings of the National Academy of Sciences of the United States of America*, 98(1):355--360, 2001.

G. Tortora and B. Derrickson. *Principles of Anatomy and Physiology*. Wiley International, 2006.

G. A. Truskey, W. L. Roberts, R. A. Herrmann, and R. A. Malinauskas. Measurement of endothelial permeability to 125I-low density lipoproteins in rabbit arteries by use of en face preparations. *Circulation Research*, 71(4):883--897, 1992.

P. L. Tuma and A. L. Hubbard. Transcytosis: Crossing cellular barriers. *Physiological Reviews*, 83(3):871--932, 2003.

D. W. Urry and T. M. Parker. Mechanics of elastin: molecular mechanism of biological elasticity and its relationship to contraction. *Journal of muscle research and cell motility*, 23(5-6):543--559, 2002.

D. W. Urry, B. Haynes, D. Thomas, and R. D. Harris. A method for fixation of elastin demonstrated by stress/strain characterization. *Biochemical and biophysical research communications*, 151(2):686--692, 1988.

S. van der Walt, J. L. Schönberger, J. Nunez-Iglesias, F. Boulogne, J. Warner, N. Yager, E. Gouillart, T. Yu, and the scikit-image contributors. scikit-image: image processing in Python. *PeerJ*, 2:e453, 2014.

D. M. Wang and J. M. Tarbell. Modeling interstitial flow in an artery wall allows estimation of wall shear stress on smooth muscle cells. *Journal of biomechanical engineering*, 117(3):358--363, 1995.

S. Weinbaum, G. Tzeghai, P. Ganatos, R. Pfeffer, and S. Chien. Effect of cell turnover and leaky junctions on arterial macromolecular transport. *The American journal of physiology*, 248(6 Pt 2), 1985.

P. D. Weinberg. Disease patterns at arterial branches and their relation to flow. *Biorheology*, 39(3-4):533--537, 2002.

P. D. Weinberg. Rate-limiting steps in the development of atherosclerosis: the response-to-influx theory. *Journal of vascular research*, 41(1):1--17, 2004.

P. D. Weinberg, S. L. Carney, C. P. Winlove, and K. H. Parker. The contributions of glycosaminoglycans, collagen and other interstitial components to the hydraulic resistivity of porcine aortic wall. *Connect Tissue Res*, 36(4):297--308, 1997.

J. A. Weiss and B. J. Maakestad. Permeability of human medial collateral ligament in compression transverse to the collagen fiber direction. *Journal of biomechanics*, 39(2):276--283, 2006.

WHO. Cardiovascular diseases fact sheet, 2009.

C. P. Winlove, J. Davis, A. Baldwin, and A. Chabanel. Effects of particle size and perfusate composition on the uptake of colloidal gold by the rabbit thoracic aorta perfused in situ. *Atherosclerosis*, 44(1):99--111, 1982.

G. J. Ye, A. P. Nesmith, and K. K. K. Parker. The role of mechanotransduction on vascular smooth muscle myocytes' [corrected] cytoskeleton and contractile function. *Anatomical record (Hoboken, N.J. : 2007)*, 297 (9):1758--1769, 2014.

M. A. Zulliger, N. T. Kwak, T. Tsapikouni, and N. Stergiopulos. Effects of longitudinal stretch on vsm tone and distensibility of muscular conduit arteries. *American Journal of Physiology-Heart and Circulatory Physiology*, 283(6):H2599--H2605, 2002.

Appendix A

Publications

Parts of the work presented in this thesis have been presented previously in publications or presentations detailed below.

A.1 Journal Articles

A combined numerical and experimental framework for determining permeability properties of the arterial media Comerford, A., Chooi, K. Y., Nowak, M., Weinberg, P. D. and Sherwin, S. J.
Biomechanics and modeling in mechanobiology 14/2:297-313 (2015)

Comparison of Statistical Methods for Assessing Spatial Correlations Between Maps of Different Arterial Properties Rowland, E M., Mohamied, Y., Chooi, K.Y., Bailey, E. L. and Weinberg, P. D.
Journal of biomechanical engineering 137/10 (2015)

Intimal and medial contributions to the hydraulic resistance of the arterial wall at different pressures: a combined computational and experimental study Chooi, K. Y., Comerford, A., Sherwin, S. J. and Weinberg, P. D.
Journal of the Royal Society Interface (submitted 2015)

Role of endothelial permeability hotspots and endothelial mitosis in determining age-related patterns of macromolecule uptake by the rabbit aortic wall near branch points Chooi, K. Y., Comerford, A., Cremers, S.G. and Weinberg, P. D.
American journal of physiology. Heart and circulatory physiology (submitted 2015)

A.2 Conference Contributions

Smooth muscle tone-dependent hydraulic conductance of aortic media Chooi, K.Y., Comerford, A., Sherwin, S. J. and Weinberg, P. D.
Oral presentation. MEIbioeng15, 2015, Leeds

3D confocal imaging of the arterial wall to determine structure and hydraulic permeability Chooi, K.Y., Comerford, A., Weinberg, P. D.
Poster presentation. British Atherosclerosis Society Meeting, 2015, Manchester

Pressure-dependent Permeability of Aortic Elastic Lamellae to Albumin Chooi, K.Y., Comerford, A., Weinberg, P. D.
Poster presentation. World Congress of Biomechanics, 2014, Boston

Pressure-dependent Permeability of Aortic Elastic Lamellae to Albumin Chooi, K.Y., Comerford, A., Weinberg, P. D.

Poster presentation. The 9th International Symposium on Biomechanics in Vascular Biology and Cardiovascular Disease, 2014, Montreal

3D confocal imaging of the arterial wall to determine structure and permeability Chooi, K.Y.
Oral presentation. Imperial College 3D imaging symposium, 2014

Spatial correspondence of endothelial 'hotspots' with mitosis rate and lesion prevalence around intercostal branch ostia in immature and mature rabbit aortas Chooi, K. Y., Comerford, A., Cremers, S.G. and Weinberg, P. D.
Poster presentation. British Atherosclerosis Society Autumn Meeting, 2013, Cambridge

Spatial correspondence of endothelial 'hotspots' with mitosis rate and lesion prevalence around intercostal branch ostia in immature and mature rabbit aortas Chooi, K. Y., Comerford, A., Cremers, S.G. and Weinberg, P. D.
Poster presentation. Bioengineering 13, 2013, Glasgow

Development and characterisation of the isolated rat aortic bifurcation as a system to study arterial transmural transport Chooi, K.Y., Comerford, A., Weinberg, P. D.
Poster presentation. The 8th International Symposium on Biomechanics in Vascular Biology and Cardiovascular Disease, 2013, Rotterdam

Appendix B

Attenuation Correction and Image Volume Rotation

Three separate scripts were written to make this process efficient. The first downsamples all the image volumes so the second script runs more quickly (Section B.1). The second script prompts the user for input parameters for the third script: The user is shown the downsampled images and rotation angles and crop dimensions are set based on these (Section B.2). The third reads in all the user-defined parameters and performs all the rotations and intensity attenuation correction on the full resolution image volumes (Section B.3).

B.1 Downsampling

```
/*script to reduce resolution by 8x8 binning of .tiff files in
preparation for xy and xz rotation. Also sets up file
structure for the xy and xz rotations */

 run("Close All");
 print("\\Clear");

// paths and files
// dir=location of *.tiff files, produced by lif_to_tiff.txt
dir="/Volumes/KYC_2TBport/rotate_20150128/";
file_list = getFileList(dir);
//Array.show(file_list);
n_files=file_list.length;

print("Number of files="+n_files);
for (i=0; i<file_list.length; i++) {
print("file number "+toString(i)+": "+file_list[i]);
}

j=0;
image_list=newArray(n_files);
for (i=0; i<file_list.length; i++) {
if(endsWith(file_list[i],".tiff")){
image_list[j]=file_list[i];
j=j+1;
}
}
image_list=Array.trim(image_list,j);
n_images=image_list.length;
```

```
print("Number of .tiff images="+image_list.length);
for (i=0; i<image_list.length; i++) {
print("image number "+toString(i)+": "+image_list[i]);
}

//Save image_list as a .txt file for future use
file_handle=File.open(dir+"image_list.txt");

for (i=0; i<image_list.length; i++) {
print(file_handle,image_list[i]);
}

File.close(file_handle);

//Array.show(image_list);
Array.sort(image_list);
Array.show(image_list);

start=0;
end=5;

print("1st image:"+image_list[start]);
print("last image:"+image_list[end]);
print("list of images to be processed:\n");
for (i=start; i<(end+1); i++) {
print(image_list[i]);
}



//for(i=6; i<image_list.length; i++) {
for(i=start; i<(end+1); i++) {
print("Progress: "+i+" of "+n_images+" completed");

tiff_file=image_list[i];
sub_dir=replace(tiff_file, '.tiff', '/'); //folder to store virtual stack processes...
xy_rot_dir="xy_rotate/"; //folder for rotations in xy plane
xz_rot_dir="xz_rotate/"; //folder for rotations in xy plane

xy_rotate_dir=dir+sub_dir+xy_rot_dir;
xz_rotate_dir=dir+sub_dir+xz_rot_dir;

print("directory: "+dir);
print("orginal tiff file: "+tiff_file);
print("sub directory for virtual stack process ...
intermediate outputs of xy rotation: "+xy_rotate_dir);
print("sub directory for virtual stack process ...
intermediate outputs of xz rotation: "+xz_rotate_dir);

// Make directories
```

```
File.makeDirectory(dir+sub_dir);
File.makeDirectory(xy_rotate_dir);
File.makeDirectory(xz_rotate_dir);

//load image for resolution reduction
orig_tiff=dir+tiff_file;
print("loading original from: "+orig_tiff);
run("TIFF Virtual Stack...", "open=[orig_tiff]");
run("Collect Garbage");

//set voxel size in real units before doing any manipulation
print("set voxel size in real units");
selectWindow(tiff_file);
run("Properties...", "unit=nm pixel_width=130.55 pixel_height=130.55 voxel_depth=167.85");

//reduce resolution
print("reduce resolution");
selectWindow(tiff_file);
run("Bin...", "x=8 y=8 z=8 bin=Average");
run("Collect Garbage");

//enhance contrast
print("enhance contrast");
run("Enhance Contrast...", "saturated=0.4 normalize process_all");
run("Collect Garbage");

//save as tiff
print("saving as"+dir+sub_dir+"binned_888_contrast_enhanced.tif");
saveAs("Tiff", dir+sub_dir+"binned_888_contrast_enhanced.tif");
selectWindow("binned_888_contrast_enhanced.tif");
close();
run("Collect Garbage");


}

exit("Clean exit")
```

B.2 User prompting

```
run("Close All");
print("\\Clear");

// paths and files
dir="/Volumes/KYC_2TBport/rotate_20150128/";
image_list_str=File.openAsString(dir+"image_list.txt");
image_list=split(image_list_str,"\n");
//Array.show(image_list);
```

```
n_images=image_list.length

//get a list of only the Rhodamine (ch=1) images: image_list_reduced
if (n_images==1){
image_list_reduced=image_list;
print("only one image found: Is this a test-run? 2 channels expected");
}
else{
image_list_reduced=newArray(n_images/2);
for (i=0; i<n_images/2; i++) {
image_list_reduced[i]=image_list[i*2+1];
}
}


Array.show(image_list_reduced);
Array.sort(image_list_reduced);
Array.show(image_list_reduced);

start=0;
end=2;

print("1st image:"+image_list_reduced[start]);
print("last image:"+image_list_reduced[end]);
print("list of images to be processed:\n");
for (i=start; i<(end+1); i++) {
print(image_list_reduced[i]);
}

for (i=start; i<(end+1); i++) { //short loop for testing purposes
// for (i=9; i<n_images/2; i++) {
  print("Progress: "+i+" of "+n_images/2+" completed");
tiff_file=image_list_reduced[i];
sub_dir=replace(tiff_file, '.tiff', '/'); //folder to store virtual stack processes...
xy_rot_dir="xy_rotate/"; //folder for rotations in xy plane
xz_rot_dir="xz_rotate/"; //folder for rotations in xy plane

xy_rotate_dir=dir+sub_dir+xy_rot_dir;
xz_rotate_dir=dir+sub_dir+xz_rot_dir;

print("directory: "+dir);
print("orginal tiff file: "+tiff_file);
print("sub directory for virtual stack process intermediate outputs of xy rotation:...
 "+xy_rotate_dir);
print("sub directory for virtual stack process intermediate outputs of xz rotation: ...
"+xz_rotate_dir);

// Make directories
File.makeDirectory(dir+sub_dir);
File.makeDirectory(xy_rotate_dir);
```

```
File.makeDirectory(xz_rotate_dir);


//Create .txt file to hold all the cropping and rotating parameters
output_file=dir+sub_dir+"xy_xz_rotate_params.txt";
f_handle=File.open(output_file);


// inputs
crop1=newArray(0,0,0,0); // crop coords before any rotations
crop2=newArray(0,0,0,0); // crop coords before after xy rotation
crop3=newArray(0,0,0,0); // crop coords before after xy rotation

alpha_xy=0; //rotation angle in xy plane
alpha_xz=0; //rotation angle in xz plane


//load image for rotations
binned_tiff=dir+sub_dir+"binned_888_contrast_enhanced.tif";
print("loading binned image from: "+binned_tiff);
open(binned_tiff);
run("Collect Garbage");

//remove slices from below the sample
selectWindow("binned_888_contrast_enhanced.tif");
waitForUser("Slice selection","note down start and end of useful stack to enter as z_start and..
 z_end as inputs to xy_xz_rotate.ijm");
z_start_1=getNumber("Enter z_start:",1); // z slices to keep before any rotations
z_end_1=getNumber("Enter z_end:",nSlices);
run("Slice Keeper", "first=z_start_1 last=z_end_1 increment=1");
File.append("z_start_1:\n"+z_start_1*8-7,output_file);
File.append("z_end_1:\n"+z_end_1*8,output_file);
run("Collect Garbage");

//close inactive windows to save memory
selectWindow("binned_888_contrast_enhanced.tif");
close();
run("Collect Garbage");

//set voxel size in real units before doing any manipulation
print("set voxel size in real units");
selectWindow("binned_888_contrast_enhanced.tif kept stack");
run("Properties...", "unit=nm pixel_width=1044.4 pixel_height=1044.4 voxel_depth=1342.8");

//Get coords for first crop
setTool("rectangle");
waitForUser("Crop1 ROI","Draw a rectangular ROI to input coordinates for crop1 as inputs ...
to xy_xz_rotate.ijm");
Roi.getBounds(crop1[0], crop1[1], crop1[2], crop1[3]);
//Array.show(crop1);
```

```
//crop1=Array.print(crop1);
File.append("crop1[0]:\n"+crop1[0]*8-7,output_file);
File.append("crop1[1]:\n"+crop1[1]*8-7,output_file);
File.append("crop1[2]:\n"+crop1[2]*8,output_file);
File.append("crop1[3]:\n"+crop1[3]*8,output_file);
run("Collect Garbage");

//crop in xy plane to save memory
print("crop coordinates (crop1):");
Array.print(crop1);
selectWindow("binned_888_contrast_enhanced.tif kept stack");
makeRectangle(crop1[0], crop1[1], crop1[2], crop1[3]);
run("Crop");
run("Collect Garbage");

//get alpha_xy and rotate the stack
selectWindow("binned_888_contrast_enhanced.tif kept stack");
setTool("line");
waitForUser("alpha_xy","Draw parallel to IEL from top to bottom to calculate alpha_xy as ...
input to xy_xz_rotate.ijm");
Roi.getCoordinates(xpoints, ypoints);
//Array.show(xpoints);
//Array.show(ypoints);
alpha_xy=90-atan2((ypoints[1]-ypoints[0]),(xpoints[1]-xpoints[0]))*180/PI;
//waitForUser("alpha_xy","Work out rotation required in xy plane as input (alpha_xy) to...
 xy_xz_rotate.ijm");
//alpha_xy=getNumber("Enter alpha_xy:",0); // z slices to keep before any rotations
File.append("alpha_xy:\n"+alpha_xy,output_file);
print("perform rotation in xy plane");

selectWindow("binned_888_contrast_enhanced.tif kept stack");
   setBatchMode(true);
   id = getImageID;
   for (j=1; j<= nSlices; j++) {
       showProgress(j, nSlices);
       selectImage(id);
       setSlice(j);
       name = getMetadata;
       run("Duplicate...", "title=temp");
      run("Rotate... ", "angle=alpha_xy grid=1 interpolation=Bilinear enlarge");
       saveAs("tif", xy_rotate_dir+pad(j-1));
       close();
   }
   setBatchMode(false);
   run("Image Sequence...", "open=["+xy_rotate_dir+"00000.tif] use");
   run("Collect Garbage");

selectWindow("binned_888_contrast_enhanced.tif kept stack");
close();
run("Collect Garbage");
```

```
/*selectWindow("binned_888_contrast_enhanced.tif kept stack");
run("Rotate... ", "angle=alpha_xy grid=1 interpolation=Bilinear enlarge stack");
run("Collect Garbage");*/

//Get coords for second crop
setTool("rectangle");
waitForUser("Crop2 ROI","Draw a rectangular ROI to input coordinates for crop2 as inputs ...
to xy_xz_rotate.ijm");
Roi.getBounds(crop2[0], crop2[1], crop2[2], crop2[3]);
//Array.show(crop2);
//crop1=Array.print(crop2);
File.append("crop2[0]:\n"+crop2[0]*8-7,output_file);
File.append("crop2[1]:\n"+crop2[1]*8-7,output_file);
File.append("crop2[2]:\n"+crop2[2]*8,output_file);
File.append("crop2[3]:\n"+crop2[3]*8,output_file);
run("Collect Garbage");

//crop in xy plane to save memory
print("crop coordinates (crop2):");
Array.print(crop2);
selectWindow("xy_rotate");
makeRectangle(crop2[0], crop2[1], crop2[2], crop2[3]);
run("Crop");
run("Collect Garbage");

//Reslice
print("Reslice...");
selectWindow("xy_rotate");
run("Reslice [/]...", "output=1 start=Top avoid");
run("Collect Garbage");

//close inactive windows to save memory
selectWindow("xy_rotate");
close();
run("Collect Garbage");


//get alpha_xz and rotate the stack
selectWindow("Reslice of xy_rotate");
setTool("line");
waitForUser("alpha_xz","Draw parallel to IEL from top to bottom to calculate alpha_xz as...
 input to xy_xz_rotate.ijm");
Roi.getCoordinates(xpoints, ypoints);
//Array.show(xpoints);
//Array.show(ypoints);
alpha_xz=90-atan2((ypoints[1]-ypoints[0]),(xpoints[1]-xpoints[0]))*180/PI;
//waitForUser("alpha_xy","Work out rotation required in xy plane as input (alpha_xy) ...
to xy_xz_rotate.ijm");
```

```
//alpha_xy=getNumber("Enter alpha_xy:",0); // z slices to keep before any rotations
File.append("alpha_xz:\n"+alpha_xz,output_file);


print("perform rotation in xz plane");

selectWindow("Reslice of xy_rotate");
   setBatchMode(true);
   id = getImageID;
   for (j=1; j<= nSlices; j++) {
       showProgress(j, nSlices);
       selectImage(id);
       setSlice(j);
       name = getMetadata;
       run("Duplicate...", "title=temp");
      run("Rotate... ", "angle=alpha_xz grid=1 interpolation=Bilinear enlarge");
       saveAs("tif", xz_rotate_dir+pad(j-1));
       close();
   }
   setBatchMode(false);
   run("Image Sequence...", "open=["+xz_rotate_dir+"00000.tif] use");
   run("Collect Garbage");

   selectWindow("Reslice of xy_rotate");
close();
run("Collect Garbage");

/*selectWindow("Reslice of binned_888_contrast_enhanced");
run("Rotate... ", "angle=alpha_xz grid=1 interpolation=Bilinear enlarge stack");
run("Collect Garbage");*/

//Get coords for second crop
setTool("rectangle");
waitForUser("Crop3 ROI","Draw a rectangular ROI to input coordinates for crop3 as ...
inputs to xy_xz_rotate.ijm");
Roi.getBounds(crop3[0], crop3[1], crop3[2], crop3[3]);
//Array.show(crop2);
//crop1=Array.print(crop2);
File.append("crop3[0]:\n"+crop3[0]*8-7,output_file);
File.append("crop3[1]:\n"+crop3[1]*8-7,output_file);
File.append("crop3[2]:\n"+crop3[2]*8,output_file);
File.append("crop3[3]:\n"+crop3[3]*8,output_file);
run("Collect Garbage");

//crop in xz plane to save memory
print("crop coordinates (crop3):");
Array.print(crop3);
selectWindow("xz_rotate");
makeRectangle(crop3[0], crop3[1], crop3[2], crop3[3]);
run("Crop");
```

```
run("Collect Garbage");

//save result
print("Saving final tiff stack as "+dir+sub_dir...
+"binned_888_contrast_enhanced_xy_xz_rotate.tif");
selectWindow("xz_rotate");
saveAs("Tiff", dir+sub_dir+"binned_888_contrast_enhanced_xy_xz_rotate.tif");
run("Collect Garbage");
close();

File.close(f_handle);


}
exit("Clean exit")

 function pad(n) {
      str = toString(n);
      while (lengthOf(str)<5)
          str = "0" + str;
      return str;
  }
```

B.3 Rotation and attenuation correction

```
run("Close All");
 print("\\Clear");
 run("Collect Garbage");

// paths and files
//dir="/Users/kyc106/Desktop/80mmHg scans/";
dir="/Volumes/KYC_2TBport/rotate_20150128/";


image_list_str=File.openAsString(dir+"image_list.txt");
image_list=split(image_list_str,"\n");
//Array.show(image_list);
n_images=image_list.length
print("number of images="+n_images);

//Array.show(image_list);
Array.sort(image_list);
Array.show(image_list);

start=0;
end=5;

print("1st image:"+image_list[start]);
print("last image:"+image_list[end]);
```

```
print("list of images to be processed:\n");
for (i=start; i<(end+1); i++) {
print(image_list[i]);
}

for (i=start; i<(end+1); i++) { // short loop for testing
//for(i=6; i<n_images; i++) {

print("Progress: "+i+" of "+n_images+" completed");

tiff_file=image_list[i];
sub_dir=replace(tiff_file, '.tiff', '/');
if(endsWith(sub_dir,"c=0/")){
sub_dir1=replace(sub_dir,'c=0/', 'c=1/');
}
else{
sub_dir1=sub_dir;
}
//folder to store virtual stack processes...
xy_rot_dir="xy_rotate_large/"; //folder for rotations in xy plane
xz_rot_dir="xz_rotate_large/"; //folder for rotations in xy plane

xy_rotate_dir=dir+sub_dir+xy_rot_dir;
xz_rotate_dir=dir+sub_dir+xz_rot_dir;

print("directory: "+dir);
print("orginal tiff file: "+tiff_file);
print("sub directory for rotation params: "+dir+sub_dir1);
print("sub directory for virtual stack process intermediate outputs of xy rotation:...
 "+xy_rotate_dir);
print("sub directory for virtual stack process intermediate outputs of xz rotation:...
 "+xz_rotate_dir);

// Make directories
File.makeDirectory(dir+sub_dir);
File.makeDirectory(xy_rotate_dir);
File.makeDirectory(xz_rotate_dir);

// inputs

input_params_str=File.openAsString(dir+sub_dir1+"xy_xz_rotate_params.txt");
//input_params_str=File.openAsString("/Volumes/Yean_Chooi/Confocal_scans/Pressurised ...
AB/80mmHg/pres_aorta_80mmHg_20140328_position2_c=1/xy_xz_rotate_params.txt")
input_params=split(input_params_str,"\n");
//Array.show(input_params);
n_params=input_params.length/2;
print("number of parameters="+n_params);
param_names=newArray(n_params);
params=newArray(n_params);
for (j=0; j<n_params; j++) {
```

```
param_names[j]=input_params[j*2];
params[j]=input_params[j*2+1];
}
//Array.show(params);
//Array.show(param_names);

//load image for rotations
orig_tiff=dir+tiff_file;
print("loading original from: "+orig_tiff);
run("TIFF Virtual Stack...", "open=[orig_tiff]");
run("Collect Garbage");
Stack.getDimensions(width, height, channels, slices, frames);

z_start_1=params[0];
z_end_1=params[1];

if (z_start_1<1){
z_start_1=1;
}

if (z_end_1>nSlices){
z_end_1=nSlices;
}

alpha_xy=params[6];
alpha_xz=params[11];

crop1=Array.slice(params,2,6);
crop2=Array.slice(params,7,11);
crop3=Array.slice(params,12,16);

print("z_start_1="+z_start_1);
print("z_end_1="+z_end_1);

print("alpha_xy="+alpha_xy);
print("alpha_xz="+alpha_xz);

print("crop coordinates (crop1):");
Array.print(crop1);

print("crop coordinates (crop2):");
Array.print(crop2);

print("crop coordinates (crop3):");
Array.print(crop3);

//remove slices from below the sample
selectWindow(tiff_file);
print("Running Slice Keeper");
run("Slice Keeper", "first=z_start_1 last=z_end_1 increment=1");
```

```
run("Collect Garbage");

//close inactive windows to save memory
selectWindow(tiff_file);
close();
run("Collect Garbage");

//set voxel size in real units before doing any manipulation
print("set voxel size in real units");
selectWindow(tiff_file+" kept stack");
run("Properties...", "unit=nm pixel_width=130.55 pixel_height=130.55 voxel_depth=167.85");

//crop in xy plane to save memory
selectWindow(tiff_file+" kept stack");
Stack.getDimensions(width, height, channels, slices, frames);
print("width="+width+"\n"+"height="+height);
print("crop coordinates (crop1 original):");
Array.print(crop1);

if (crop1[0]<0){
crop1[0]=0;
}

if (crop1[1]<0){
crop1[1]=0;
}

print("crop coordinates (crop1):");
Array.print(crop1);

makeRectangle(crop1[0], crop1[1], crop1[2], crop1[3]);
run("Crop");
print("Cropping...");
run("Collect Garbage");

//account for z-drop-of before any rotations take place
print("enhance local contrast: saturation = 0.4%, images normalised");
selectWindow(tiff_file+" kept stack");
run("Enhance Contrast...", "saturated=0.4 normalise process_all");
run("Collect Garbage");

//rotate in xy plane to align elastin sheets to vertical edge of image
print("performing rotation in xy plane...");
selectWindow(tiff_file+" kept stack");
   setBatchMode(true);
   id = getImageID;
   for (j=1; j<= nSlices; j++) {
       showProgress(j, nSlices);
       selectImage(id);
       setSlice(j);
```

```
        name = getMetadata;
        run("Duplicate...", "title=temp");
       run("Rotate... ", "angle=alpha_xy grid=1 interpolation=Bilinear enlarge");
        saveAs("tif", xy_rotate_dir+pad(j-1));
        close();
    }
    setBatchMode(false);
    run("Image Sequence...", "open=["+xy_rotate_dir+"00000.tif] use");

//close inactive windows to save memory
selectWindow(tiff_file+" kept stack");
close();
run("Collect Garbage");

//crop in xy plane to save memory
selectWindow("xy_rotate_large");
Stack.getDimensions(width, height, channels, slices, frames);
print("width="+width+"\n"+"height="+height);
print("crop coordinates (crop2 original):");
Array.print(crop2);

if (crop2[0]<0){
crop2[0]=0;
}

if (crop2[1]<0){
crop2[1]=0;
}

makeRectangle(crop2[0], crop2[1], crop2[2], crop2[3]);
print("crop coordinates (crop2):");
Array.print(crop2);
run("Crop");
print("Cropping...");
run("Collect Garbage");

//Reslice
print("Reslice...");
selectWindow("xy_rotate_large");
run("Reslice [/]...", "output=1 start=Top avoid");
run("Collect Garbage");

//close inactive windows to save memory
selectWindow("xy_rotate_large");
close();
run("Collect Garbage");

//rotate in xz plane to align elastin sheets to vertical edge of image
print("performing rotation in xz plane...");
selectWindow("Reslice of xy_rotate_large");
```

```
   setBatchMode(true);
   id = getImageID;
   for (j=1; j<= nSlices; j++) {
       showProgress(j, nSlices);
       selectImage(id);
       setSlice(j);
       name = getMetadata;
       run("Duplicate...", "title=temp");
      run("Rotate... ", "angle=alpha_xz grid=1 interpolation=Bilinear enlarge");
       saveAs("tif", xz_rotate_dir+pad(j-1));
       close();
   }
   setBatchMode(false);
   run("Image Sequence...", "open=["+xz_rotate_dir+"00000.tif] use");

//close inactive windows to save memory
selectWindow("Reslice of xy_rotate_large");
close();
run("Collect Garbage");

//crop in xz plane to save memory
selectWindow("xz_rotate_large");
Stack.getDimensions(width, height, channels, slices, frames);
print("width="+width+"\n"+"height="+height);
print("crop coordinates (crop3 original):");
Array.print(crop3);

if (crop3[0]<0){
crop3[0]=0;
}

if (crop3[1]<0){
crop3[1]=0;
}

makeRectangle(crop3[0], crop3[1], crop3[2], crop3[3]);

print("crop coordinates (crop3):");
Array.print(crop3);
run("Crop");
print("Cropping...");
run("Collect Garbage");

//Reslice
print("Reslice...");
selectWindow("xz_rotate_large");
run("Reslice [/]...", "output=1 start=Top avoid");
run("Collect Garbage");

//save result
```

```
print("Saving final tiff stack as "+dir+sub_dir+"xy_xz_rotate.tif");
selectWindow("Reslice of xz_rotate_large");
saveAs("Tiff", dir+sub_dir+"xy_xz_rotate.tif");
run("Close All");
run("Collect Garbage");


}

exit("Clean exit")



    function pad(n) {
      str = toString(n);
      while (lengthOf(str)<5)
          str = "0" + str;
      return str;
  }
```